DYNAMICS OF COPPER OXIDATION INVESTIGATED BY *IN SITU* UHV-TEM

by

Guangwen Zhou

BS, Xiangtan University, 1993

MS, Beijing Polytechnic University, 1996

Submitted to the Graduate Faculty of

the School of Engineering in partial fulfillment

of the requirements for the degree of

Doctor of Philosophy

University of Pittsburgh

2003

UNIVERSITY OF PITTSBURGH

SCHOOL OF ENGINEERING

This dissertation was presented

by

Guangwen Zhou

It was defended on

November 24, 2003

and approved by

Dr. John A. Barnard, Professor, Department of Materials Science and Engineering

Dr. Gerald H. Meier, Professor, Department of Materials Science and Engineering

Dr. Scott X. Mao, Professor, Department of Mechanical Engineering

Dr. Mridula D. Bharadwaj, Senior Research Engineer, U.S. Steel Corporation

Dissertation Director: Dr. Judith C. Yang, Assistant Professor,
Department of Materials Science and Engineering

DYNAMICS OF COPPER OXIDATION INVESTIGATED BY *IN SITU* UHV-TEM

Guangwen Zhou, Ph.D.

University of Pittsburgh, 2003

To bridge the gap between information provided by surface science methods (adsorption of up to ~a few monolayers of oxygen) and that provided by bulk oxidation studies (typically, an oxide layer of a few microns or thicker), the initial stages of metal oxidation — from nucleation to coalescence — are being investigated by *in situ* ultra-high vacuum transmission electron microscopy (UHV-TEM).

The aims of this thesis research are to gain basic insight into the complex kinetics and energetics of nano-oxide formation during the initial stages of oxidation, and fundamentally understand the distribution, stability, and morphological evolution of oxide islands since controlled oxidation is a processing tool for creating nanostructure patterns on surfaces. A systematic *in situ* study was carried out of the dynamic responses of Cu thin films to variations in thermodynamic variables such as temperature, oxygen pressure, strain, and crystallographic orientation. The main findings of the experiments include: 1) the universality of oxygen surface diffusion model, 2) formation of completely different oxide structure from oxide islands (disks, nanorods, dome, container pyramids) to disordered networks and almost uniform layer growth by altering the oxidation temperature and substrate orientation, 3) creation of nano-indentation arrays on metal surfaces by reducing the oxide arrays. The *in situ* UHV-TEM measurements of shape and size evolution of the oxides were used to gain fundamental insights into the complex kinetics and energetics of oxidation and reduction. Models based on the surfaces and strain during oxidation explained quantitatively the formation of some of the novel oxide nano-structures. A wealth of surface processes was discovered that reveal how each surface and thermodynamic condition needs to be considered for fundamentally understanding and controlling oxidation behavior.

TABLE OF CONTENTS

LIST OF TABLES

LIST OF FIGURES

ACKNOWLEDGEMENTS

My first, and most earnest, acknowledgment must go to my advisor, Prof. Judith C. Yang. Nearly four years ago, a telephone conversation with Prof. Yang started me on the path I traveled at Pitt. She has been instrumental in ensuring my academic, professional and financial wellbeing ever since. In every sense, none of this work would have been possible without her.

My special thanks go to the Frederick Seitz Materials Research Laboratory, the University of Illinois at Urbana-Champaign, where the experimental work in this thesis was carried out. I would like to thank R. Twesten, M. Marshall, K. Colravy, and N. Finnegan for their generous technical assistance.

The time spent by the committee members and their suggestions to improve the thesis are all very much appreciated.

I would like to thank Prof. Will Slaughter, Prof. Jorg Wiezorek, and Prof. Ian Nettleship for the discussion regarding the formation of the container oxide structure.

I am grateful to Mridula Bharadwaj for her help in many ways during the beginning time of my graduate study at Pitt.

I would like to thank Dr. Jeffrey Eastman for the discussion regarding the impact of the nano-oxidation on the nano-technology.

I would thank Dr. K.M. Goldman for reading my thesis.

I am grateful to my colleages and friends, Long Li, Fengting Xu, Deyu Li, Maja Kisa, Liang Wang, Richard McAfee, Xuetian Han, for their assistance on countless occasions.

My final, and most heartfelt, acknowledgment must go to my wife, Weiying. Weiying has worked diligently, and successfully, to show me life outside Benedum Hall. Her support, encouragement, and companionship have turned my journey through graduate school into a pleasure. For all that, and for being everything I am not, she has my everlasting love.

1.0 GENERAL INTRODUCTION

From the standpoint of thermodynamics, all metals except Au exhibit a tendency to oxidize in the earth's atmosphere. The driving force for oxidation of a given metal depends on the free-energy change, but the rate of oxidation and the morphological changes of the oxide during oxidation depend on complex kinetics and energetics of the particular materials system. The goal of this thesis research is to investigate and fundamentally understand the kinetics and energetics of oxide formation in the initial stages of oxidation and the distribution, stability, and morphological evolution of oxide islands in response to variations in thermodynamic variables such as temperature, pressure, strain, and crystallographic orientation.

Since the expression, "the initial stages of oxidation", may mean different things to different people, it is necessary to indicate more specifically just what this study involves. The initial stages of oxidation processes can be classified in four categories, the boundaries between these categories are somewhat uncertain. The categories are: 1) surface adsorption, 2) oxide nucleation, 3) oxide growth, and 4) coalescence of film growth. This thesis will present information mainly on the structure and topography of the oxide as related to the nucleation and growth and no specific information on adsorption, which is the first stage of the oxidation process, will be given.

Oxygen reactions with metal surfaces have been studied extensively to understand oxidation kinetics. In Chapter 2, the background of this research project is introduced. The systems primarily investigated were Cu thin films with different orientations. The initial state of a metal surface, such as surface impurities and surface morphology, may greatly influence the oxide nucleation, growth and hence the oxide film structure. Experiments, therefore, have to be performed under ultra high vacuum (UHV) conditions, which is critical for quantitative understanding of nucleation and growth kinetics. Secondly, the experimental conditions should be kept as simple as possible to allow for a reasonable interpretation of the results. Therefore, this work is concerned with the interaction of gas with single crystalline substrates. Visualizing

the oxidation process at the nanometer scale with *in situ* experiments under UHV conditions will provide a detailed understanding of the fundamental processes which take place during oxidation and further give essential insights into the complex kinetics and energetics of nano-oxide formation. Therefore, a modified *in situ* UHV transmission electron microscope (TEM) was employed to observe the oxidation processes in real time. It provides a unique view of dynamic reactions as they occur. The detailed experimental procedure is given in Chapter 3.

The initial stages of oxidation on Cu(100), Cu(110) and Cu(111) surfaces were systematically investigated in this work. Many factors affecting the kinetics/energetics of the nucleation and growth of the oxide exist in the determination of the morphology, size and structures of nanoscale oxide islands. We are investigating the dependency of the oxide island density, size distribution, morphology, etc., on the oxidation parameters, such as oxygen pressure, substrate temperature and surface orientations of the substrate. These topics can be found in Chapter 4, 5, 6. In Chapter 7, the stability of the oxide islands on Cu(100) surfaces was investigated under different oxygen pressure and temperature conditions.

Clearly, the oxygen-metal surface reaction covers a wide range of topics from surface adsorption to bulk oxide growth. With the development of well-controlled experiments and the increased experimental capabilities in resolution and cleanliness, many new phenomena could be revealed and need intensive theoretical modeling. The dynamic observation of Cu oxidation in the initial stages in this work has revealed a wealth of surface processes as concluded in chapter 8 followed by the possible future work in Chapter 9.

2.0 BACKGROUND

2.1 INTRODUCTION

The interaction of oxygen with surfaces ranges from single oxygen atom surface adsorption to bulk oxide growth. The improved experimental techniques in UHV now make it feasible to investigate surfaces that are atomically clean. Many elegant experiments have been performed using UHV scanning-tunneling-microscopy (STM) to watch the interaction of gases, including oxygen, on bare metal surfaces. One example is shown in Figure 2.1 (a) which shows the chemisorption of oxygen atoms on a Ni surface [1]. Usually, this process is accompanied by the breaking of several nearest-neighbor bonds within the substrate lattices, and it has become clear over the last twenty years that oxygen chemisorption often induces a large reconstruction of the metal surfaces. The chemisorption of oxygen on Cu surfaces is a prototype of this category of the reconstruction and has been studied extensively. The generally accepted conclusion is that the oxygen forms chains of Cu-O, referred to as the "missing-row" surface reconstruction [2-6]. *In situ* UHV-STM has been used also to visualize the dynamics of oxygen-induced surface reconstruction on a variety of metal surfaces [2, 7-12], as well as in wet environments [13-15]. With oxygen on the metal surfaces as a function of time and/or temperature, one might see first a pure adsorbate, then induced reconstruction, followed by nucleation and growth of oxide islands and ending with bulk oxide formation. The STM studies can provide many elegant insights into the atomic mechanisms of oxygen adsorption but are limited to a few monolayers. Hence, these surface techniques do not provide insights into the nucleation and initial growth to coalescence of the metal oxides.

On the other hand, most high temperature oxidation investigations have been concerned with thicker, on the order of a few microns or greater, thermodynamically stable, oxide films. Figure 2.1 (b) is an SEM image showing the bulk growth of α-Al_2O_3 where a large crack, caused by tensile stress developed in the oxide scale under certain thermal-cycling conditions, is seen [16].

A classic and standard method for measuring the rate of oxide growth is thermogravimetric analysis (TGA), which measures the weight gain and oxygen consumption. The rate that the weight changes during oxidation provides information of reaction kinetics. Ideal oxidation behavior would be an increase in weight due to the formation of a protective oxide layer, and then slight weight change during oxidation, indicating that the material is being consumed very slowly. TGA can provide important information about the dominant migrating defects such as metal cations and/or oxygen anions vacancies and/or interstitials for transport of the cations and anions, as well as by electrons and/or holes for charge balance, when the measurements are performed as a function of oxygen partial pressure. However, TGA does not provide any structural information. Hence, nearly all classical theories assume a uniform growing film, where structural changes are not considered because of the lack of previous experimental methods to visualize this non-uniform growth in conditions that allowed for highly controlled surfaces and impurities [17, 18].

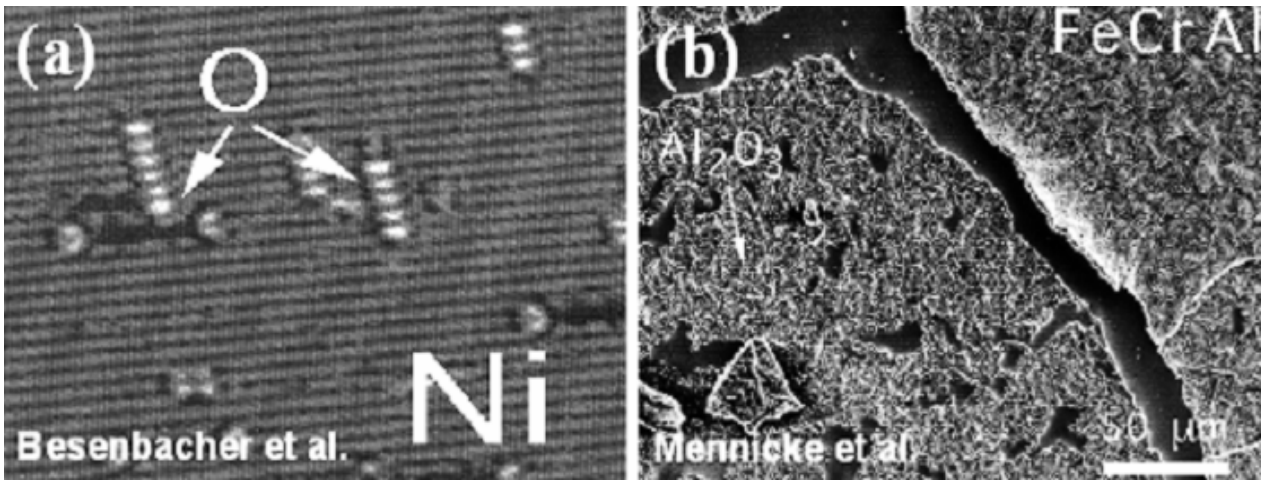

Figure 2.1 Comparison of oxygen atom surface adsorption and bulk oxide growth [1, 19]

It has been long recognized that the microstructure of the scale at the onset of oxidation plays an influential role in the oxidation rate at later stages in various materials [20-22]. Therefore, a complete understanding of oxidation processes should include the investigation of the initial stages of oxidation, i.e., the nucleation and initial growth of the oxides which occurs in the nanometers-size regime. Nucleation of the oxides on solid surfaces is complicated by many chemical components and reaction paths and the importance of the solid surface structures on the nucleation and growth must be considered.

2.2 PATTERN OF OXIDE NANOSTRUCTURES ON SURFACES

In the rapidly developing field of nanotechnology, the formation of ordered structures through surface processes has been intensively investigated because of potential applications and the intrinsic interest in structure with reduced dimension [23-26]. Controlled nanoscale pattern formation on surfaces has become one of the most important and challenging areas of nanoscience. Todate, two approaches for surface patterning have been pursued: top-down lithographic methods and bottom-up self-assembly methods. Lithographic nanopatterning of large areas is typically a slow process requiring expensive tools of limited availability. In contrast, self-assembly methods rely on intrinsic properties of the system and hold promise for creating complex, future-generation device architectures. Currently, various techniques with controlled deposition, such as molecular beam epitaxy (MBE), chemical vapor deposition (CVD), and physical vapor deposition (PVD), are used to grow self-assembled epitaxial nanostructures, in which coherent island formation occurs during the growth of lattice-mismatched materials systems. Such self-assembled nano-structures have been realized in semiconductor systems of Ge/Si [23, 26], GeSi/Si [27], and InAs/GaAs [28, 29]. These techniques can generate features with nanometer sizes but are limited in the types of patterns they can produce.

Oxidation can be viewed as a processing tool for creating oxide nano-structure on surfaces. The controlled formation of the oxide nanostructures would be technologically important for their potentially novel optical, magnetic and sensor properties. Review of the literature suggests that the work in this area has been quite limited to date, due in part to limited understanding regarding the evolution of oxide nanostructures on surfaces [24, 30].

2.3 HETEROEPITAXIAL GROWTH OF METAL OXIDE

The oriented growth of a crystalline material on the single crystal surface of a different material is called heteroepitaxy, and it has been extensively modeled [31-37]. Experimental and theoretical modeling results have demonstrated that the structure, strain and the energy of the

epitaxial interface play a significant role in determining the epitaxial orientation. Figure 2.2 (a) shows an example of the epitaxial growth of Ge islands on a Si(100) surface .

Oxidation potentially involves nucleation and growth, surface diffusion and solid state reactions, and this bears a striking resemblance to heteroepitaxy. Figure 2.2(b) shows the oxidation of Cu(100) film, where the epitaxial relationship between the oxide islands and the Cu substrate was revealed by the selected area electron diffraction pattern (SAD). These two dramatic systems, thin film growth by MBE, CVD, PVD, etc. and oxide formation by oxidation, both show the epitaxial growth with substrates. Yang, et al., have shown that heteroepitaxy theory describes surprisingly well the nucleation and growth of Cu_2O islands on Cu(100) [38-40]. Since an oxidation reaction is generally a multi-step process which is more complex than thin film growth, the modeling of oxidation by using the epitaxial theory should incorporate the additional complexities in oxidation, such as dissociation of O_2 and the surface chemical reaction.

The goal of this research project is to extend the investigation to Cu(110) and Cu(111) and gain more fundamental understanding of the effect of strain and surface structure on oxidation.

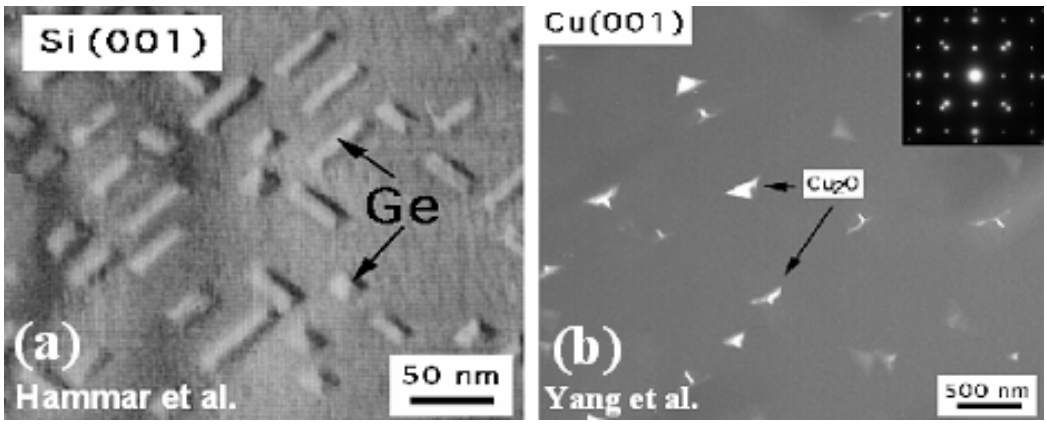

Figure 2.2 Comparison of Ge on Si heteroepitaxy and Cu_2O nucleation on Cu(100)

2.4 *IN SITU* UHV-TEM OF OXIDATION

In order to establish a complete understanding of the oxidation mechanisms, a thorough knowledge of the microstructure of the oxide scale is essential. In the past, much of this information was provided by SEM in conjunction with electron probe microanalysis of bulk

samples [20-22]. However, to understand the oxidation properties on a microstructural scale, the use of TEM is necessary. Most TEM studies of oxide scales have been carried out with oxide films stripped from the metal. Such a technique has the disadvantage of changing the relative position of the oxide film on the substrate and prohibits accurate determination of orientation relationships between the oxide and the base metal [21, 41-43]. Furthermore, one cannot study the initial stages of the oxide scale since one cannot strip off discontinuous layers. Previous investigators have recognized the importance of *in situ* oxidation techniques and have studied the initial stages of oxidation by *in situ* techniques, including TEM, but obtaining an atomically clean surface was impossible with previously available experimental techniques [41, 43-48]. Impurities play a dramatic role in changing the progress of oxidation [49]. The surface impurities must be controlled to gain quantitative and fundamental information about oxidation. Some the previous *in situ* TEM investigations involved a side chamber for oxidation processing, then the samples were transferred to the TEM column for observation. The nucleation, initial growth, and structure changes of the oxide were not followed in real time. Therefore, some important nucleation information during oxidation was missing, which is critical for understanding oxidation mechanisms.

It has become increasingly apparent that detailed experimental data along with a sophisticated theoretical treatment of the initial stages of a chemical treatment on a metal surface are essential to a fundamental understanding of oxidation. We are presently using a novel technique, *in situ* UHV-TEM, which combines the correct range in spatial resolution for bridging the gap between nucleation and initial growth of oxide as well as providing the UHV environment necessary for atomically clean surfaces. The advantages of *in situ* TEM experiments include visualization of oxidation processes in real time and information on buried interfaces. The microscope provides dynamic information from the nucleation to the initial growth and coalescence of the oxide islands at the nanometer scale. One can now see structural changes under controlled surface conditions. This experimental tool provides unique and critical data of these gas surface reactions in a wide pressure and temperature range needed for a fundamental understanding of the atomistic kinetics.

Visualizing the oxidation process at the nanometer scale with *in situ* experiments under ultra high vacuum conditions will provide essential insights into the complex kinetics and energetics of nano-oxide formation. First, it will shed light on the oxidation kinetics. Secondly, it allows us

to distinguish between models for the formation process of nanostructures, kinetics versus energetics control. *In situ* UHV-TEM allows us to study the nucleation and growth processes of oxide, provides a unique view of dynamic reactions as they occur, and enables us to understand and, therefore, manipulate surface reactions. The dynamic information obtained from these *in situ* experiments enables us to understand oxidation mechanisms in the nanometer regime and to control the oxide pattern on the surface.

2.5 OXIDATION OF COPPER

Copper is used in electronic packaging and ultra-large scale integrated (ULSI) devices due to its low resistivity and high electro-migration resistance [50]. However, one obstacle in the way of widespread application of Cu technology is that it oxidizes at a significant rate at temperatures as low as room temperature, forming a non-protective oxide scale. Especially, as the dimensions of interconnects approach nanometers, the passivation of these interconnects will become a critical issue. No single theory has yet been formulated to explain the phenomenon of Cu oxidation but, in general, the results of a number of studies indicate that low temperature oxidation (<250°C) follows an inverse logarithmic rate law, at intermediate temperatures a mix of both parabolic and cubic behavior is noted, and as the temperature increases, the parabolic rate dominates [50]. The activation energy of Cu oxidation below 500°C has been reported to be approximately 85 kJ/mol for bulk Cu and 75.5 kJ/mol for thin films oxidized under low oxygen partial pressures [50].

Cu is also considered to be a model system for the oxidation of metal for the fundamental understanding of oxidation mechanisms and has been studied extensively [47, 48, 51-56]. Figure 2.3 shows the phase diagram of Cu-O. Copper forms two thermodynamically stable oxides, Cu_2O and CuO. Cu_2O is simple cubic lattice (space group $P_{N\bar{3}M}$) with 4Cu and 2O atoms in its basis, and a lattice parameter of 4.22Å. The Cu atoms form a FCC lattice and the O atoms form a BCC lattice, where each O atom is surrounded by a tetrahedron of Cu atoms. CuO has a monoclinic structure (space group $C_{2/C}$) with lattice parameters of a=4.7Å, b=3.4Å, c=5.1Å and β=99.5°. Some other metastable copper oxides with Cu_4O, Cu_8O, $Cu_{64}O$, $Cu_4O_{0.75}$ structures and two types of superstructures, called Cu_4O-S_1 and Cu_4O-S_2, which have the crystal structure

similar to Cu_2O, were also observed by high-resolution transmission electron microscopy (HRTEM) in the early stages of oxidation of copper [57-61]. Cu is a FCC metal with a lattice parameter of 3.61Å. In this work, Cu films with different orientations, Cu(100), Cu(110) and Cu(111), are chosen as model systems to investigate the kinetics of the initial stage of oxidation of copper films. For the temperatures, (T<1100°C), and very low oxygen partial pressures, ($P(O_2)$<0.1 torr), used in our experiments, only cubic Cu_2O is expected to form [62].

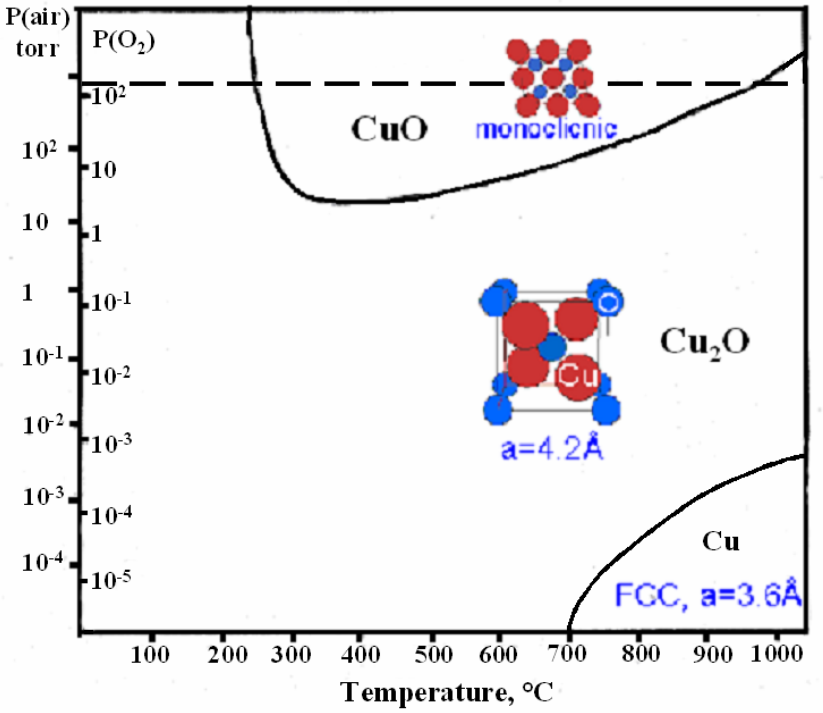

Figure 2.3 Phase diagram of Cu-O system [62]

3.0 EXPERIMENTAL PROCEDURES

3.1 INTRODUCTION

The Cu films were oxidized *in situ* within a modified TEM. Selected samples were then examined *ex situ* by atomic force microscopy (AFM), scanning electron microscopy (SEM), and high resolution transmission electron microscopy (HRTEM). This equipment resides at the Frederick Seitz Materials Research Laboratory, the University of Illinois at Urbana-Champaign.

3.2 *IN SITU* ANALYSIS

3.2.1 Experimental setup

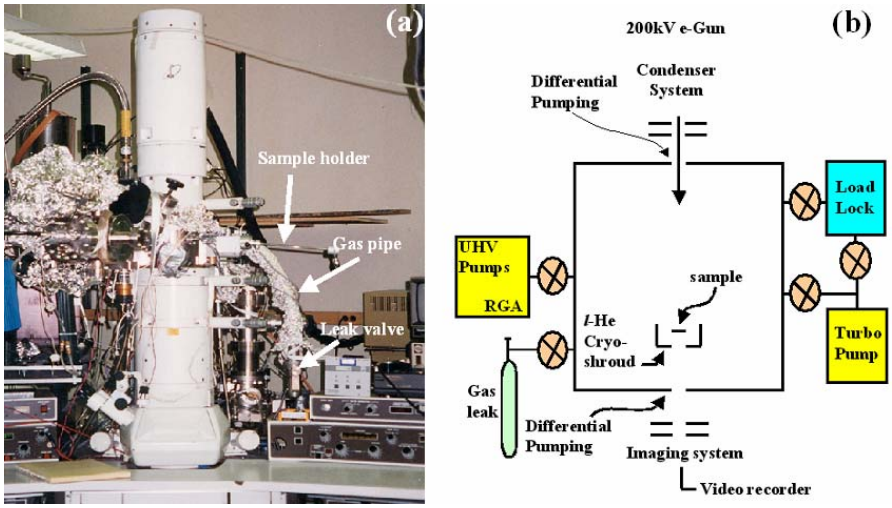

Figure 3.1 The modified *in situ* UHV-TEM (a) and its schematics drawing of the main elements of the system (b).

The primary tool for studying the oxidation of the Cu films was an *in situ* UHV-TEM, as shown in Figure 3.1, and the main elements of the system are illustrated in the schematic drawing. The electron microscope was a modified JEOL 200CX TEM with a top loading sample holder [63]. The additional pumping on the sample chamber consisted of a combined Thermionics ion/liquid nitrogen cooled sublimation pump and a Balzers turbomolecular pump. Furthermore, a cryoshield surrounds the specimen cartridge which is cooled via conduction through a Cu wire to a cold finger held at liquid nitrogen or helium temperature. The pressure in the sample region was determined by an ion gauge attached above the polepiece.

Typical pressures in the sample chamber were 2×10^{-7} torr with just the turbo pump operating. The pressure was improved by an order of magnitude by the ion pump. The pressure at the actual sample location inside the objective lens polepiece could not be measured directly, but the Si (001) (2×1) surface reconstruction was found to be stable for ≈40 min at room temperature with the liquid He cryoshroud operating [64]. Hence, a pressure in the low 10^{-9} Torr range at the sample position can be inferred. Reactive gases, e.g., methanol vapor or oxygen could be introduced into the sample chamber with the ion pump valved off. Partial gas pressures of up to 10^{-4} torr could be achieved with the electron beam operating. By isolating the TEM column, 1 atmosphere oxygen pressure is achievable. The microscope was typically operated at 100kV. The thin film samples were mounted in the sample holder on a specially prepared Si support, which was heated by electrical resistance.

3.2.2 Sample preparation

The Cu films used in this work were produced by e-beam evaporation of 99.999% pure Cu pellets on irradiated NaCl. The films were grown in a UHV evaporator system with a base pressure of 1×10^{-9} torr. The deposition rate was measured by quartz crystal thickness monitors and the substrate was heated by an e-beam with a temperature stability of ±5 K. Prior to mounting the sample in the evaporator, the rocksalt was cleaved in air. Cu and other metals can be grown epitaxially, i.e. $(001)_{metal}\|\ (001)_{NaCl}$, $<001>_{metal}\|\ <001>_{NaCl}$, on rocksalt if appropriate deposition rates and growth temperatures are used [65-67]. The growth parameters for Cu films

were the same as those in previous studies [68, 69]: the deposition rate was 5Å /s and the substrate temperature, 250°C. The thinnest films that could be obtained were 400Å thick and included some holes. Cu films thicker than 600Å were continuous. Cu films were grown from 400-1000Å in thickness.

The films were cut into the desired size and then floated off the rocksalt in deionized water. Residual rocksalt on the films was removed by transferring the films into fresh water several times. They were then floated onto the sample supports, depicted in Figure 3.2 (a), which were lithographically produced Si pieces, 350 μm thick and 2 by 3 mm in size, with a 1 μm Si_3N_4 layer on top. The size of the central hole extended from 400 μm by 400 μm on top to 800 μm by 800 μm at the bottom of the Si piece. Once the water had dried off, the sample could be mounted in the sample holder (Figure 3.2 (b)).

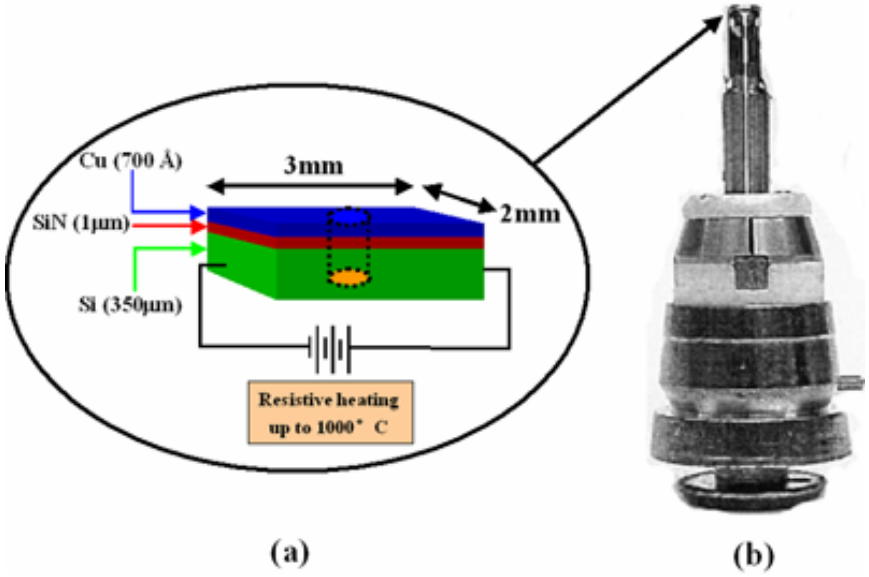

Figure 3.2 Si_3N_4 sample support (a) and sample cartridge (b). In the microscope, the sample cartridge was mounted upside down.

The samples were mounted in the sample holder shown in Figure 3.2(b). Two metal posts, electrically isolated, supported the sample, which was secured in place by two spring-loaded clips. The sample was oriented such that its top side (film side) faced the support posts. The top loading design of the microscope required this "upside down" orientation so that once inside the microscope, the top side of the sample faced the electron beam. Once the sample cartridge was

inserted into the polepeice, springs pressing against the lower part of the cartridge ensured electrical contact. The sample was heated by passing a current through the Si support. Therefore, care had to be taken that the metal film did not cause a short circuit. The design of the microscope, especially the top loading mechanism, did not allow for a thermocouple attachment to measure the sample temperature. Therefore, it was necessary to rely on a calibration curve which related the power (P=IV) drop across the sample to the actual temperature. This type of temperature measurement, however, depends strongly on the geometry and material of the sample support. The varying sizes of the metal thin films on top of the Si_3N_4 should not affect the temperature measurement significantly.

In order to perform the temperature calibration, a sample was mounted in the cartridge, which was then placed inside a bell jar evaporator. A thermocouple was attached to the sample and electrical connections were made to the cartridge to measure T as a function of the power passed through the Si holder. Furthermore, temperatures above 800 K were also measured with an infrared pyrometer through the glass jar, in good agreement with the thermocouple measurements.

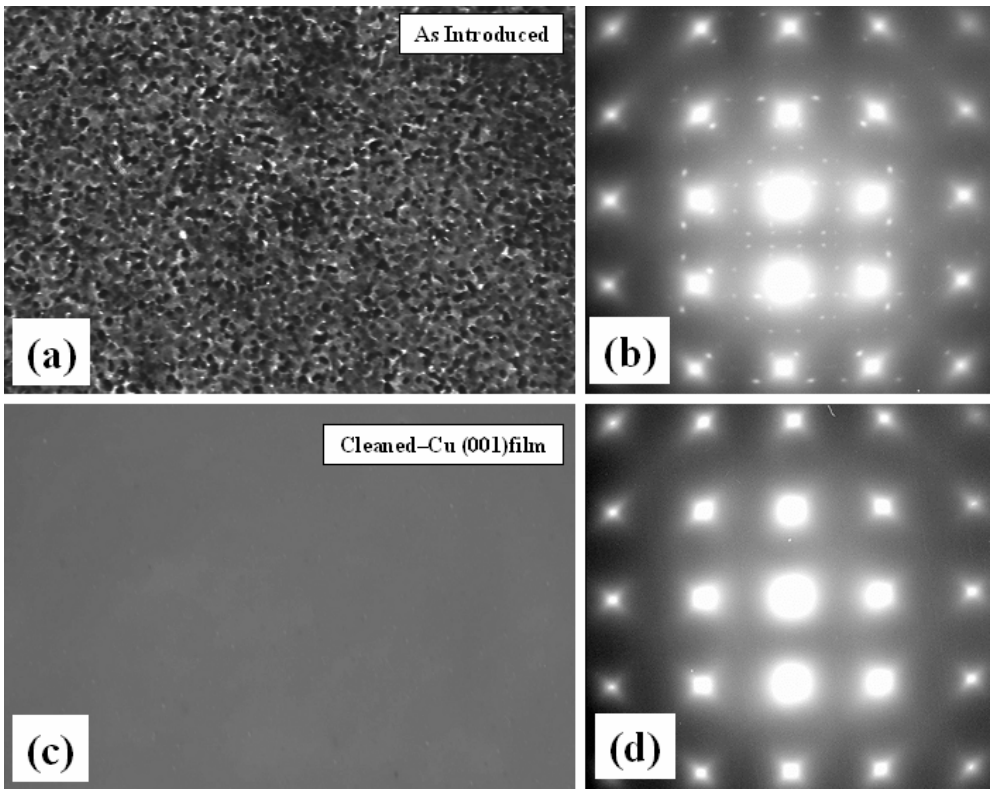

Figure 3.3 The *in situ* cleaning of Cu film by methanol vapor at 350°C

The voltage could not be measured directly across the sample and therefore included the voltage drops due to contact resistance to the sample itself. The resistance calculated from the measured current and voltage values, nevertheless, were consistent with the temperature-resistance dependence of a semiconductor [64]. This implies that any contact resistance is small and can be neglected. Additional temperature measurements were calibrated with the phase transition temperature of Cu_3Au [64], and the surface roughening temperature (700°C) of the Cu(110) surface [70]. The temperature change of the Si piece (2mm×3mm×350μm) due to the enthalpy change for the oxidation of the small amount of Cu (1.5mm×1.5mm×70nm) is ~ 0.1°C. This negligible effect was also experimentally confirmed by the oxidation of the roughened Cu(110) surface at ~710°C. No structural change on the roughened surface was observed with the continuous formation of oxide islands, however, thermal faceting was observed at ~800°C inside the TEM without any oxidation reaction.

The films needed to be cleaned inside the microscope. In the case of Cu, the native oxide (Cu_2O) on the films had to be removed. This was accomplished by leaking in methanol vapor at a partial pressure of 5×10^{-5} torr, while keeping the sample at 350°C. The methanol decomposes on the film surface to yield gaseous water, formaldehyde (CH_2O), carbon monoxide and carbon dioxide [71], which are pumped away from the surface leaving an oxide free film. This process can be followed clearly in the TEM. Figure 3.3 shows a bright field micrograph (a) and its selected area diffraction pattern of a Cu(001) surface before and after the cleaning procedure (c), (d). The diffraction spots due to epitaxial Cu_2O have disappeared, and only the intensity from the bare Cu surface remains. Sub-monolayer coverages cannot be detected easily in the diffraction.

3.3 *EX SITU* ANALYSIS

3.3.1 Atomic force microscopy (AFM) analysis

The surface topography was also measured on selected samples by AFM. The measurements were done on the both parts of the sample where the Cu film was supported by the Si/Si_3N_4 sample holder and on the unsupported thin film (hole area). This had the great advantage that

TEM data, acquired in the *in situ* UHV-TEM, and AFM results, were available from the same sample. In AFM, like in all scanning probe microscopy techniques, a sharp probe is scanned across the surface and the tip-sample interactions are monitored. AFM is usually done in one of two modes, contact mode or tapping mode.

In contact mode AFM, a tip, attached to the end of a cantilever, is scanned across the sample surface, while the cantilever deflection is measured with the help of a laser and a split photodiode detector. The split photodiode detector consists of two closely spaced photodiodes. If the cantilever is displaced, one photodiode collects more light than the other one and the difference in the signal from both photodiodes, normalized by their sum, is proportional to the cantilever deflection. A feedback loop maintains a constant deflection for each point on the surface by moving the cantilever vertically. In this fashion, the force between the tip and sample, which typically ranges from nN to μN, remains constant. The vertical movements of the scanner are recorded as a function of lateral position on the sample and a topographic image of the sample surface is formed. The radius of curvature of contact mode tips is usually 20-60 nm.

Contact mode AFM is, in theory, the only AFM technique that allows as to record atomic resolution images [72], if the measurements are done under UHV conditions and on atomically flat surfaces. In air, however, the normal forces on the tip can be high due to capillary forces from the adsorbed fluid layer. This, in combination with lateral (shear) forces on the tip, degrades the image resolution and can damage soft samples. Furthermore, the large tip radius limits the usefulness of contact mode AFM in measuring surface features with dimensions in the nanometer range and a high aspect ratio.

All AFM scans were checked for imaging artifacts by rotating the scan directions. “Real” features of the sample follow this rotation, while artifacts usually do not. Occasionally, the image resolution was lost during repeated scans of one area. This is typically caused by loose debris on the sample, which attaches itself to the tip.

The size of the data was always 512×512 pixels and the scan speed less than 2 Hz. The following filter in second order was applied to the raw data. Flatten modified the image on a line-by-line basis. It removed the offset in the vertical direction between scan lines by calculating a least square fit polynomial for a scan line and subtracting this fit from the same scan line.

3.3.2 High resolution transmission electron microscopy (HRTEM) analysis

The design of the JEOL 200CX as a microscope with the top loading holder increased the stability of the sample and minimized drift, especially during annealing. The drawback was that the sample could not be tilted due to the modifications for *in situ* annealing. Some samples were also studied *ex situ* in a JEOL-2010F. The 2010F is an energy filtering, field-emission analytical TEM/STEM. The point-to-point resolution of the microscope is 0.24nm and the microscope is equipped with a STEM system and capable of tilting 40 degrees on one axis and 30 degrees on the other. It is ideal for small probe work including: HAADF STEM, nanodiffraction, and spatially resolved EELS and EDS. It operates at 200kV and uses a Schottky field emitter. The 2010F is equipped with an energy filter to filter both images and diffraction patterns as well as act as an energy-loss spectrometer. The system is capable of EDS/EELS mapping, holography, and *in situ* heating and cooling. Both intensified video rate and slow-scan CCD cameras are available. The system is controlled by the JEOL FasTEM system allowing total computer control of the system.

3.4 LIMITED EFFECTS OF SURFACE DEFECTS ON OXIDE NUCLEATION

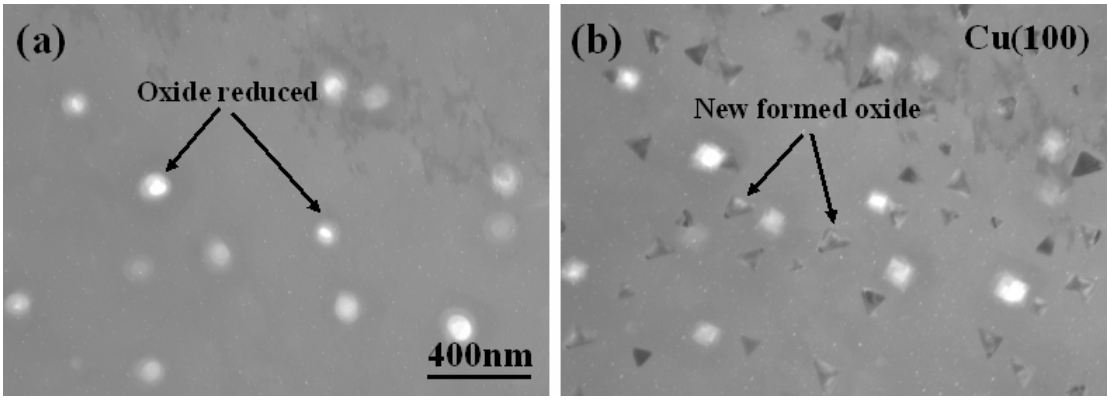

Figure 3.4 The limited effects of surface defects on the oxide nucleation on Cu(100), (a) the Cu film after oxide reduction by methanol gas at 350°C, where the areas with bright contrast are the thinned regions due to oxide reduction; (b) repeated oxidation on the same surface area, where the new oxide islands have a random distribution, not necessary at the same sites of oxide reduction.

A particularly important question is the role of surface defects and topology in the initial oxide nucleation. It is known for semiconductor thin film growth that surface steps and ledges are often preferential nucleation sites during thin film deposition. Milne and Howie [44] have proposed that surface steps play a significant role in the nucleation of copper oxides during oxidation of copper. Milne [73] has observed large faceted oxide islands along surface steps by scanning reflection electron microscopy, but was not able to observe the nucleation at these steps. Hence, it is necessary to clarify the role of surface defects in the oxide nucleation, which is very important to understand the nucleation and growth kinetics of oxide islands.

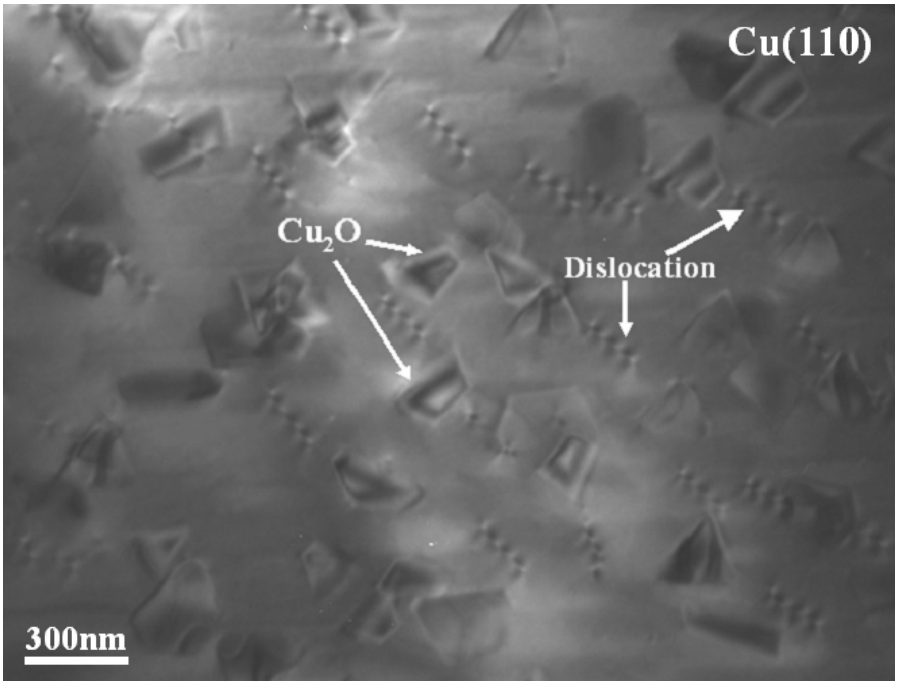

Figure 3.5 The oxidation of Cu(110) film with a lot of dislocations, where the oxide islands have a random distribution, and the dislocation sites are not the preferred nucleation sites.

The formation of oxide islands on surfaces followed by reduction will create surface templates which have concentrated surface defects at certain sites. If it is true that the surface defects are the preferred nucleation sites, it will be expected that the repeated oxidation on the same surfaces results in the formation of oxide islands at the areas with the concentrated surface defects, and the islands do not have a random distribution. Figure 3.4 shows a typical example of oxidation, reduction, followed by oxidation experiments on Cu(100) surface. The reduction of oxide islands resulted in thinned regions at the island sites which have bright contrast in Figure

3.4 (a). These thinned regions should have a large number of surface defects. Figure 3.4 (b) corresponds to the same surface area after the oxidation again, where the oxidation temperature was ~ 350°C, and oxygen pressure was ~7×10^{-4} torr. It is noted that the new oxide islands in Figure 3.4 (b) were not nucleated at the same sites, and the islands still have a random nucleation distribution on the surface. The experimental observation demonstrates that surface defects play a very limited role in the initial stages of oxidation.

Although surface defects/dislocations do not play an important role in the oxide nucleation and growth, the films with continuous structure are very important for a quantitative understanding of the oxidation kinetics. Figure 3.6 shows an example of oxidation of Cu(100) film, where the film contains grain boundaries. It is found that the grain boundary is the preferred oxide nucleation site. The oxide islands are aligned along the grain boundary, and these oxide islands have a larger average size than the islands formed on the flat surface area.

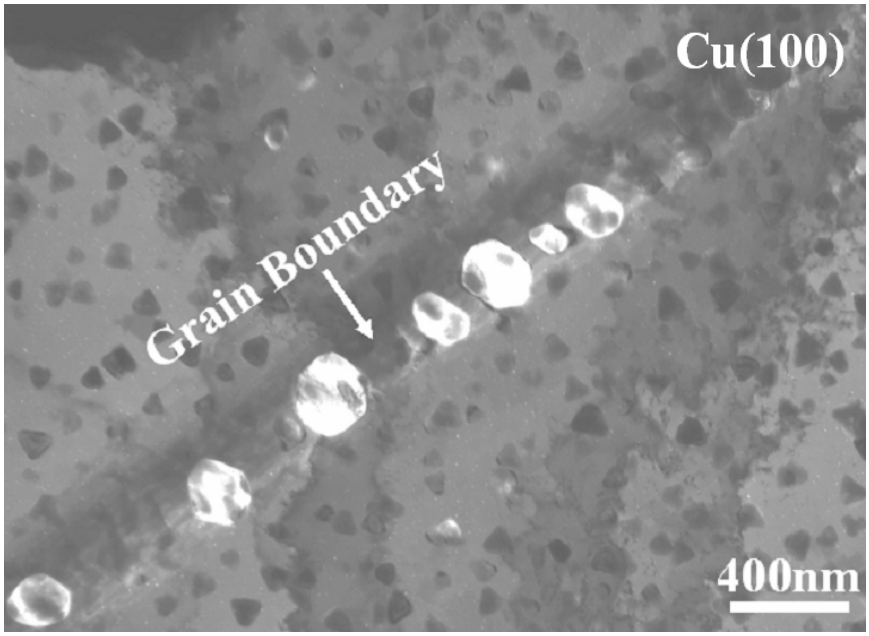

Figure 3.6 The oxidation of Cu(100) film at 400°C and oxygen pressure of 0.01 torr, where grain boundary structure is present in the film. The alignment of oxide islands along the grain boundary indicates that the grain boundary is the preferred nucleation site for oxide islands, also, the larger average size of the oxide islands nucleated along the grain boundary indicates the oxide islands have a faster growth kinetics than the islands formed on the flat area.

It is interesting to note here that surface defects and dislocations play a very limited role in the nucleation/growth kinetics of oxide islands, which is very different from thin film growth, where the surface defects/dislocations are the preferred nucleation sites, and also affect the growth kinetics of the islands. In the following oxidation experiments, we assume the oxide islands have a homogeneous nucleation site on flat and continuous Cu surfaces, where each site on the surface has an equal probability for being a nucleation site.

4.0 Cu(100) OXIDATION

The formation of the Cu_2O oxide islands has been investigated by oxidizing Cu(100) thin films at different temperatures (150°C ~ 1000°C). It is found that dramatically different morphologies of oxide nanostructures were achieved by an appropriate choice of the oxidation temperature. During oxidation at low temperatures, (T < 400°C), the oxide islands adopt a triangular shape, between temperatures of 400°C-600°C, the islands appear more symmetrical. We focused on two unusual nanostructures. Quasi-one-dimensional Cu_2O structures with aspect ratios as large as 40:1 were formed at the oxidation temperature of 600°C. The *in situ* observation data on the elongation of Cu_2O islands agree with the energetic calculations based on the balance between surface and interfacial energies and the elastic stress relaxation in the three dimensional islands (Tersoff and Tromp model). A peculiar pyramid structure, hollow Cu_2O pyramids, was formed when the Cu(100) films were oxidized at 1000°C. A model based on the plastic slip caused by the volume change from the oxidation of Cu to Cu_2O, is proposed to quantitatively account for the formation of this structure.

4.1 EFFECT OF TEPERATURE ON THE MORPHOLOGY OF OXIDE ISLANDS

The substrate temperature is of major importance for surface oxidation since dissociation of the oxidizing species, surface diffusion, surface structural changes, etc., are thermally activated processes. Therefore, the Cu_2O island formation was studied as a function of oxidation temperature in the range of 150°C to 1000°C at a constant oxygen partial pressure of $5x10^{-4}$ torr. Oxide island formation was not observed for several hours at oxidation temperatures below 150°C under such low oxygen pressure. Three-dimensional island formation was observed for oxidation at all temperatures higher than 150°C. For all of the temperatures that we have

examined, we confirmed by selected area electron diffraction (SAD) that the oxide formed during oxidation is the epitaxial Cu_2O on the Cu surface.

4.1.1 Experimental observations

Figure 4.1 contains bright field TEM images showing the morphology of Cu_2O islands formed on Cu(001) at different oxidation temperatures. At 350°C, only triangular in cross-section islands formed (Figure 4.1 (a)). The island size increased with continued exposure to oxygen, but the island shape did not change. At elevated temperatures, between 400°C and 550°C, the islands exhibited a shape change from triangular to square or round-based islands as they increase in size due to the continued exposure to oxygen as shown in Figure 4.1 (b).

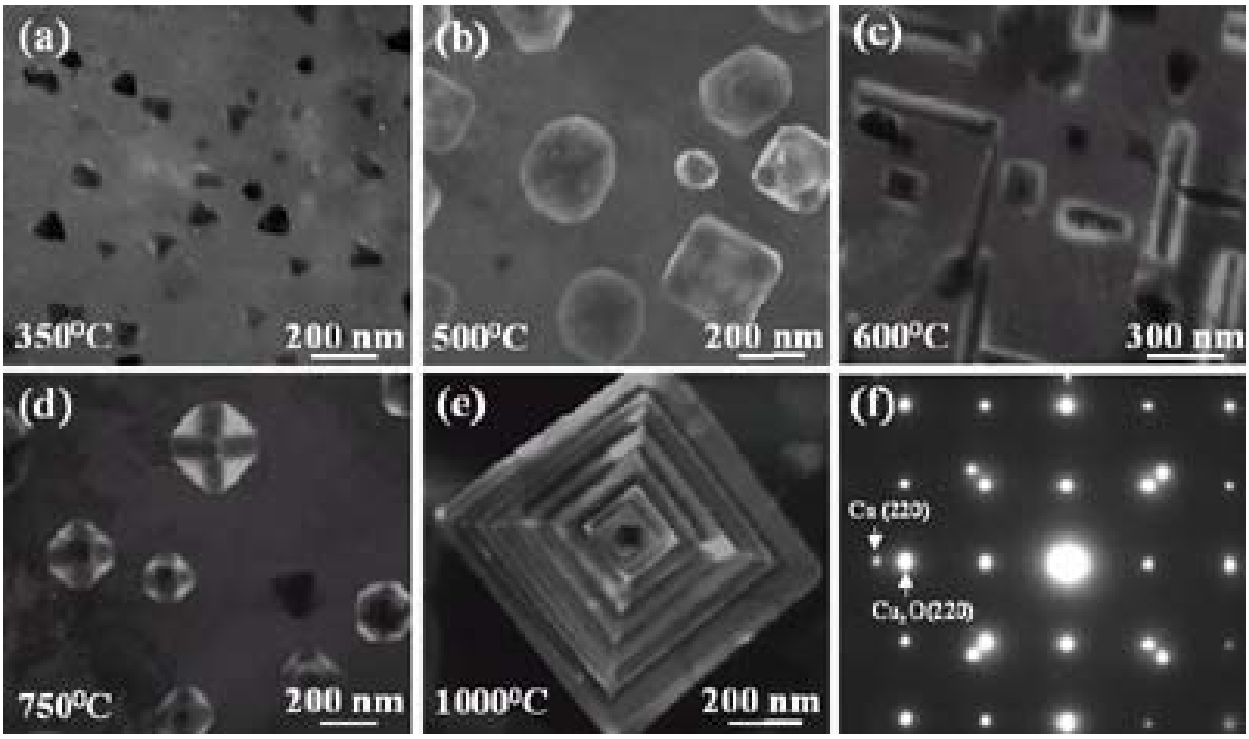

Figure 4.1 The morphology of Cu_2O islands formed during *in situ* oxidation of Cu(001) at an oxygen partial pressure of $5x10^{-4}$ torr and oxidation temperatures of (a) 350°C, (b) 500°C, (c) 600°C, (d) 750°C and (e) 1000°C, (f) epitaxial relationship between Cu_2O and Cu(100).

In a narrow temperature regime near 600°C, elongated Cu_2O islands formed, as shown in Figure 4.1 (c). The elongation directions of the islands are always along the two orientation pairs

of the four crystallographic orientations, i.e, (011)Cu and $(0\bar{1}\bar{1})$Cu, $(01\bar{1})$Cu and $(0\bar{1}1)$Cu and roughly equally distributed. We have observed elongated islands with aspect ratios as large as *40:1*. Figure 4.2 shows an example of the highly elongated Cu_2O islands formed at this temperature.

Oxidation at temperatures between 650-800°C resulted in the formation of pyramid islands, which have a distinctive cross-hatched pattern, as shown in Figure 4.1 (d). The islands are faceted and are aligned with each other with the edges parallel to <011>Cu directions. When the Cu film was oxidized at temperatures between 800-1000°C, pyramids with terraces and ledges formed, as shown in Figure 4.1 (e). The pyramid terraces have roughly equal width distributions. The *in situ* observation revealed that these terraced-pyramids developed by nucleating and growing new terraces at the base terrace of the pyramids.

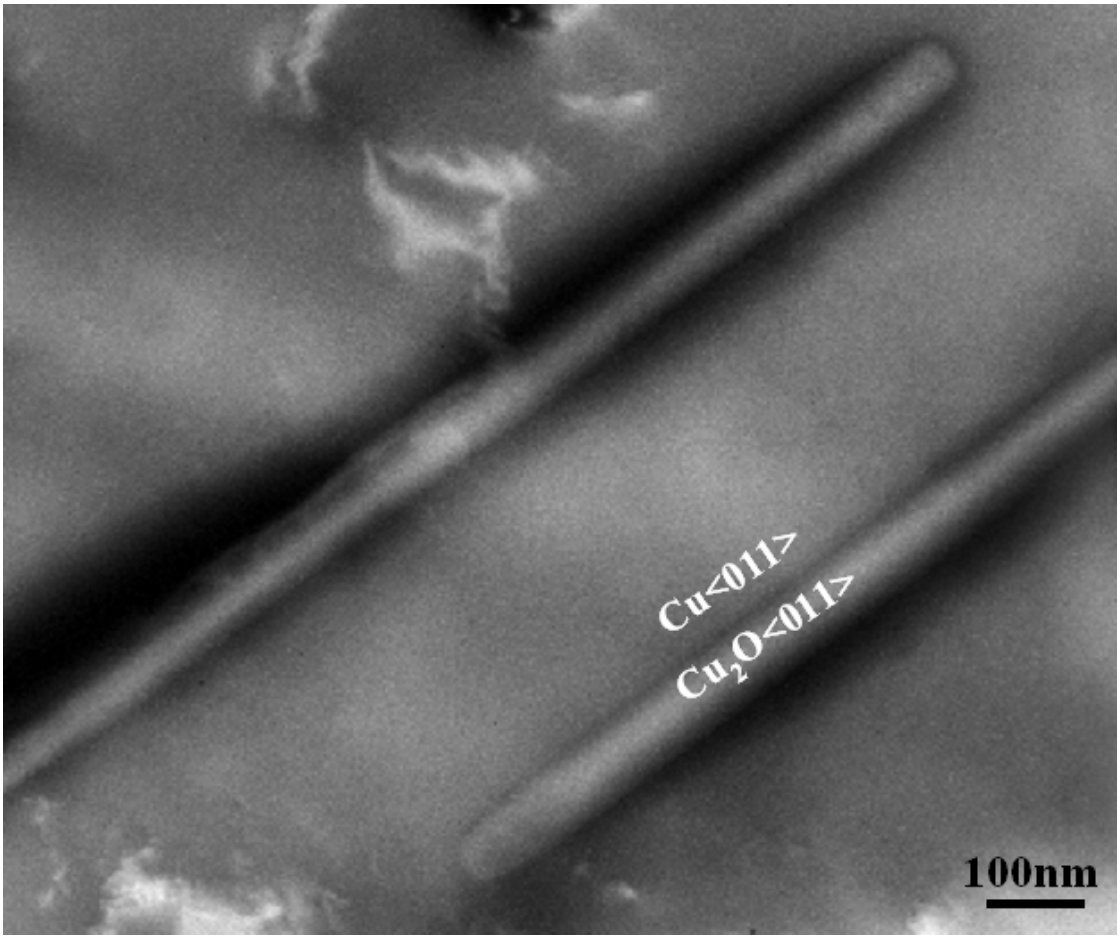

Figure 4.2 Highly elongated Cu_2O islands formed at 600°C.

Figure 4.3 presents AFM images of typical Cu_2O islands formed at different temperatures. Figure 4.3 (a) shows an oxide island formed at T=350°C. The surface topography reveals that the island has a flat top, where their height is approximately equal to 30nm. Figure 4.3 (b) is the AFM image of an elongated island formed at T=600°C. The surface profile shows that the islands have a flat top, and the contact angle θ between the edge facet and the substrate is *35*°. The height of the islands above the Cu film surface is approximately 15nm. Figure 4.3 (c) corresponds to an island formed at T=800°C, where the island terraces are visible. The island height is 40nm, which is much smaller than its lateral size.

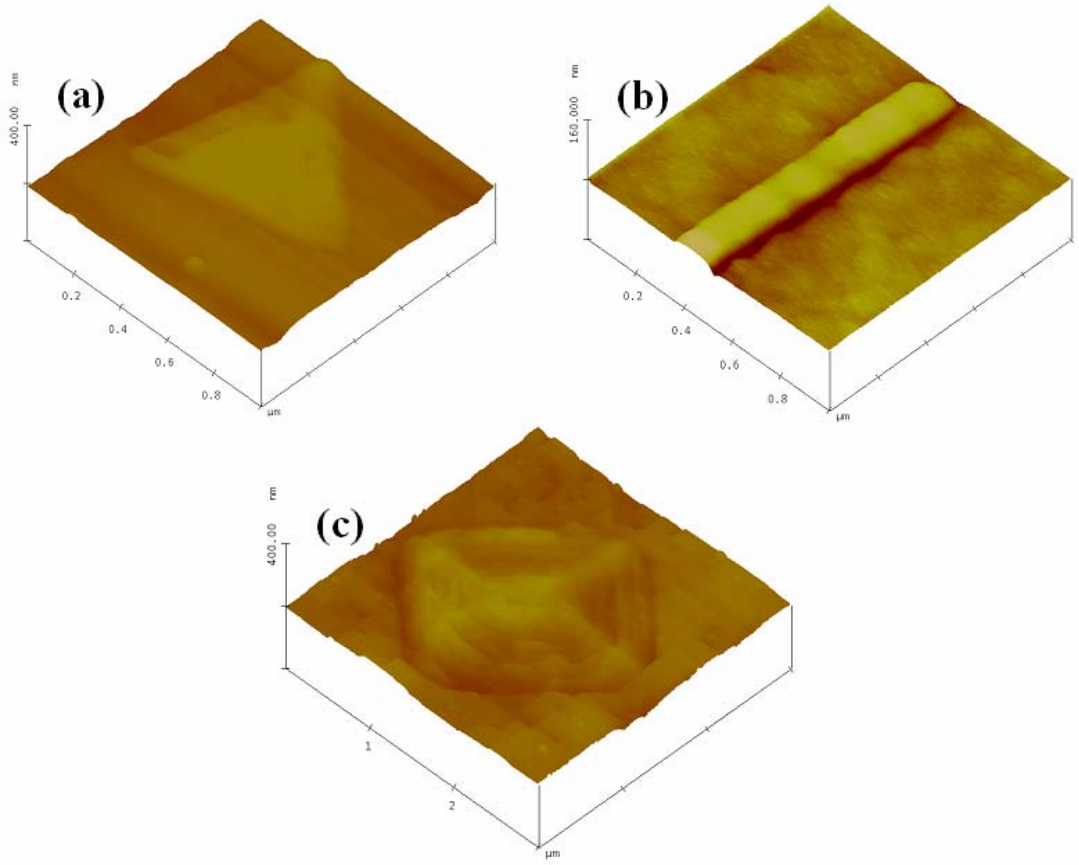

Figure 4.3 AFM images of typical (a) triangular (T=350°C), (b) elongated (T=600°C), and (c) pyramid islands (T=800°C).

Both *in situ* TEM and AFM investigations revealed that the edges of all of the square shaped islands formed at higher temperature, as shown in Figure 4.1 (b, c d. e), are along {011}Cu, and they have roughly equal growth rates along these four equivalent crystallographic orientations.

4.1.2 Discussion

We have shown that a wide variety of oxide nanostructures can be created by only selecting the oxidation temperature. The *in situ* UHV-TEM observations revealed the dramatic sensitivity of the oxide island morphology to oxidation temperature. During oxidation at low temperatures, (T < 400°C), the oxide islands adopt triangular shapes, but at temperatures higher than 400°C, the islands have a more symmetrical geometry. It has previously been shown that the initial stages of Cu(100) oxidation are surprisingly similar to heteroepitaxy in thin film growth, where oxygen surface diffusion is the dominant mechanism [39]. In heteroepitaxial growth, only a few investigators have examined the effect of the substrate temperature on the thin film growth and morphology such as Cr on Cu substrates [31], indium-doped tin oxide films [74] and plasma enhanced chemical vapor deposition (PECVD) of polycrystalline Si films [75]. Yet, only Afify, *et al*., [74] noted a distinct change in the island morphology due to the substrate temperature, where dendritic growth was noted at higher temperatures for indium-doped tin oxide films. A possible reason why this dramatic effect of temperature on the film morphology has not been widely observed in other systems could be that the temperature ranges previously investigated were considerably smaller (only ~200°C) than the temperature range we examined (150°C to 1000°C).

The oxide morphology is controlled by kinetic and thermodynamic factors during the oxidation process. *In situ* observations can provide insight which enables distinguishing between morphologies due to kinetic or thermodynamic considerations. It is reasonable to expect that temperature affects the kinetics and/or energetics of the oxide formation.

The formation of Cu_2O islands will induce strain in the Cu film and the oxide islands due to the large lattice mismatch. Copper is a face-centered cubic metal, with a lattice parameter a=3.61Å, and Cu_2O is cubic with a lattice parameter a=4.22Å. Cu_2O has a thermal expansion coefficient of 1.9×10^{-6} $°C^{-1}$, and Cu has a thermal expansion coefficient of 17×10^{-6} $°C^{-1}$ [76]. With increasing temperature, the lattice mismatch becomes smaller, and, hence, this lattice mismatch induced strain becomes smaller. This may explain the triangular shape at low temperatures, where the strain is high and then the interfacial strain energy will be minimized by minimizing the interfacial area. An interface with circular shape should have the smallest area. However, the anisotropy in interface and surface energy and the relatively slow growth kinetics

may make the triangular shape the preferred shape of the oxide islands formed at 350°C. At higher temperatures, there is less lattice mismatch and therefore reduced interfacial strain with increasing temperature. Hence, the chosen interfaces will be along the low energy interfaces (such as the low index planes). A second effect of the temperature is on the growth kinetics of the oxide islands. As temperature increases, there would be enhanced oxygen surface diffusion, and the islands could approach more closely the equilibrium shape. Thus, the oxide islands formed at low temperatures, (350°C), have a low symmetry (triangular shape) and the islands formed at high temperatures exhibit higher symmetry (round and square shapes). Therefore, the competition among differing energies and kinetics at the different temperatures gives rise to a rich variety of structure during oxide growth.

4.2 FORMATION OF ONE DIMENSIONAL Cu_2O STRUCTURES AT 600°C

Formation of nanostructured islands on surfaces has been intensively investigated. One intriguing aspect in these systems is the tendency of the islands to change their shape as they increase in size. The details of this transition process are complex and temperature dependent. The underlying cause of shape transitions is a competition between the interfacial energy and surface energy in an island. Existing estimates of transformation volumes and equilibrium island shapes generally compare energies of the competing island shapes, thus providing a necessary but not sufficient condition for transformation to occur.

Tersoff and Tromp have given an "elastic strain relief" model to describe how strained epitaxial islands, as they grow in size, may undergo a shape transition [77]. Below a critical size, islands have a compact symmetric shape. However, at a larger size, they adopt a long thin shape, which has an energy minimum for the system because of the tradeoff between surface/interfacial energies and stress relaxation in the three dimensional islands due to the lattice mismatch between the substrate and epitaxial film. The formation of rectangular hut structures was observed by Mo, *et al.* [26], during the initial growth stages of Ge on Si(100), and the similar elongated island structures were also observed in many other systems created by molecular beam epitaxy (MBE) such as Ag/Si(100) [77, 78], GaAs/Si(100) [79], CoSi/Si(100) [80, 81], Au/Mo(111) [82], and InAs/InP(100) [83]. Here, we present the first observations of a surface

chemical reaction where the nanorod transition is observed, thereby demonstrating a greater universality of the elastic strain relief model proposed by Tersoff and Tromp.

4.2.1 Experimental observations

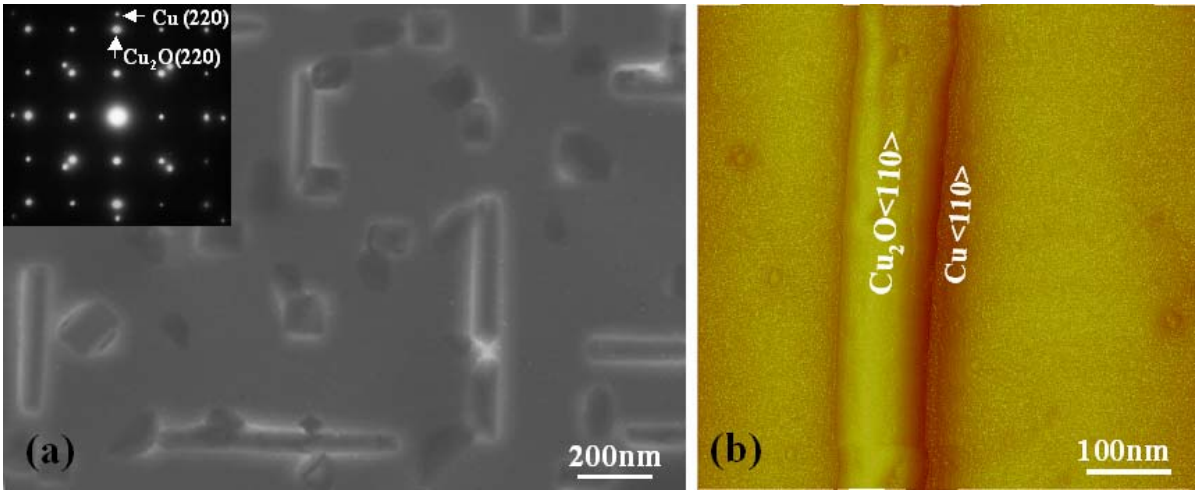

Figure 4.4 (a) The Cu_2O islands formed by oxidation of Cu(100) at constant oxygen partial pressure of 8×10^{-4} and temperature of 600°C. The square shaped islands are smaller or near to the critical size of ~110nm. Elongated islands, which have undergone shape transition, are also observed. (b) AFM image (0.6 μm by 0.6 μm; z range, 0.3 μm) of one elongated Cu_2O island.

We observed the formation and growth of elongated Cu_2O islands on Cu(100) surfaces through oxidizing the Cu(100) films inside the UHV-TEM in a very narrow temperature regime, near 600°C. After the introduction of oxygen gas into the column, the oxide islands were observed to nucleate rapidly, followed by growth. Figure 4.4 shows the morphology of Cu_2O islands formed on Cu(100) surface under 8×10^{-4} torr of oxygen partial pressure at 600°C. The islands are initially compact, and become progressively elongated as they grow larger. These elongated islands have varying lengths, but similar widths. The islands grow epitaxially with the underlying Cu surface, as revealed by selected area electron diffraction patterns, i.e., (100)Cu//(100)Cu_2O and [001]Cu//[001]Cu_2O as shown in the inset in Figure 4.4 (a). The elongation directions of the islands are always along the two orientation pairs of the four

crystallographic orientations, i.e., <011> and $<0\bar{1}\,\bar{1}>$ or $<01\,\bar{1}>$ and $<0\bar{1}\,1>$, and roughly equally distributed. We have observed elongated islands with aspect ratios as large as *40:1*. The island shapes were not observed to depend on oxygen pressure. Instead, the Cu_2O island density is closely related to the oxygen pressure. The island size is mainly determined by the oxidation time at this temperature. Resutls from atomic force microscopy (AFM) studies, as shown in Figure 4.4 (b), indicate that the islands have a flat top, and the contact angle, θ, between their edge facets and the substrate varied from *20°* to *35°* at the different growth stages. The height of the islands above the Cu film surface is approximately 15nm and remained almost constant for most of the islands during the continuous growth, as determined by examining the height of the islands with different cross-sectional areas. The total thickness of the islands was estimated to be around 20 nm by considering the conversion of the displaced copper atoms that had occupied the region of the Cu_2O island based on the island surface profile from the AFM observation.

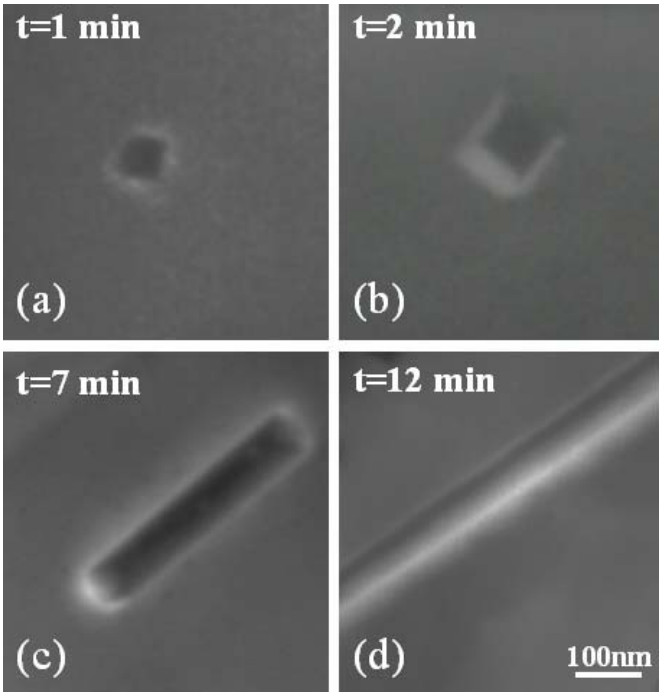

Figure 4.5 *In situ* TEM images of the four growth stages of a Cu_2O island as a function of oxidation time at constant oxygen partial pressure of 1×10^{-4} and temperature of 600°C. The initially formed square shaped island is shown in (a). The island remains a square when increasing in size (b). A shape transition to rectangular islands has occurred, where the aspect ratio increases with continued oxidation (c), and (d).

In order to visualize the growth of one island for a long time without interference due to coalescence with a neighboring island, we continuously oxidized the Cu(100) films at a low oxygen partial pressure of 1×10^{-4} torr. The volume evolution of the islands is recorded *in situ*, and a sequence of images focusing on the growth of a single island is shown in Figure 4.5. The initially formed island is square shaped as shown in Figure 4.5(a), and continues to grow uniformly in size (Figure 4.5 (b)). When a critical size, (~110nm), is reached, the island shows a fascinating shape transition to a quasi one-dimensional nanorod with the continued oxidation (Figure 4.5 (c), (d)). The contrast around the island is related to the strain in the island and the film. This was confirmed by AFM which indicates no dip around the island for the initial growth stages (Figure 4.5 (a-c)), and a very small dip ~5nm for the larger island (Figure 4.5 (d)).

4.2.2 Discussion

We compared our results with the theoretical model given by Tersoff and Tromp [59], who derived an analytical expression for the energy per unit volume (E/V) of a strained epitaxial island.

$$\frac{E}{V} = 2\Gamma\left(\frac{1}{s}+\frac{1}{t}\right)+\frac{1}{h}\left(r_i + r_t - r_s\right) - 2ch\left[\frac{1}{s}\ln\left(\frac{se^{3/2}}{h\cot\theta}\right)+\frac{1}{t}\ln\left(\frac{te^{3/2}}{h\cot\theta}\right)\right] \tag{4.1}$$

where s, t, and h are the width, length, and height of the island, respectively; θ being the contact angle. These parameters are shown in Figure 4.6. Γ contains the surface and interface energies and contact angle, $\Gamma=\gamma_e csc\theta-(\gamma_t + \gamma_s - \gamma_i)cot\theta$ (units J/m^2); γ_t, γ_s, and γ_e are the surface energies (per unit area) of the island's top, the substrate, and the island's edge facet, respectively; γ_i is the island-substrate interface energy. It should be noted that the interface in this case is a dynamically growing metal/oxide. The first two terms in Eq.(4.1) give the change in surface and interface energies when an island forms on the surface. The third term describes the stress in the island due to the substrate-island lattice mismatch. This stress causes the island to exert a force on the substrate, which elastically distorts the substrate. This lowers the energy of the island. Therefore, the energy of the island is relaxed by the cost of some strain in the substrate, and this

relaxation energy is related to c, $c = \sigma_b^2 (1-\nu)/2\pi G$, where ν and G are the Poisson ratio and shear modulus of the substrate, and σ_b is the island bulk stress.

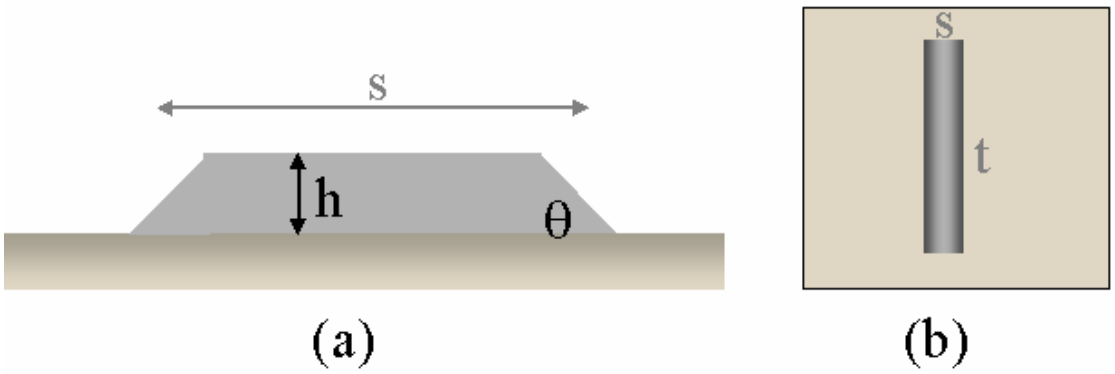

Figure 4.6 Schematics of the nanorod shape, showing the cross section (a), and planar section (b), and illustrating definition of width s, length t, height h, and contact angle θ.

In Equation (4.1), $2\Gamma\left(\frac{1}{s}+\frac{1}{t}\right)+\frac{1}{h}\left(r_i + r_t - r_s\right)$ is related to surface and interface energy, for an island with constant height, this term will decrease with larger *s* and *t*, i.e., large interfacial area. $-2ch\left[\frac{1}{s}\ln\left(\frac{se^{3/2}}{h\cot\theta}\right)+\frac{1}{t}\ln\left(\frac{te^{3/2}}{h\cot\theta}\right)\right]$ is related to the strain relaxation of the island, and this term will decrease with small *s* and *t*, i.e., small interfacial area. Therefore, it is clear from Equation (4.1) that for a given volume of an island with shape as shown in Figure 4.6, the surface energy dependent term prefers to have a large interfacial area island for stability, i.e., minimal surface area due to large interface area (flat island), while the strain relaxation energy term prefers to have islands with a smaller interfacial area (less strain) for more stability. So the optimal balance between surface energies and strain is obtained through the minimization of the total energy expression for an island of constant height, *h*, with respect to both *s* and *t*. This gives a square island with $s=t=\alpha_0$, where the optimal size α_0 is given by

$$\alpha_0 = e\phi h \exp(\Gamma / ch) \qquad (4.2)$$

where $\Phi=e^{-3/2}\cot\theta$, e is the usual mathematical constant. The island remains a square before increasing its size up to $s=t=e\alpha_0$. Due to continued oxygen exposure, the island grows beyond this critical size ($e\alpha_0$), the square shape becomes unstable and a transition to rectangular shape takes place. As the island grows further, the aspect ratio, t/s, increases, i.e., reducing its width back to the optimal size, α_0, while rapidly increasing its length. Equation (4.2) implies an experimental observation of the critical size, at which the shape transition occurs, and which determines the relative importance of the surface energy and the island stress. If the surface energy, Γ, dominates, α_0 becomes very large to reduce the edge-to-area ratio. But if the island stress dominates, then the minimum energy is obtained with smaller islands.

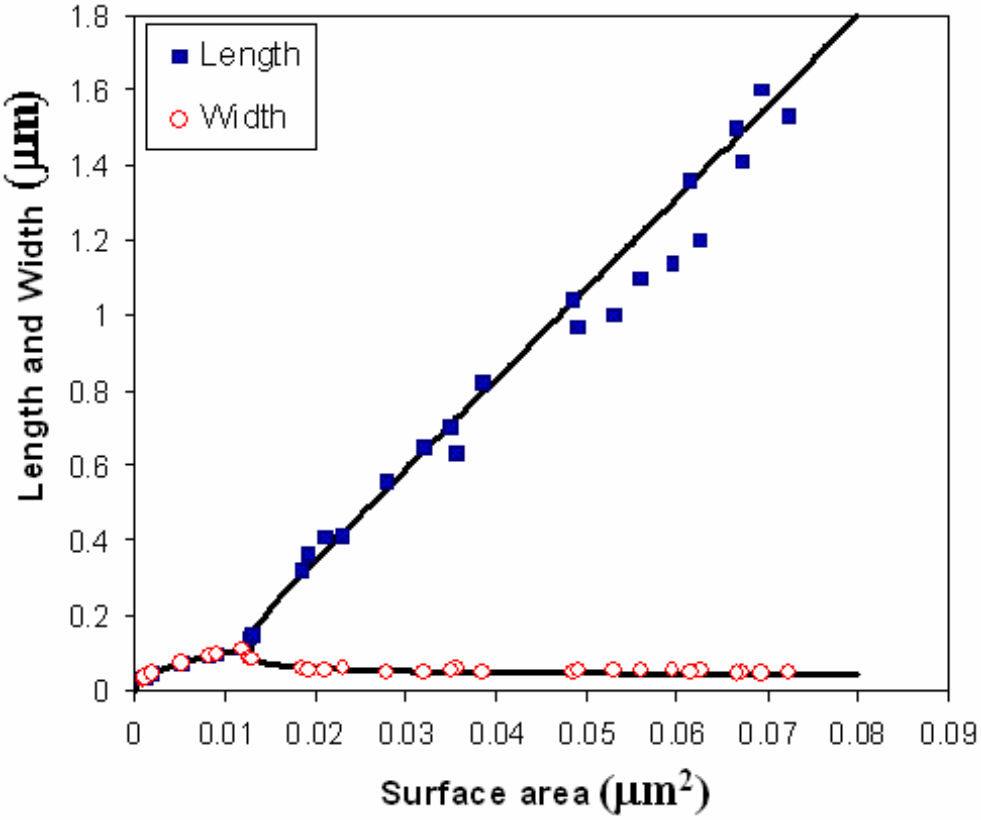

Figure 4.7 Dependence of both island length t (squares) and width s (circles) on the island surface area. The solid lines represent a theoretical fit based on Equation (4.1). The initially square shaped island undergoes a shape transition at the critical size $s=t=e\alpha_0$=114nm. There is a reduction of the width to its optimal width, α_0.

Therefore, in the evaluation of "c", we used standard values of G_{Cu} (40GPa) and σ_b for Cu_2O from the shear modulus (G=10GPa) and Poisson ratio (ν=0.455) of the Cu_2O [66]. The contact angle, $\theta = 30°$, and height, h=20nm, were measured by the AFM. By fitting with the critical size, $e\alpha_0$=114nm, we can estimate Γ from Eqn (4.2). Gamma (Γ) depends on the overall surface energies and interfacial energy, which were not readily available in the literature. These values can be substituted into Equation (4.1) to determine the energy per unit volume as a function of width s and length t.

A comparison of Tersoff and Tromp's model with our data shows good agreement for the size evolution of the island. Figure 4.7 shows the evolution of width s and length t versus the island area obtained from Equation (4.1), where the critical size (110nm) for the shape transition of the island was used as a fit parameter. It is seen that the island grows as square shape up to the critical size of 110nm, beyond which there is a transition to a rectangular shape. With its continued elongation, there is a reduction in the island width.

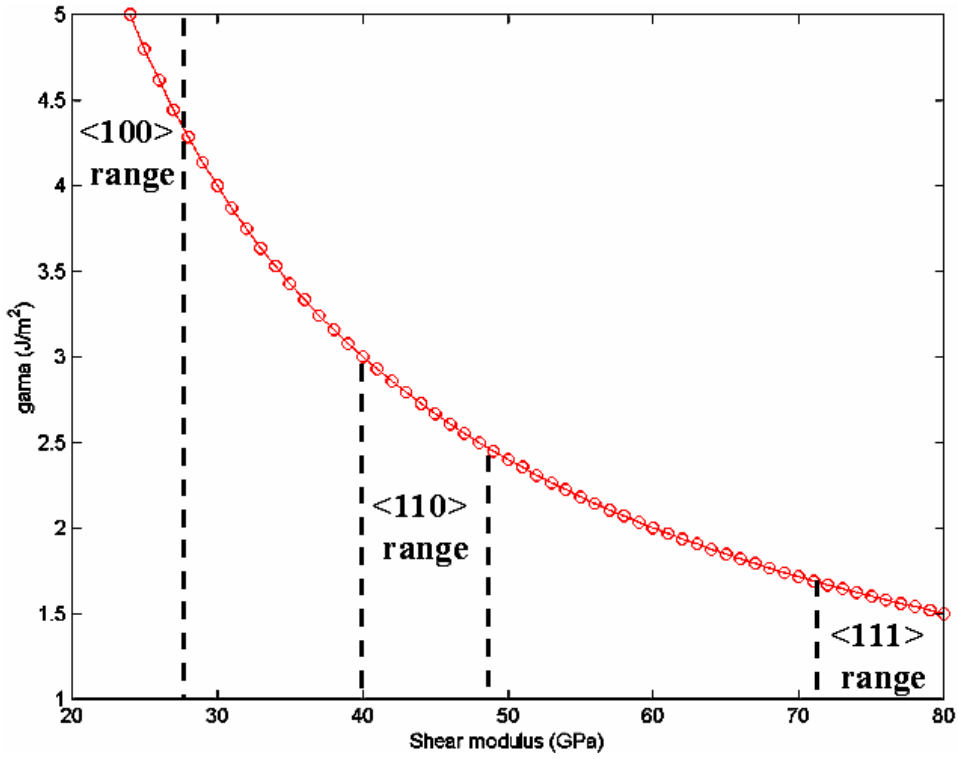

Figure 4.8 The dependence of the overall surface and interface energies (Γ) of the oxide island on the shear modulus of the substrate.

Because of the cubic anisotropy of the Cu substrate, the oxide islands are all randomly elongated in one of the two equivalent {011} directions, as shown in Figure 4.4 (a). Cu exhibits strong elastic anisotropy, the shear modulus along the <100>, <110>, and <111> directions is G_{100}~24.5GPa, G_{110}~48GPa, and G_{111}~71GPa, respectively [84]. Since the critical size of the shape transition of the island was used as the fit parameter to estimate the overall surface and interface energy, (Γ), the small change of the shear stress from 40GPa as used in the calculation has some effect on the overall surface and interface energy ($\Gamma=\gamma_e csc\theta -(\gamma_t + \gamma_s - \gamma_i)cot\theta$), but does not change the shape of Figure 4.7. Figure 4.8 shows the dependence of the Γ on the shear modulus. The shear modulus for the <110> direction results in the overall surface and interface energies (Γ) of 2.5-3J/m^2. The shear modulus for the <100>, or <111> direction results in a Γ too large or too small for epitaxial growth. The dependence of the overall surface and interface energy, (Γ), on the shear modulus may explain why the <110> direction is the preferred elongated direction. From this dependence we also know that the interface energy could be estimated from the critical size of the shape transition of the island in the epitaxial growth system if the surface energies of the oxide islands are known.

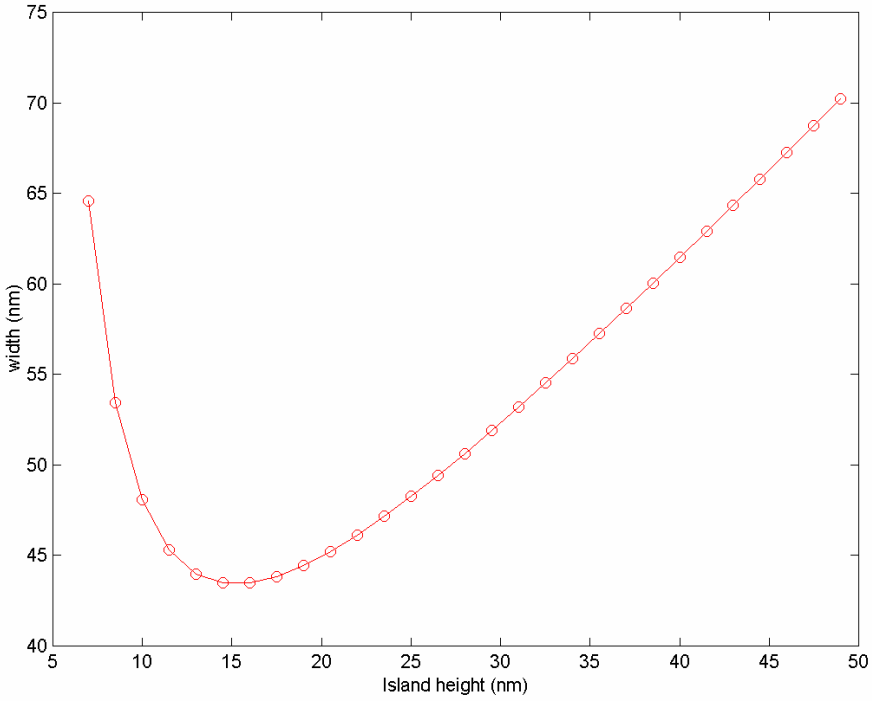

Figure 4.9 The change of the island width as a function of the island thickness

The observed constant island height is in agreement with the assumption used in Eq. (4.2). The minimum-energy island width is $s = \alpha_0 = e\phi h \exp(\Gamma / ch)$. However, Tersoff and Tromp noted that h may vary slowly compared with width s and length t, and it will inevitably increase as the island grows, since this lowers the island energy [77]. As indicated in Eq. (4.2) for the island width with minimum energy, this width decreases, relative to the height, with increasing h, until for $h \geq 2\Gamma/c$ ($s=\alpha_0=h\cot\theta$), the island becomes triangular in cross section. Figure 4.9 shows the change of the island width as the island increases its thickness. We, indeed, observed islands with triangular cross section as shown in Figure 4.10, and the AFM investigations indicated that the heights of most of the islands with triangular cross section are larger than 40nm.

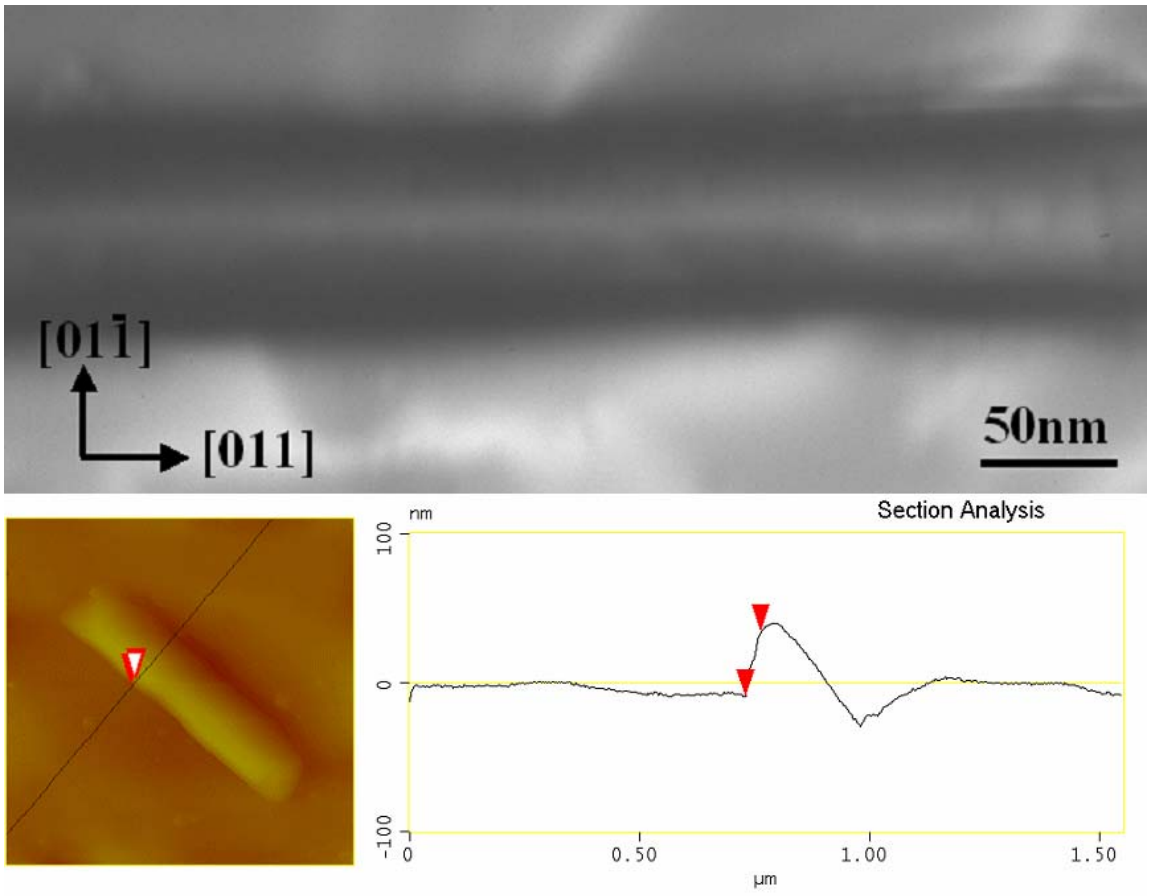

Figure 4.10 An elongated Cu_2O island that is triangular in cross section, an AFM image of an elongated island, the surface profile indicates that the island is triangular in cross section, and the island height is ~44nm.

The comparison of the island volume growth as function of time also provides significant insights into the oxidation kinetics. We assume that the dominant mechanism for the growth of three dimensional Cu_2O islands is surface diffusion of oxygen to the perimeter of the island [85]:

$$\frac{dN}{dt} = AK_S J_S \tag{4.3}$$

where *N(t)* is the number of oxygen atoms in a Cu_2O island at time t, K_s is the sticking coefficient, J_S is the diffusive flux of oxygen, and *A* is the perimeter of an island. The island volume evolution undergoes three different stages. (I) Before shape transition the island has equal length and width. By solving the above differential equation (Equation 4.3), the island volume increases parabolically with respect to oxidation time before the shape transition

$$V^I(t) = \frac{\left(K_S J_S \Omega\right)^2}{4h}\left(t - t_0\right)^2 \tag{4.4}$$

where Ω is the equivalent atomic volume of oxygen in Cu_2O, and *h* is the island height. (II): As can be seen from Figure 4.7, the width of the island reduces somewhat from eα_0 to α_0 within a few minutes after the shape transition and then remains constant. Therefore, in stage (II) the island's width and length change simultaneously as a function of oxidation time. The island volume increase with respect to oxidation time can be expressed as follows

$$V^{II}(t) = 2K_S J_S \Omega \int \left[s(t) + t(t)\right] dt \tag{4.5}$$

where *s(t)* and *t(t)* are the island width and length. It should be noted that equation (4.5) is the general form of the volume dependence on time. To estimate the integrand, $2K_S J_S \Omega\left(s(t) + t(t)\right)$, as a function of time, we used the experimental value of *s(t)* and calculated the corresponding *t(t)* from Tersoff and Tromp's model, which is also similar to the experimental measurements as shown in Figure 4.7. The coefficient, K_sJ_s, in Equation (4.5) was determined from the fit of the experimental data prior to the shape transition to Equation (4.4). Therefore, the island volume at time t in stage II, which is the integral of the formula: $2K_S J_S \Omega\left(s(t) + t(t)\right)$, can be numerically estimated as the area under the curve generated from this formula from the shape transition time to time t. (III): The island retains its optimal size, α_0, of width and constant height, the length increases with time, we determine that the volume of the island increases exponentially:

$$V^{III}(t) = \frac{(\alpha_0 h)^2}{2K_S J_S \Omega}\left(e^{\frac{2K_S J_S \Omega}{\alpha_0 h}(t-t_0)} - \frac{2K_S J_S \Omega}{h} \right) \tag{4.6}$$

Figure 4.11 is the fit of of this surface diffusion model to experimental data of the oxide volume. Prior to shape transition, the island volume increases parabolically with oxidation time, as shown in Region I. After shape transition the island volume increases exponentially with the oxidation time as shown in Region III. Region II corresponds to the transition zone of the island from compact to elongated structure, and the island changes its volume evolution behavior from parabolic to exponential dependency on time during this transition zone. The good fit of the kinetic model to the volume evolution of the island indicates that the growth of the Cu_2O islands is initially dominated by the surface diffusion of oxygen.

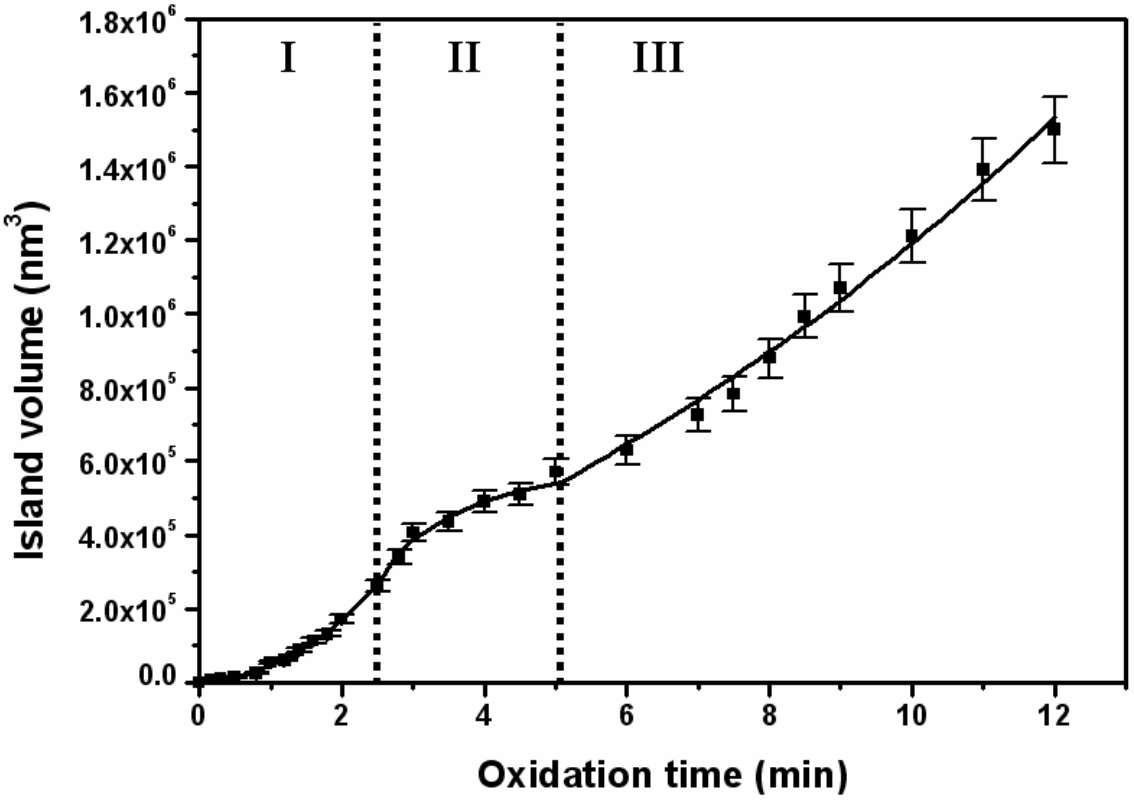

Figure 4.11 The volume of the Cu_2O island with respect to time when the copper film was oxidized at 1×10^{-4} torr oxygen and 600°C. The solid line corresponds to the theoretical fit to the oxygen surface diffusion model.

4.3 FORMATION OF CONTAINER Cu_2O PYRAMIDS AT 1000°C

Here the formation of a peculiar oxide structure, hollow pyramid, by nano-oxidation of Cu(100) films at 1000°C, is described. The evolution of the island size and shape was followed within the UHV-TEM and the topology was characterized by AFM. The containers have multiple terraces and ledges on their outer and inner side facets. A model based on elastic-plastic deformation is proposed to account for the formation of this structure.

The formation of oxide on metal surfaces could generate stresses in the oxide and substrate due to the volume mismatch between the oxide and metal. In the growth of bulk oxide, the relief of these stresses may occur by fracture in the oxide scale and/or in the underlying metals, or by separation of the oxide–metal interface. In nano-oxidation, the relaxation of the stresses may be very different from the bulk oxidation. For example, the oxide formation in nano-oxidation is similar to heteroepitaxial growth of lattice-mismatched systems in thin film growth and the models based on the surface/strain energies can be used to explain the formation of the different oxide nanostructures on surfaces [86, 87]. Therefore, not only the generation of stresses is of interest but stress-relaxation mechanisms in a growing oxide island during the oxidation process. The experiment for this structure is based on the transformation stress generated in the Cu_2O by the large lattice change by the oxidation of Cu (a=3.61Å) to Cu_2O (a=4.22Å) at ~1000°C. This temperature provides very fast oxidation kinetics, and therefore, fast stress buildup in the oxide.

4.3.1 Experimental observations

At 1000°C and 5×10^{-4} torr oxygen pressure, the oxidation of the Cu film begins rapidly so that oxide nuclei are seen on the surface within a few seconds after the introduction of oxygen gas into the column, then followed by the growth. Figure 4.12 (a) shows the general morphology of Cu_2O islands formed on Cu(100) film with thickness of 70nm after 1 min oxidation under the oxygen partial pressure of 5×10^{-4} torr. The initial oxide nuclei are visible with trapezoid shape located at the island center. With the continuous oxidation, the islands develop laterally to 4-fold symmetrical pyramids with terraces and ledges. The directions of the pyramid edges are normal to {011}.

In order to visualize the growth of one island for a long time without interference due to coalescence with a neighboring island, the Cu film was oxidized at a lower oxygen partial pressure of 3×10^{-4} torr. The morphology evolution of the islands was recorded *in situ*, and a sequence of images focusing on the growth of one island is shown in Figure 4.12 (b). After the introduction of oxygen gas into the column, the oxide pyramid island was observed to nucleate rapidly as followed by lateral growth. When the island width reached ~600nm, a ledge appeared quickly. The island continuously grew laterally and a second ledge appeared. The base layer of the island is laterally shifted with the periodic formation of the ledges. Eventually, a terraced pyramid formed with roughly equal width distribution of terraces (~230nm). This terrace and ledge evolution mode revealed that the pyramid growth occurred only along the base terrace of the island and the pyramid thickening was caused by the progressive formation of new ledges at the base terrace of the pyramid.

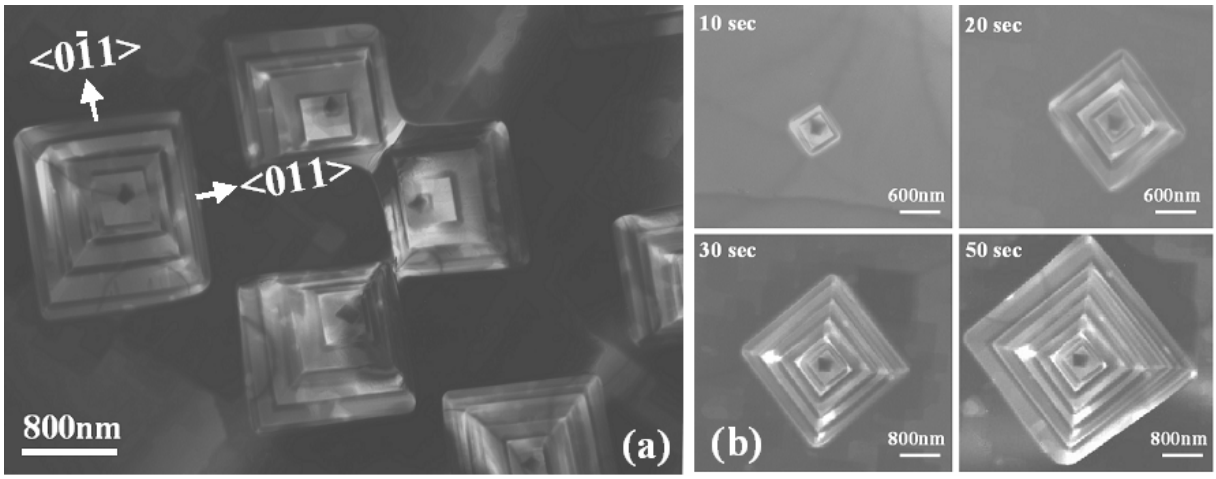

Figure 4.12 (a) The general morphology of Cu_2O islands formed by oxidation of Cu(100) at constant oxygen partial pressure of 5×10^{-4} and temperature of 1000°C. (b) *In situ* TEM images of the four growth stages of a Cu_2O island as a function of oxidation time at constant oxygen partial pressure of 3×10^{-4} and temperature of 1000°C.

Figure 4.13 shows a dark field TEM image from the Cu/Cu_2O interface area, where the Cu thickness fringes caused by the inclined interface, are visible. The inset (a) is the diffraction pattern from the interface area, where their epitaxial relationship is (100)Cu//(100)Cu_2O and [001]Cu//[001]Cu_2O. Inset (b) is an HREM image from the interface, where Moiré fringes,

caused by the overlap of Cu and Cu_2O lattices in the inclined interface area, are visible. Inset (c) is an HREM image of Cu away from the interface. The intact lattice structure of Cu indicates that the Cu film is defect free.

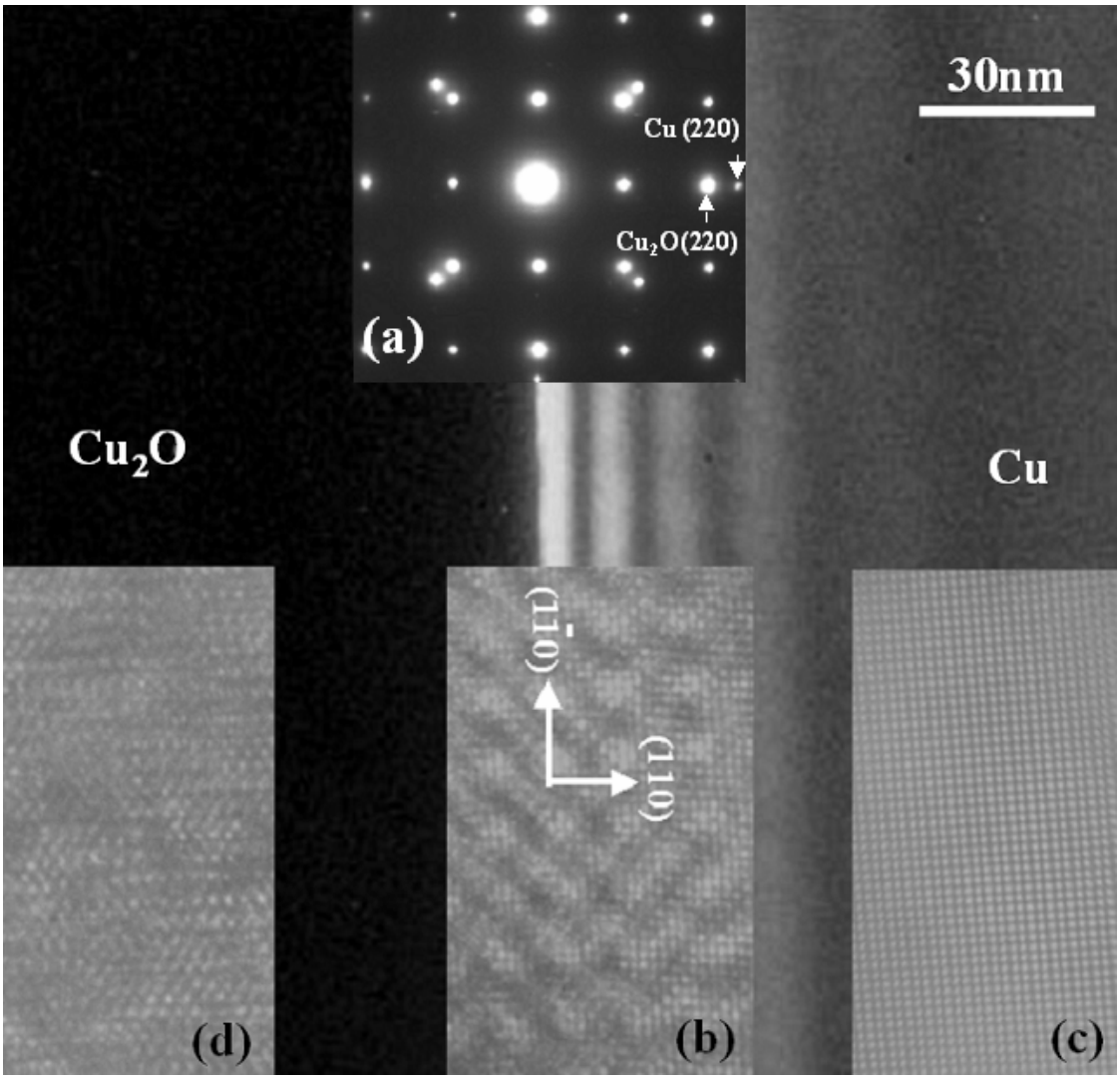

Figure 4.13 Dark field TEM micrograph from Cu reflection showing the equal thickness fringes in the interface area of Cu and Cu_2O; inset (a) Electron diffraction pattern from the interface area; Inset (b) HREM image from the interface area, where the Moire fringes are due to the superimposition of Cu_2O and Cu lattices; inset (c) Cu lattice image away from the interface; inset (d) Cu_2O lattice image away from the interface.

However, the HREM image of the oxide ~60nm away from the interface shows a large number of lattice distortions in the oxide, as shown in inset (d), which reveals the existence of

huge stresses in the Cu_2O. The occurrence of Moiré fringes only at the interface area also indicates that the oxide completely penetrates the Cu film as a wedge shaped interface. The thickness of Cu film is 70nm and the width of the projection of the interface on the Cu film plane is 50nm. This was determined by directly measuring the width of the zone having the thickness fringes. Therefore, the interface was determined to be $(111)Cu_2O//(111)Cu$ according to their epitaxial relationship. This interface structure remains during the oxidation, as determined by examining the interfaces of Cu_2O islands with different sizes.

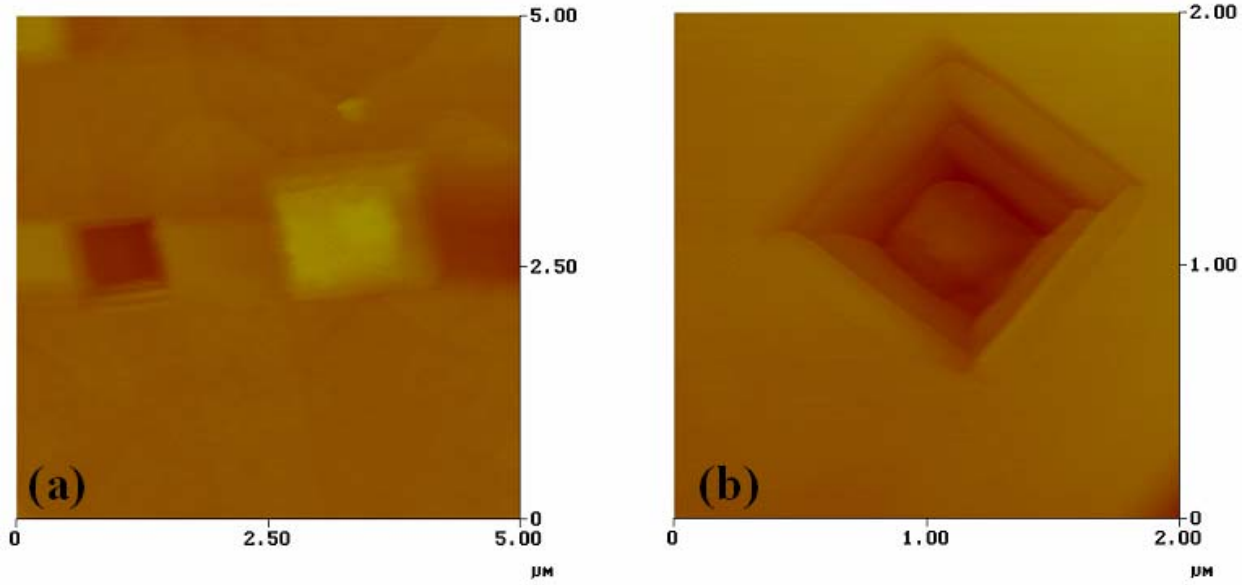

Figure 4.14 (a) AFM image (z range: 0.7μm) of two container pyramids, one is concave down, one convex up; (b) the higher magnification image (z range: 0.7μm) of a concave island.

4.3.2 Discussion

The formation of terraced pyramids on a surface is sometimes observed in thin film growth by the MBE technique, where threading screw dislocations on the substrate surface are responsible for the spiral growth of the terraced pyramids [88, 89]. The formation of oxide pit or pyramid structures by a screw dislocation mechanism was also observed on the surface of wustite scale in the oxidation of pure iron at 1200°C [90]. The formation of the screw dislocation at the oxide/gas interface produces a self-perpetuating ledge on the scale surface. As iron cations from the metal

reach the scale/gas interface by lattice diffusion, they migrate on the scale surface by surface diffusion to the ledge, which provides a favorable site for attachment and lattice extension. This growth model explained quite well the different pit/pyramid structures formed on the surface of the wustite scale [90].

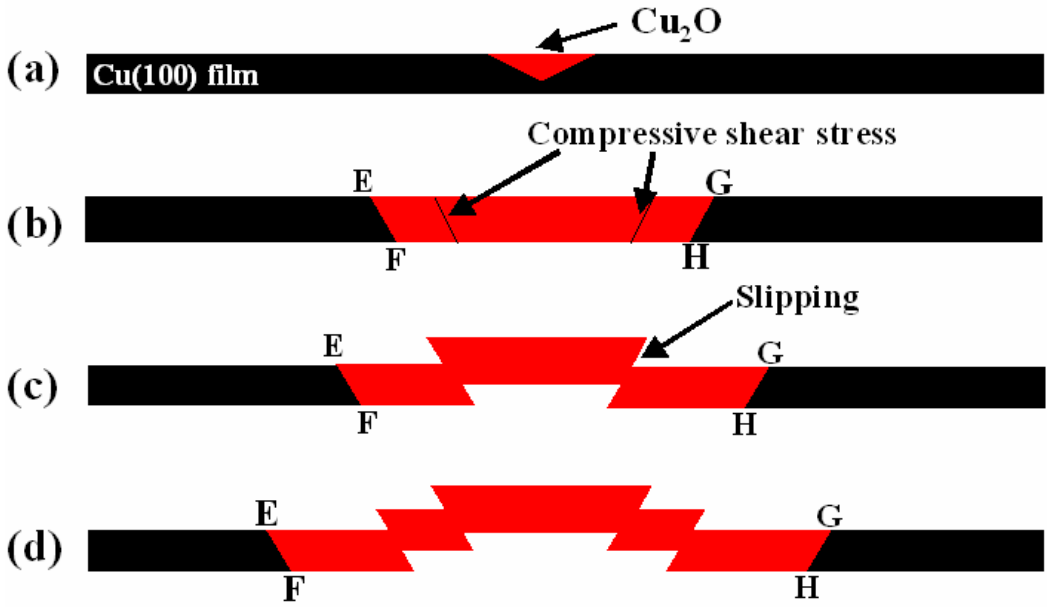

Figure 4.15 Schematics of the formation of the container pyramid

Due to the special sample geometry in the present investigation, the oxidation of the Cu thin film at ~1000°C resulted in very fast penetration of the oxide island through the whole film, which makes the growth mode of the islands different from the pyramid formation on a surface by thin film growth process, where the pyramid growth occurs on the surface. Also, this growth mode is different from the oxidation of bulk metals, where the continuous growth of the oxide is caused by lattice diffusion once the metal surface is covered by the oxide scale. For the oxidation of the thin Cu film at ~ 1000°C, the oxide island penetrates through the Cu film very quickly. Subsequently, the continuous oxidation will result in the lateral growth of the oxide island along the metal/oxide interface, EF and GH, as indicated Figure 4.15. The fast growth of the oxide along the EF and GH, i.e., the metal/oxide interface, generates a large compressive stress (transformation stress) buildup in the growing oxide due to the large lattice change from Cu to Cu_2O, which may play an important role in the formation of this hollow pyramid structure. Based on our *in situ* observations, the formation of this structure may be described as follows

(Figure 4.15). The first step is the nucleation of oxide islands on the Cu surface (Figure 4.15 (a)), then the oxide islands grow into the film and eventually penetrate through the film (Figure 4.15 (b)). The oxygen is then also available to the island bottom, and the island grows laterally along the inclined metal-oxide interfaces, as indicated by EF and GH in Figure 4.15. Since the island growth on the bottom surface of the copper film occurs at a later stage than the initial nucleation site (upper surface), therefore, the growth front (as indicated by E and G) of the island on the upper surface, is in front of that (as indicated by F and H) of the bottom surface as shown in Figure 4.15. The continuous formation of new Cu_2O along the inclined (111) Cu/Cu_2O interface (EF and GH) will exert a large shear stress on (111)Cu_2O (Figure 4.15 (b)). This shear stress becomes ever larger with the continuous growth of the islands, and finally causes the slip in the oxide by plastic deformation, in the normal direction to Cu(001) film, to release the stress (Figure 4.15 (c)). As a result, the central part of the Cu_2O island moves upward and results in hollow space, terrace/ledges on and inside the island. Multiple stress accumulation and relaxation gives rise to multiple formation of the terraces and ledges (Figure 4.15 (d)). The height of the ledges is determined by the extent of the relaxation of the total stress, and the terrace width is determined by the required strain energy for the slip. The {110} edge directions and the (111) shear stress provide <112> direction as the slip direction, as shown in Figure 4.16.

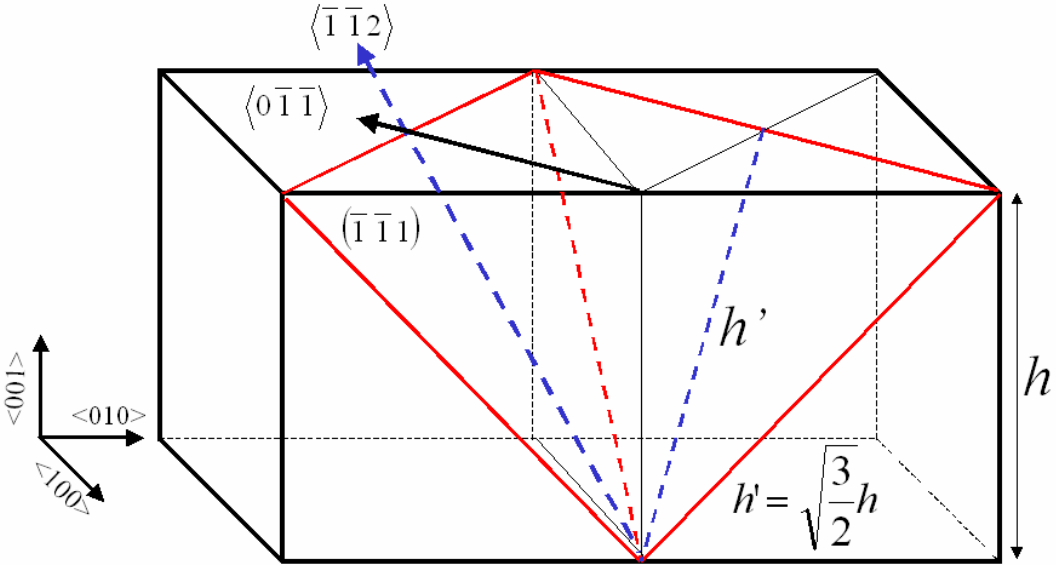

Figure 4.16 A section of Cu_2O structure, the slip direction is determined to be <112> from the relationship between the (111)Cu_2O shear stress and <110> edge directions of the pyramid.

We first calculated the amount of strain relaxation by this mechanism. Figure 4.17 is the schematic illustration showing the slip process and relationship between the ledge height and terrace width based on the island geometry (Figure 4.16). By the slip process, the strained ABCD is squeezed out from the oxide to form A′B′C′D′, then releasing the strain. During this process, the length of the strained AB is increased to A′B′, and the length of CD is increased to C′D′. Therefore, $(A'B'-AB)/AB$ corresponds to the relaxed strain, similarly, $(C'D'-CD)/CD$ is the relaxed strain. The length of A'B' is ~560nm, measured from the TEM negative films, and the ledge height is ~55nm, obtained from AFM measurements. Therefore, the change of AB to A′B′ is accompanied by ~14% strain relaxation. Similarly, the elevation of CD to C′D′ is also accompanied by ~14% strain relaxation. The formation of Cu_2O along the Cu_2O/Cu interface, i.e., EF and GH, results in the compressive strain, $\varepsilon = \frac{a_{Cu_2O} - a_{Cu}}{a_{Cu}} \approx 16\%$, which is very close to the strain relaxation by the elevation of AB to A′B′, and CD to C′D′.

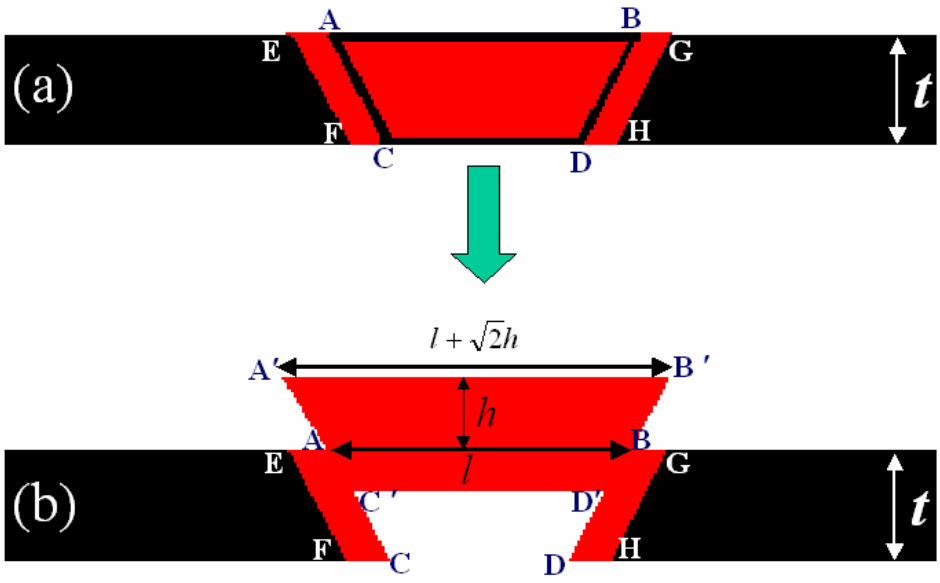

Figure 4.17 The slip process and the relationship between ledge height (h) and terrace width (*l*).

The stored strain energy (*SE*) caused by the formation of Cu_2O from Cu can be calculated as (Appendix 3)

$$SE = \frac{1}{3} \times t \times \left(\frac{E}{1-\nu} \varepsilon^2 \right) \times \left(3l^2 - 3\sqrt{2}tl + 2t^2 \right), \tag{4.7}$$

where E is Young's modulus of Cu_2O, ε is the normal strain in the oxide, and the size parameters, l and t, are defined in Figure 4.17. This stored strain energy increases as the square of the island size. To evaluate the stored strain energy, we used standard values of **E** (30GPa) and the Poisson ratio (ν=0.455) for Cu_2O [76]. The strain in the oxide can be obtained by considering the lattice change from Cu to Cu_2O, $\varepsilon = \frac{a_{Cu_2O} - a_{Cu}}{a_{Cu}}$, the different thermal expansion coefficients, 1.9×10^{-6} °C^{-1} (Cu_2O) and 17×10^{-6} °C^{-1} (Cu), were included.

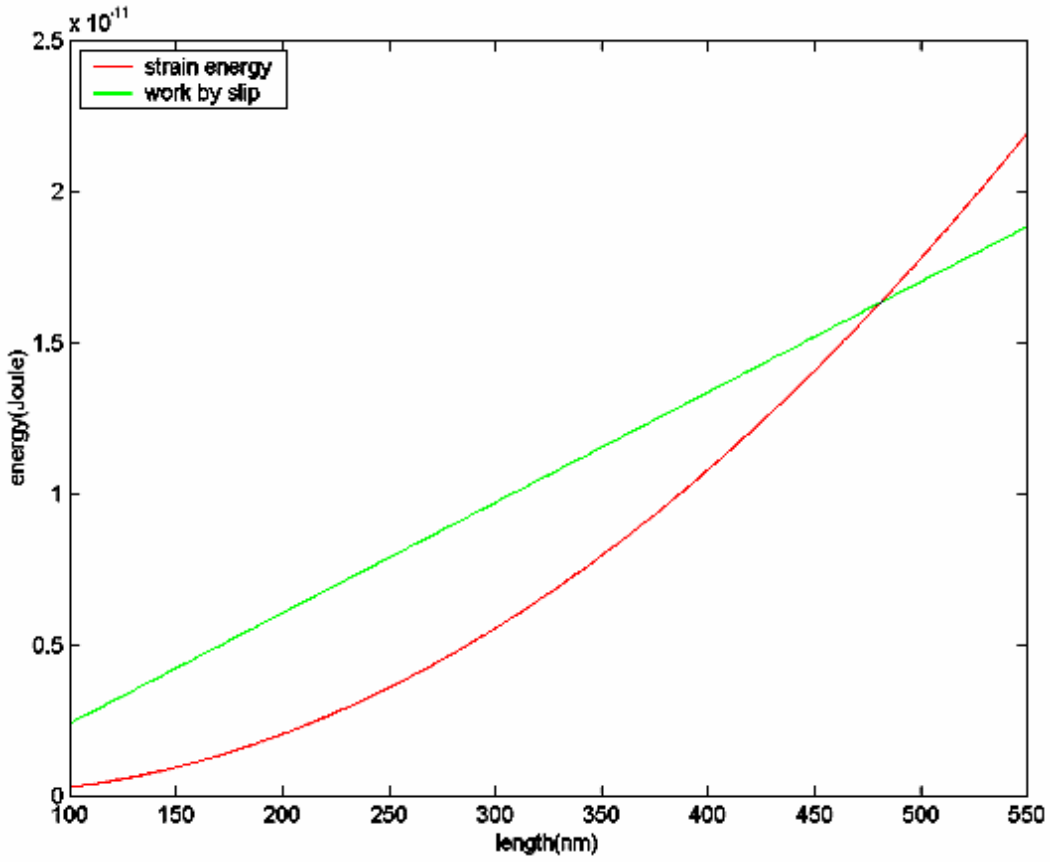

Figure 4.18 The plot of the stored strain energy and the work done by the slip, the intersection point corresponds to the size l as defined in Figure 4.17.

The hollowing process in the pyramid creates new inner and outer surfaces, as shown in Figure 4.17, which creates extra surface energies. Therefore, part of the stored strain energy is

consumed by the formation of the new surfaces. We can make a rough comparison between the stored strain energy and the extra surface energy. For the first terrace (A′B′=560nm), the new surface area created during the hollowing process is

$$S = \sqrt{6}h \times [2(2l + \sqrt{2}h) - 2\sqrt{2}t] \tag{4.8}$$

The accurate surface energy of Cu_2O is unknown, but the surface energy of oxides is usually in the range of 1~2 J/m^2, therefore, the total extra surface energy of the island during the hollowing process is ~5×10^{-13} J. The stored strain energy obtained from Eq. (4.7) is ~ 1.7×10^{-11} J for the first terrace. Therefore, compared with the stored strain energy, the extra surface energy due to the formation of the new surface area during the hollowing process is small and can be neglected.

From this analysis, we can know that the stored strain energy provides the required energy for the deformation process. The work done by the slip process depends on the shear stress on the slip plane and the surface area undergoing the slip, and this work done by the slip can be calculated as (Appendix 3),

$$W = 3\tau \times l \times [t^2 - (t-h)^2] - \sqrt{2} \times \tau \times [t^3 - (t-h)^3], \tag{4.9}$$

where τ is the shear stress required for the slip in the growing oxide islands, and the size parameters are same as that in Figure 4.17. The shear stress τ for the slip process is unkown, and we used the experimental terrace size to determine the shear stress for the slip. Provided that all the stored strain energy (*SE*) is released by the slip process, i.e., *SE*=*W*, then the shear stress τ can be estimated. Figure 4.18 shows the plots of the stored strain energy and the work done by the slip process for the formation of the first terrace, where the intersection point corresponds to the island size for the slip. From the width (~560nm) of the first terrace and the ledge height (~55nm), the shear stress was estimated to be 2.5 GPa for the slip. This shear stress is very large and close to the theoretical strength ($\tau = \frac{G}{2\pi}\frac{b}{a} \approx 3.4$ GPa) of the Cu_2O structure. In bulk materials, especially in metals, the shear stresses are often several orders of magnitude less than the theoretical strength due to the existence of the localized structural defects. In ceramics, slip by dislocation motion is more difficult than in metals because ions of like charge have to be brought into close proximity of each other, i.e., larger barrier (Peierls stress) for dislocation motion. The main reason why nonmetallic crystals such as ceramics materials can not have a

high deformability and be utilized as structural materials is that the Peierls stress in these crystals is so high that the dislocations are inactive at stresses below the fracture stress [91]. Therefore, the shear stress needed to cause slip by the dislocation mechanism could be high in Cu_2O.

Table 4.1 Comparison of Cu_2O and MgO properties [76].

Parameter	**Cu_2O**	**MgO**
Oxygen sublattice	Bcc	Fcc
Lattice constant (Å)	4.22	4.21
Melting point (ºC)	1235	2826
Density (g/cm^3)	6.0	3.6
Young's modulus, E (GN/m^2)	30	209
Shear modulus, G (GN/m^2)	10	75
Poisson's ratio	0.455	0.36
Thermal expansion coeff. (10^{-6})	1.9	10
Surface energy ($ergs/cm^2$)	Unknown	1150

Experimental data regarding the deformation of Cu_2O are not readily available. The deformation mechanisms of some other oxides may provide some clues regarding the plasticity of the Cu_2O. Polycrystalline Al_2O_3 aggregate with grain size of 10μm shows plastic deformation under shear stress of ~0.01G=1.55GPa (G is the shear modulus of Al_2O_3) at a temperature of $0.8T_M$. Polycrystalline MgO aggregate with grain size of 1μm shows plastic deformation under a shear stress of ~0.008G=1GPa (G is the shear modulus of MgO) at the temperature of $0.8T_M$ [92]. In the present experiment, the temperature for the formation of the Cu_2O is ~$0.8T_M$ (T_M=1245°C for Cu_2O), and the determined shear stress for the slip is 0.25G (G= 10GPa for Cu_2O). This higher normalized shear stress ($\frac{\tau}{G}$=0.25) determined by the slip mechanism in the present case could be possible due to the small size (nanometer scale) and single crystalline structure of the islands which usually have a higher deformation stress than the bulk ones. In this analysis, we only considered the dissipation of the strain energy by the slip process. However, some other factors, such as heat loss, atom diffusion, etc., may release part of the stored strain

energy during the hollowing processing. Putting together these different processes to release the stored strain energy will give rise to a smaller shear stress for the slip.

As discussed above, the formation of this hollow structure is closely related to the strain relaxation in the oxide island. One question about this mechanism is why the strain is released by the oxide island, rather than by the Cu film. Compared to other oxides, Cu_2O is an atypically soft material with low mechanical modulus (see Table 4.1) and its lattice is more flexible than other oxides. In addition, the low melting temperature of Cu_2O (T_m=1235°C) [93] indicates that the lattice cohesive energy is not as great as those of other oxides. The Young's modulus and shear modulus of copper is ~124 GPa and ~40 GPa, respectively. The temperature dependence of the shear modulus of Cu ($\frac{T_M}{G_0}\frac{dG}{dT}$) is –0.54 [92], and therefore, the shear modulus of Cu at 1000°C is ~38.7GPa. Hence, compared to Cu, the Cu_2O has smaller Young's modulus and shear modulus (E=30GPa and G=10GPa). On the other hand, the Cu film is very thin, (~70nm), and was annealed at ~1000°C before the oxidation. The dislocations in the Cu film can then easily move to the Cu surface and form surface steps, and, therefore, the Cu film could be dislocation free before the oxidation experiment at 1000°C. This makes it more difficult to release the strain by the Cu film than the Cu_2O. The present TEM observation indicates that the Cu film had a flat surface with some surface steps at 1000°C, and no dislocation was observed. Also, the oxidized Cu film has a much larger physical size (1.5mm × 1.5mm) than the oxide islands (nanometer scale). The much larger physical size, higher Young's and shear modulus of the Cu film compared to the Cu_2O, and the absence of pre-existing dislocations in the Cu film may explain why the strain is released by the Cu_2O island, not by the Cu film.

The permanent deformation of crystals in response to stress may be through deformation twinning, dislocation glide or diffusional processes. All of these processes may be interrelated and may occur at the same time. However, as a general trend, deformation twinning is often the only macroscopic deformation process observed in complex ceramic crystals at low homologous temperatures. In the present case, the Cu_2O island is formed at ~$0.8T_M$. Therefore, some other potential scenarios, such as strain assisted growth, diffusion, creep, and screw dislocation [90] leading to the formation of pyramids could also be possible.

The slip model proposed here seems to be the simplest explanation of the present experimental observation. However, there are still some important issues to clarify in the future.

The first is whether the observed morphology can be produced by a growth mechanism that does not require the repeated shearing off of a critically stressed volume. The second is whether dislocation activity in the Cu_2O should or could happen prior to complete decohesion due to the stresses reaching the theoretical shear strength of the materials involved. Therefore, despite the feasibility of the "slip" explanation, further *in situ* experiments with higher temporal and spatial resolution to reveal more details during the formation process of this peculiar structure are needed to distinguish, uniquely, the mechanism. These details may include whether there is dislocation formation and motion in the growing oxide islands because this is related to the strain relaxation mechanism in the oxide islands; whether there is a change of the Cu film thickness in the vicinity of the growing oxide islands, which may provide some clues regarding possibility of the formation of this structure by growth mechanism, not the slip mechanism; and whether there is an absence of any pre-existing dislocation in the Cu film near the oxide islands, which could change the strain relaxation by the Cu film rather than by the oxide islands.

Experimentally, we also found that the pyramid structure is closely related to the thickness of the oxidized films. Figure 4.19 shows different container pyramids obtained by oxidizing the Cu(100) film with the different thickness.

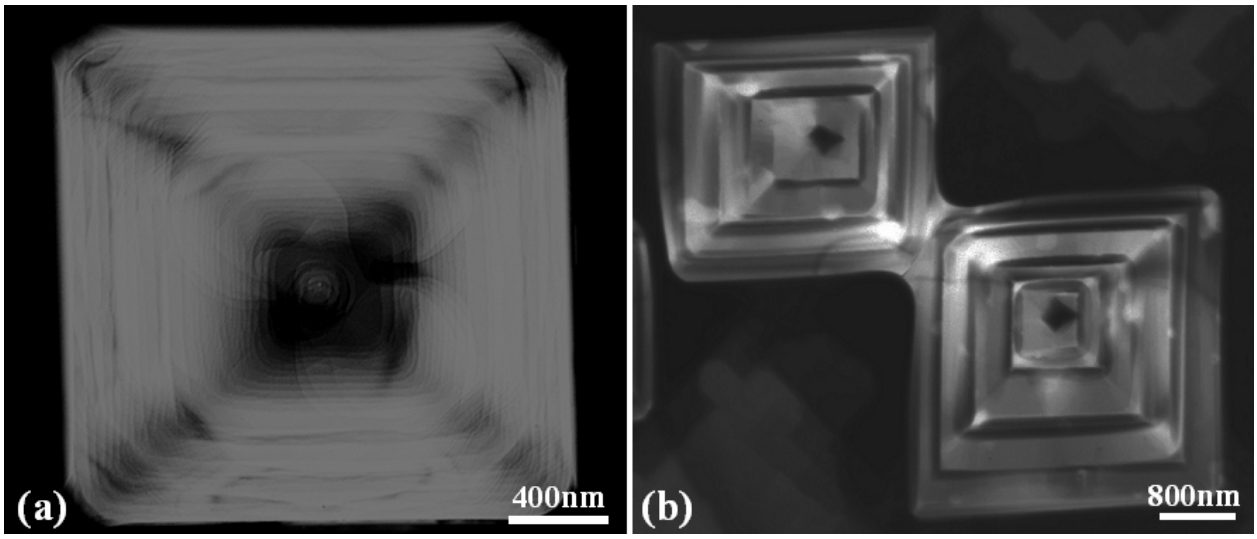

Figure 4.19 The container pyramids obtained by oxidizing the Cu films with different thickness (a) 50nm; (b) 90nm. The island lateral size for the first slip is ~390nm, the terrace width and ledge height is ~65nm and ~35nm respectively for 50nm thick Cu film; ~650nm, ~130nm and ~65nm for 90nm thick Cu film.

4.4 SHAPE CHANGE OF Cu_2O ISLANDS

The oxidation at 600°C results in the formation of the nanorod structure which is determined by energetics [86]. However, in most situations, crystal growth is governed by the formation of well-defined planes under kinetic growth conditions. The crystal shape is determined by those planes that have an extremely fast growth rate. For an expanding crystal solid, the planes with the lowest advancement rate determine the final shape [94, 95].

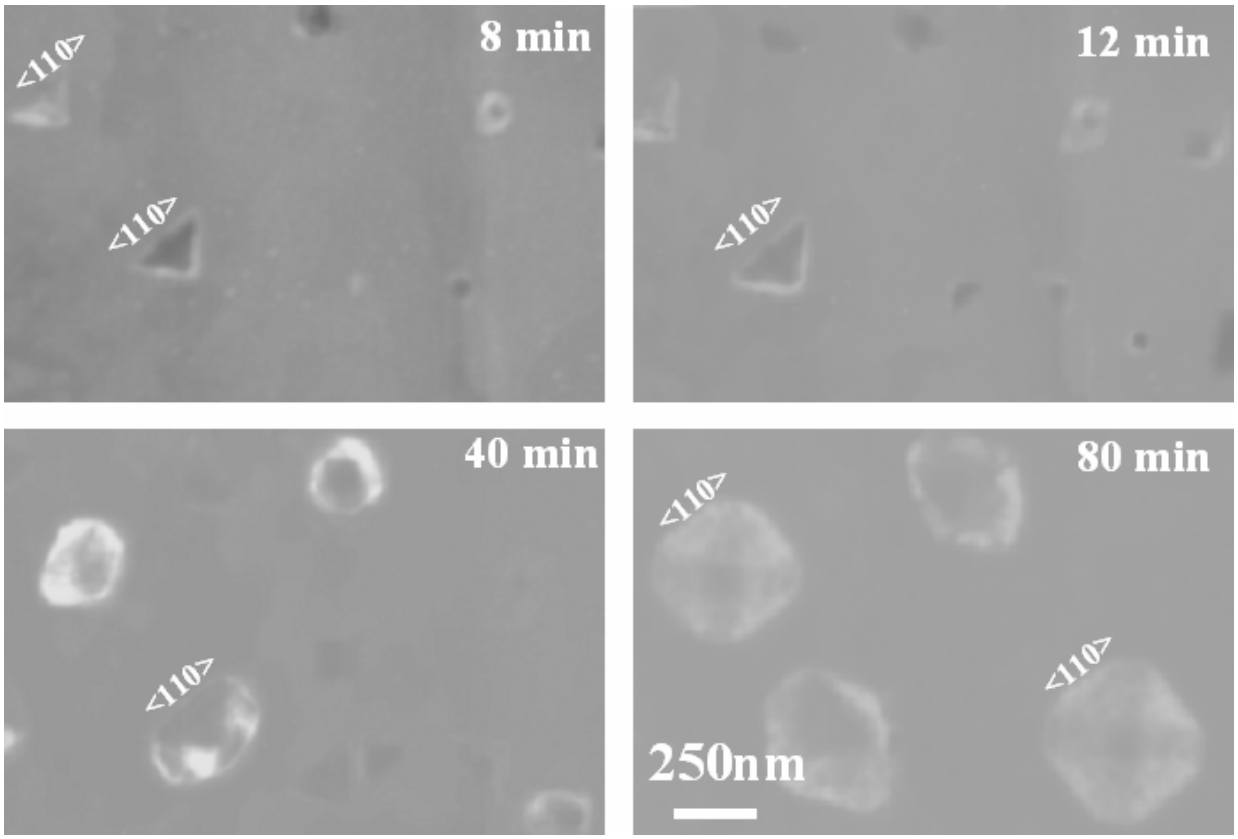

Figure 4.20 The shape evolution of Cu_2O islands from triangular to square pyramids at 450°C and oxygen pressure of 5×10^{-4} Torr.

Figure 4.20 shows our *in situ* observation of the growth of Cu_2O islands on Cu(100) at the oxygen pressure of 5×10^{-4} torr and temperature of 450°C. It shows the detailed morphological evolution of Cu_2O islands during the island growth. Firstly, we observed the formation of triangular Cu_2O islands. Following the island formation, the islands evolved further, undergoing a sequence of shape changes, and finally square or truncated square islands formed. It is noted

that one edge of the triangular shaped islands is along <110>; the other two edges are along the directions with high indices which can vary from island to island.

As we have discussed earlier, the large lattice mismatch will cause large strain energy in the island, and the islands tend to minimize the energy by minimizing the interfacial area. This was confirmed by the oxidation at temperatures as low as 350°C, where the oxide and the Cu film have a large lattice mismatch, and the formed oxide islands have a triangular shape which minimizes the interfacial area, and, therefore, minimizes the overall interfacial energy. Therefore, the islands minimize their total energy by keeping this triangular shape, and this shape is energetically favorable.

However, as the oxidation temperature increases to 450°C, the initial islands still had a triangular shape, indicative of large interfacial energy. With continuous oxidation, the oxide islands evolve to squared or truncated squared shape, where the island edges are along {110} directions. This shape change should be related to the enhanced oxidation kinetics at this temperature. Usually the facets with high index have a faster growth rate than that with low index, and the final facets of the crystal have low index. The continuous growth of the triangular shape islands causes the disappearance of the high index facets, leaving behind the low index facets {110}, as shown in Figure 4.20. Therefore, the final island morphology could be determined by the growth rates of different planes, i.e., kinetically controlled morphology. By considering the oxidation for long times, the oxide islands will evolve to the equilibrium shape, and it would be square-shaped along the close-packed directions such as {110}. Figure 4.21 is a schematic drawing of the formation of the square-shaped island caused by the growth kinetics of the island.

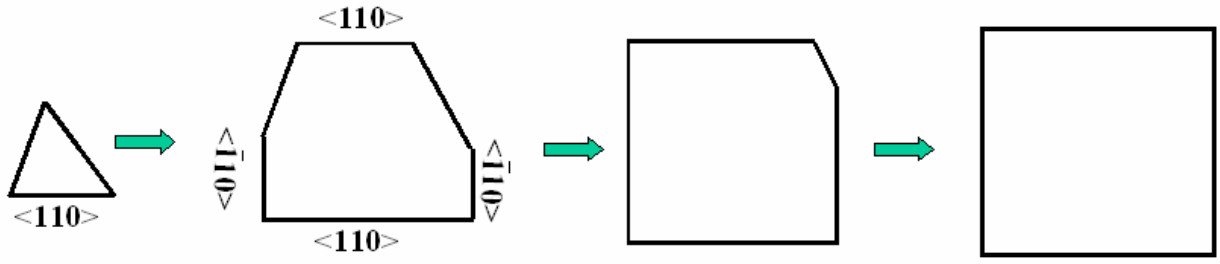

Figure 4.21 A schematic drawing showing the formation of a squared-shape island caused by the different growth rates of the different facets.

As the oxidation temperature increases to a higher point, such as 600°C, the lattice mismatch becomes smaller, and, therefore, the interfacial strain energy becomes smaller. Hence, the chosen interfaces could be along the low energy interfaces (such as the low index planes {110}), and the initial oxide islands have compact structures which minimize the total energy of the islands. This shape is very different from the triangular shaped islands formed at the low temperatures. With the further growth of the islands, the competition between surface/interface energy and strain energy causes the formation of nanorods.

With the further increase of the oxidation temperature, the lattice mismatch decreases further, and the interfacial strain energy decreases, as well. Therefore, the islands try to minimize their energy by being more compact and minimizing their surface energy. Figure 4.22 shows the *in situ* observation of the shape evolution of an island at the oxygen pressure of 5×10^{-4} and temperature of 750°C. Figure 4.23 is an AFM image of the island after 6 min oxidation, which shows the 3D geometry of the island at this temperature. The initially formed islands have a dome structure which has the smallest surface area. The islands minimize the surface area by this dome shape, thereby minimizing their surface energies. But with the continuous oxidation, some facets grow smaller until they no longer exist. Therefore, the final shape of the islands could be determined by the relative growth rates of the different crystal facets. This kinetic limitation to growth leads to the effect that rapidly growing crystal faces often grow out of existence, leaving only slowly growing faces behind. Crystal faces grow out of existence when their velocity component in a particular direction exceeds that of a neighboring crystal face growing in the same direction. Because low-index planes generally grow slower than high-index ones, the shape of crystals determined by kinetics can be the same or quite similar to those at equilibrium, but this need not be the case. Because the high-index facets have a faster growth rate, they grow out of existence with the increase in the island size. The final shape of the island is determined by the low-index facets which have slow growth rate, i.e., kinetically controlled morphology. By comparing with the oxidation at 450°C as shown in Figure 4.21, where it took ~80min for the island shape change from triangular to square, it is noted that the kinetics at 750°C was highly enhanced, where it only took ~16 min for the shape change from dome shape (energetically favorable shape) to square shape (kinetically favorable shape).

The *in situ* TEM and AFM investigation revealed that the side facets of triangular shaped islands have high index, while the normal directions of the edge facet of square shaped islands

formed at 450°C, as shown in Figure 4.21, are along <011> directions, and they have roughly equal growth rates along these four equivalent crystallographic orientations, which results in the four-fold symmetry of the island. Similarly, the normal directions of the edge facet of square shaped islands formed at 750°C (Figure 4.22), are also along the <011> directions, and they have equal growth rates along the four equivalent crystallographic orientations resulting in the four-fold symmetry of the island. The kinetic growth situation described above should be distinguished from the situation in which thermodynamics govern the island shape as the nanorods formed at 600°C.

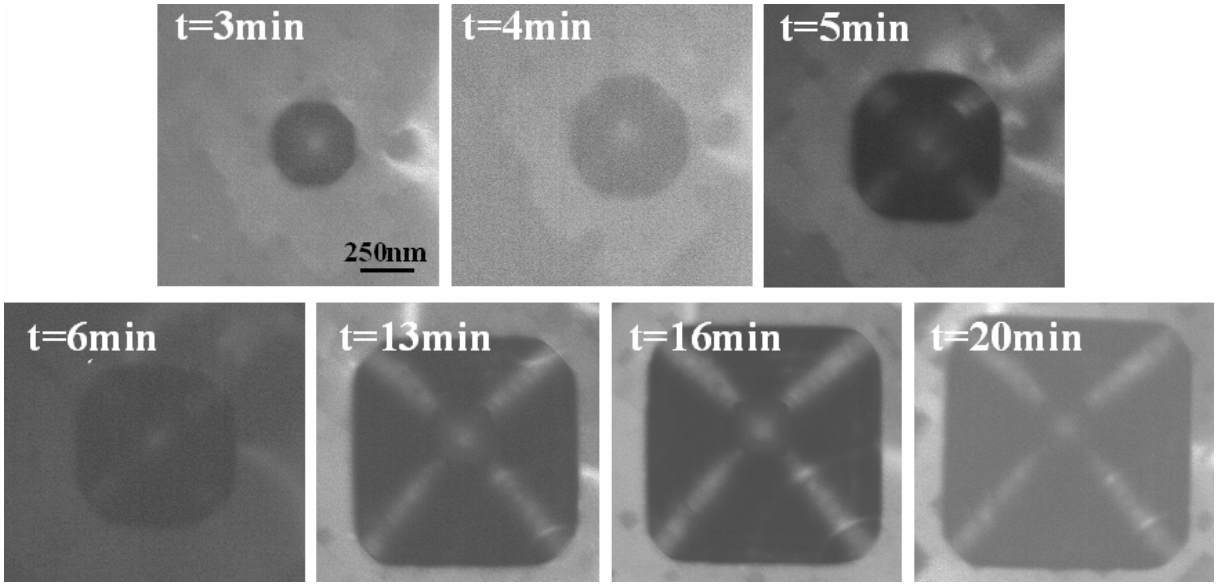

Figure 4.22 *In situ* TEM images of the different growth stages of a Cu_2O island as a function of oxidation time at constant oxygen partial pressure of 5×10^{-4} and temperature of 750°C.

Our observations regarding the morphology of oxide islands formed at different temperatures are summarized as follows. The initial oxide islands have a triangular shape in the oxidation temperature range of 350~550°C. With the continuous oxidation, the islands have a shape change from triangular to square shape in the temperature range of 400-550°C. The oxidation at ~600°C results in the formation of square shape islands in the very beginning, and the islands have shape transition from square shape to elongated structure with the continuous oxidation. The initial islands formed at ~750°C has a dome structure, and transforms to square pyramid with the continuous oxidation. The oxidation at 1000°C results in the fast penetration of the oxide island into the Cu film, and forme a hollow pyramid structure with continuous oxidation.

The morphology of the initial oxide islands is controlled by energetics, i.e., by minimizing the total energy of the islands, and by kinetics factors which could lead to different facet formation during island growth, where the final island shape is determined by the growth rate of the different planes.

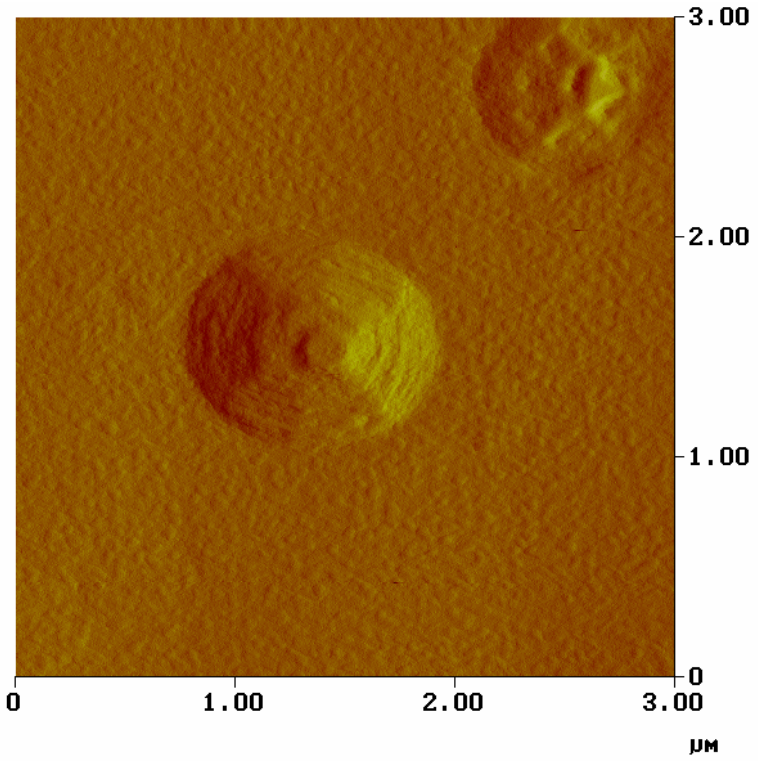

Figure 4.23 AFM image (z range: 950nm) of an island formed at 5×10^{-4} and temperature of 750°C.

4.5 CONCLUSIONS

We demonstrated that dramatically different morphologies of oxide nanostructures can be achieved by modifying the oxidation temperature. The oxygen pressure is noted to change the density of the oxide island and the oxidation rate only. We find that a critical factor to the island morphology is interfacial strain energy during oxidation. The oxidation temperature has a large effect on diffusion, interfacial strain, surface and interface energies, and mechanical properties,

which all play a significant role in the development of the oxide morphology to pyramids, nanorods, domes or container structures. A model based on the relaxation of elastic stress was used to explain the formation of the one dimensional Cu_2O structure. A model, based on plastic-slip to release the stored energy build-up due to volume change, was proposed to account for the formation of container oxide structures.

5.0 Cu(110) OXIDATION

Gwathmey and co-workers [52, 53, 96] have demonstrated that the oxidation phenomena observed on copper vary with crystal orientation. Investigations by Benard and co-workers [97, 98] showed that the rates of oxidation were different for different crystal orientations. In the present work, we present a systematic investigation of the kinetics of the initial oxidation on Cu(110) surface. Interestingly, The result of Gwathmey *et al.*, on the different passivation behavior of different Cu orientations can be explained by coalescence. We have examined the dependence of island density on oxidation time, saturation island density on oxidation temperature, and island growth as a function of oxidation time. The results presented here for the Cu(110) surface reveal the similarities and differences observed for Cu(100) and Cu(110), and demonstrate the generality of the oxygen surface diffusion model originally developed to describe the results observed on the Cu(100) surface [39]. With increasing temperature, the oxide islands show a faster thickening rate which could be due to the reduced interfacial strain energetics. Cu(110) surface shows thermal roughening at ~710°C, and the investigation of the oxidation on the roughened surface revealed that the oxide nucleation is enhanced by the increased surface roughness. The oxidation on faceted Cu(110) (T>800°C) shows dramatically different nano-oxide morphology from the flat surface, where the facets provide a template for the nucleation and growth of oxide nano-rods.

5.1 OXYGEN SURFACE DIFFUSION MODEL

Before presenting the results for oxidation of Cu(110) surfaces, we will briefly discuss the oxygen surface diffusion model for oxide nucleation and growth [39].

5.1.1 Nucleation

During the nucleation stage, oxygen impinges upon the substrate, diffuses across the surface, and may be lost to re-evaporation, formation of new nuclei, or incorporation into an existing Cu_2O island. Regardless of the details of the intermediate steps, the density of these stable nuclei is expected to increase with time, reach a saturation level, N_s, and then decrease as the discrete nuclei grow into larger islands and coalesce. Therefore, one consequence of oxygen surface diffusion being the mechanism for nucleation is that there is a saturation island density, $1/L_d^2$, where L_d^2 is the area of the "zone of oxygen capture" around each Cu_2O islands. An oxygen concentration gradient exists across this zone such that oxygen that lands within this zone shall diffuse to the Cu_2O islands; hence, the oxide islands act as oxygen sinks.

Yang, *et al*., assumed oxygen surface diffusion is the dominant transport mechanism for the nucleation of copper oxides. The probability of an oxide nucleation event is proportional to the fraction of the available surface area outside these "zones of oxygen capture" and the oxide nucleus density can be determined to be [39]

$$N = \frac{1}{L_d^2}\left(1 - e^{-kL_d^2 t}\right) \tag{5.1}$$

where L_d^2 is the area of the zone of oxygen capture, $1/L_d^2$ is the saturation island density, L_d is much larger than the diameter of the oxide island, k is the initial nucleation rate, which depends on the probability for Cu and O to form Cu_2O at the oxidation temperature, and t is the oxidation time.

Because of higher mobility of oxygen at higher temperatures, the attachment to existing islands is more favorable than the nucleation of new nuclei, it is reasonable to expect small islands with high density are formed at low temperatures, whereas for high temperatures less island density but larger average island size is expected. Since processes contributed to nucleation, such as diffusion, have an Arrhenius dependence on temperature, then it is reasonable to expect that the saturation island density dependence on temperature could follow an Arrhenius relationship,

$$N_s \sim e^{-E_a/kT} \tag{5.2}$$

where k is Boltzmann's constant, and T is the oxidation temperature. This activation energy, E_a, of the nucleation depends on the energies of nucleation, adsorption and/or desorption of oxygen [32], and not necessarily only on the oxygen surface diffusion energy. By measuring the island density at different temperatures, then the activation energy, E_a, for this surface-limited nucleation process, can be determined.

5.1.2 Growth

Orr, [85] followed by Holloway and Hudson [99], has developed an oxidation model based on the assumption that oxygen surface diffusion should play a major role in the initial growth of the metal oxide. They assumed that the oxide islands grew on the metal surface, i.e., 2-dimensional (2D) and obtained a parabolic growth rate law if oxygen surface diffusion and impingement on the island's perimeter is the dominant transport mechanism.

We have extended Orr's model to incorporate the 3-D growth. Following the derivation of Orr, oxygen surface diffusion to the perimeter of an oxide island creates a growth rate [85],

$$\frac{dN(t)}{dt} = 2\pi r K_S J_S , \tag{5.3}$$

where $N(t)$ is the number of oxygen atoms in a Cu_2O island at time t, r is the radius of the circular profile of an island, K_s is the sticking coefficient of oxygen to a Cu_2O island, and J_S is the diffusive flux of oxygen. For 2-D lateral growth of a disk-shaped island, with thickness a, then by solving the above differential equation, we see that the cross-sectional area increases parabolically with respect to time [85]. Following a similar analysis for 3-D growth of a spherical island, then the cross-sectional area, A, of the oxide island, is

$$A(t) = \frac{\pi \Omega K_S^2 D C_0}{D + L_d K_S}(t - t_0), \tag{5.4}$$

where Ω is the volume occupied by one O atom in Cu_2O, C_o is the surface concentration of oxygen far away from the Cu_2O islands, D is the surface diffusion coefficient of oxygen, L_d is the radius of the zone of oxygen capture. The power law dependence, t^2 for 2-D and t for 3-D, is independent of the shape of the island.

5.2 KINETICS OF INITIAL STAGES OF Cu(110) OXIDATION

5.2.1 Nucleation of oxide islands

The *in situ* observation of the island nucleation events as a function of time provides significant insights into the oxidation kinetics. Figure 5.1 (a) is a dark field TEM image taken from the $Cu_2O(110)$ reflection after the copper film has been cleaned with methanol. No oxide islands are visible in this region. Figure 5.1 (b-c) show the corresponding dark field images at the same area, as shown in Figure 5.1 (a), of the copper film at successive 10 minute time increments after oxygen was leaked into the column of the microscope. The partial pressure of oxygen was 5×10^{-4} torr and the temperature of the copper film was held at 350°C. After the introduction of oxygen gas, the nuclei appear after an incubation period of several minutes. After the oxidation of about 22 minutes, no new islands formed, and the islands reached the saturation density of the nuclei.

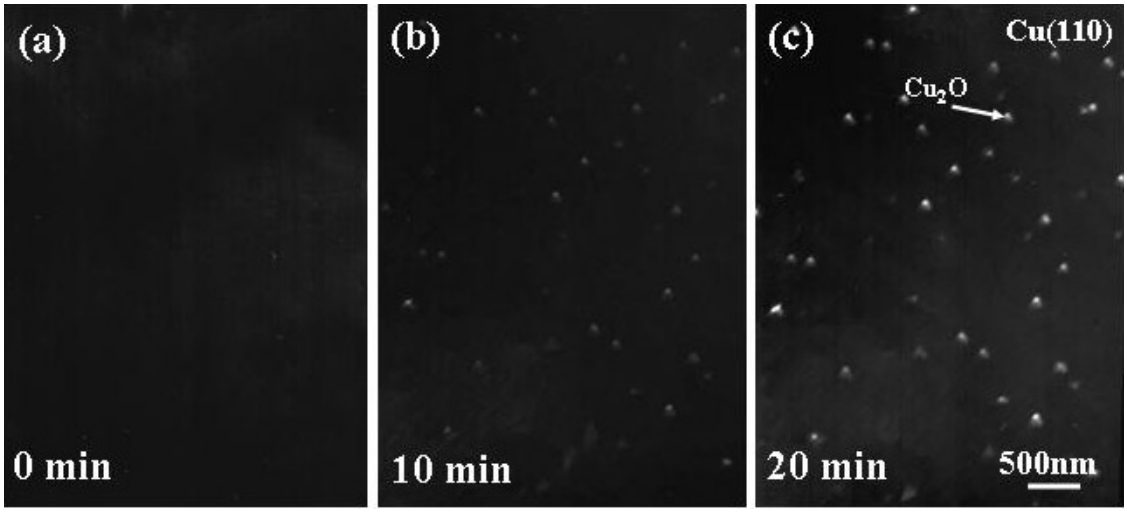

Figure 5.1 *In situ* dark field TEM images taken as a function of oxidation time, (a) 0 min, (b) 10 min, (c) 20 min, (d) 30 min at constant oxygen partial pressure of 5×10^{-4} and temperature of 350°C.

To measure quantitatively the number density and cross-sectional area of the oxide islands, the negatives were digitized with a Leafscan™ 45. The software packages Digital Micrograph™ and NIH Image™ were used to determine the number density and the cross-section as a function

of oxidation time. Figure 5.2 shows the experimental data and theoretical fit to equation (5.1). A good match is noted where the fit parameters are k =1.74 and L_d =0.33. Hence, the initial nucleation rate, k, is 1.74 μm^{-2} min^{-1}, and the saturation island density, $1/L_d^2$, is 9.01 μm^{-2}. In comparison, previous work on Cu(100) at the same oxidation conditions of 350°C and oxygen pressure of 5×10^{-4} torr revealed that the oxide islands reached saturation density of nuclei, 0.8 μm^{-2}, after 25 min oxidation [39]. The radius, L_d, of active zone of oxygen capture around each island was determined to be 1.09μm long before the islands impinge on each other. The initial nucleation rate, k, is 0.17 μm^{-2} min^{-1}.

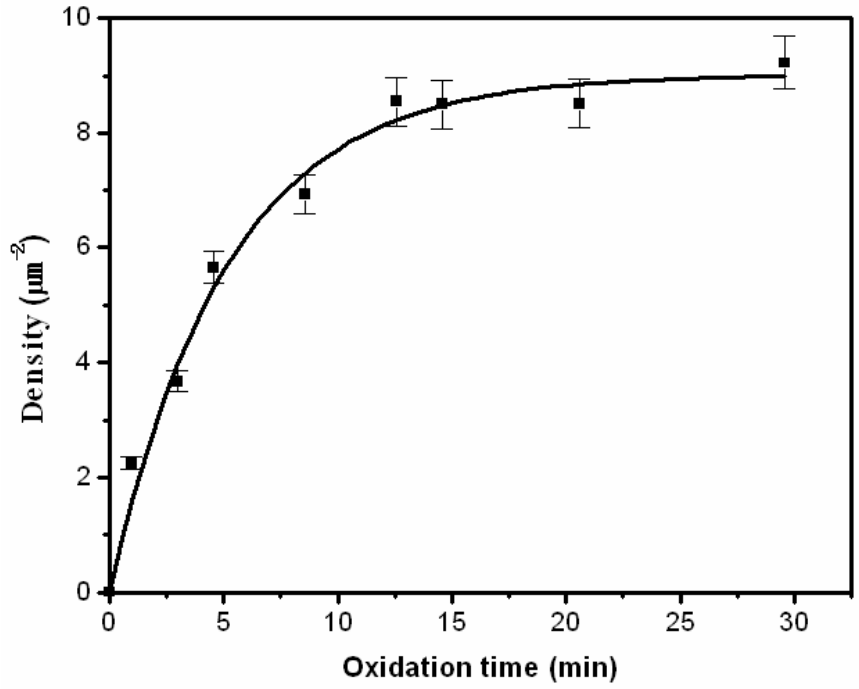

Figure 5.2 Cu_2O island density as a function of oxidation time at constant oxygen partial pressure of 5×10^{-4} and temperature of 350°C.

We measured the saturation density of the nuclei as a function of oxidation temperature, from 300°C to 450°C, at constant oxygen pressure of 5×10^{-4} torr. Figure 5.3 shows the saturation density of nuclei versus inverse of the oxidation temperature, where the activation energy, E_a, which is equal to the slope, was determined to be 1.1±0.2eV. In comparison, the activation energy, E_a, for Cu(100) was measured to be 1.4±0.2 eV [39].

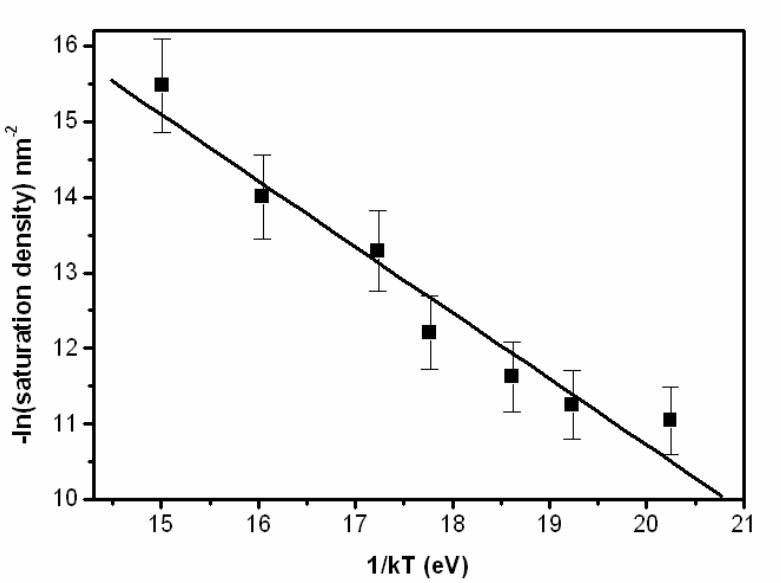

Figure 5.3 Cu_2O saturation island density versus inverse temperature. The absolute value of the slope is the E_a for the surface-limited process, E_a=1.1eV.

5.2.2 Growth of oxide islands

The evolution of the cross sectional area of the islands is recorded *in situ*, and a sequence of bright field images focusing on the growth of individual islands is shown in Figure 5.4, where the Cu(110) film was oxidized at 5×10^{-4} torr and 450°C. About a couple of minutes after the introduction of oxygen gas, Cu_2O islands were observed to nucleate rapidly followed by growth of these islands. After the initial nucleation of the oxide islands, ~5 minutes, the saturation density of the island nuclei was reached and no new nucleation event was observed, which is much faster than the oxidation at 350°C, where the saturation is reached after 22 min oxidation. Further oxidation causes the small Cu_2O islands only to grow, as can be seen in the BF micrograph in Figure 5.4, where the edges remain essentially flat and move outward.

Figure 5.5 is the comparison of the experimental data of the oxide volume to this surface diffusion model by using 3-D growth of the oxide island, Equation (5.4). The kinetic data on the evolution of cross-sectional area of the islands agree well with the model of surface diffusion of oxygen. Therefore, the excellent agreement of evolution of cross sectional area of the islands

with the kinetic model reveals that the growth of the 3-dimensional Cu_2O islands occurs by oxygen surface diffusion and impingement on the oxide perimeter.

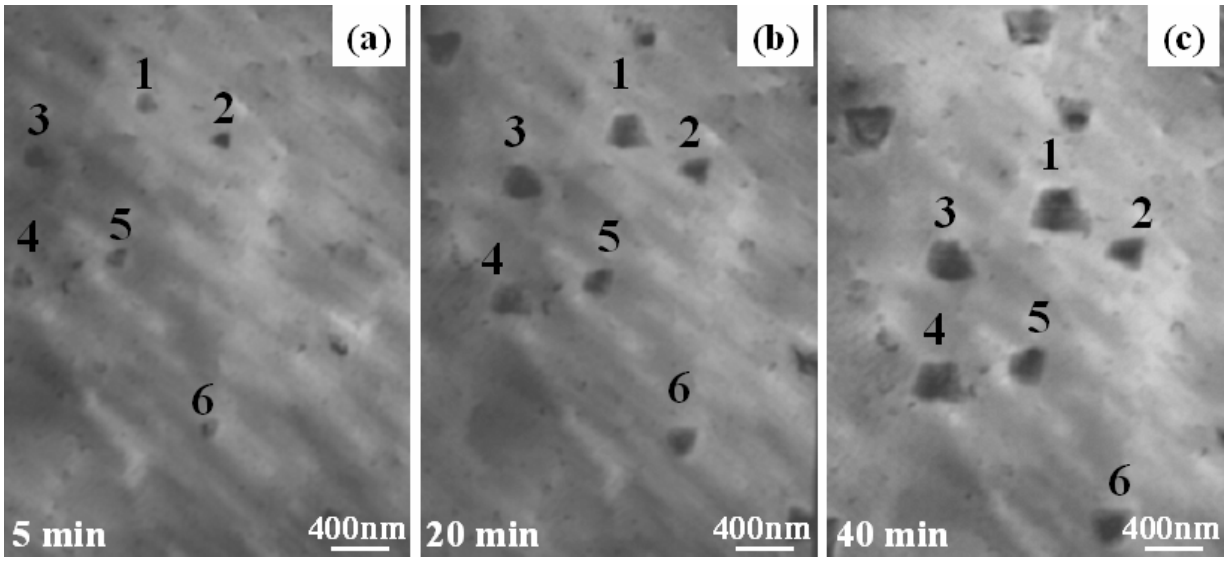

Figure 5.4 *In situ* bright field TEM image showing the growth of Cu_2O islands. Note that there is a saturation of the island nuclei at constant oxygen partial pressure of 5×10^{-4} and temperature of 450°C.

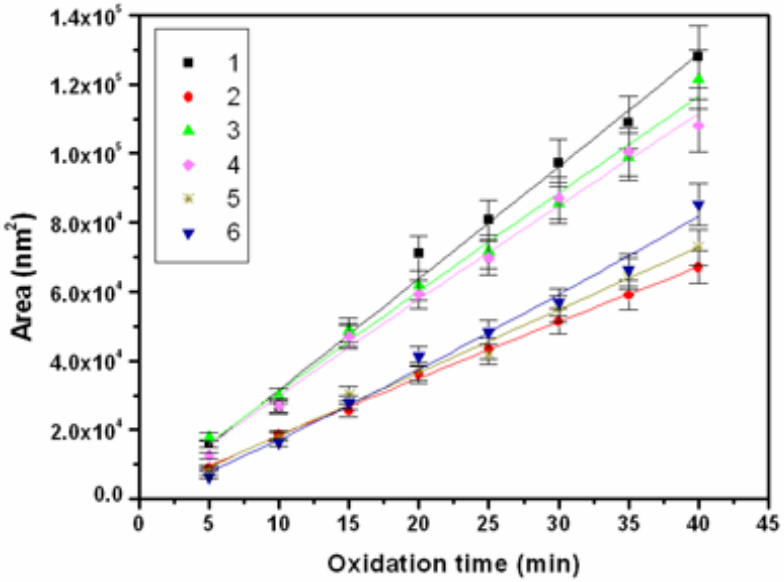

Figure 5.5 Comparison of the experimental data and the theoretical function for the surface diffusion for the 3-D growth of Cu_2O islands at constant oxygen partial pressure of 5×10^{-4} and temperature of 450°C.

5.2.3 Discussion

The comparison of the nucleation and growth behavior of Cu(110) with that of Cu(100) at the same oxidation temperature, (350°C), and oxygen pressure, (5×10^{-4} torr), revealed that the same surface diffusion models, originally developed to describe Cu(100) oxidation, explains the experimental data on Cu(110) quite well and demonstrates a greater generality of this oxygen surface diffusion model.

Since the initial oxidation stages are surface processes, it is reasonable to expect that the crystallographic orientation of the underlying metal will have a major effect on the nucleation behavior, growth rate and the orientation of the oxide film. Table 5.1 summarizes the values of the fit parameters for Cu(100) and Cu(110) oxidation. Differences in the rate, oxide island shapes, and fit parameters to the surface models were noted between Cu(100) and Cu(110). Specifically, The initial nucleation rate on Cu(110) is much faster than that on Cu(100). The saturation density on Cu(110) surface is 11 times larger than that on Cu(100). Hence, the active zone of oxygen capture around each island on Cu(110) is smaller than that on Cu(100). The activation energy, E_a, for the nucleation processes on Cu(110), was measured to be 1.1±0.2eV, which is also smaller than that on Cu(100) surface, 1.4±0.2eV.

Table 5.1 Comparison of fit parameters of Cu (110) and (100) oxidation

parameters	Cu(100)	Cu(110)
initial oxidation rate ($\mu m^{-2}min^{-1}$), k	0.17	1.74
saturation island density (μm^{-2}), $1/L_d^2$	0.83	9.01
radius of oxygen capture zone (μm), L_d	1.09	0.33
overall activation of nucleation (eV), E_a	1.4±0.2	1.1±0.2

To explain the differences in the fit parameters due to orientation, we consider the effects of kinetics and energetics, such as surface energies of the system, and the kinetics, in particular, on the diffusion and nucleation process.

Kinetics considerations

It should be noted that the diffusion of oxygen is on the reconstructed Cu surface. Previous investigators have elegantly demonstrated that Cu(100) and (110) surfaces are unreconstructed, and then transform into "missing-row" or "adding-row" reconstruction when exposed to oxygen [2-6]. Oxygen chemisorption on the Cu surface is the first step for the oxidation. We speculate that the impinging oxygen molecules dissociate into oxygen atoms, and the dissociated oxygen is adsorbed at the Cu surface to form Cu-O bonds and create a surface reconstruction. After reconstruction, the oxygen atoms diffuse on this reconstructed surface, and nucleation occurs on the reconstructed Cu-O surface. Further arriving oxygen can either nucleate new oxide islands by reacting with copper atoms or attach to an existing island, causing growth. Therefore, the surface diffusion coefficient of oxygen determines the outcome of the competition between nucleation and growth, and, hence, contributes to the number density of stable islands. Qualitatively a larger diffusion coefficient for oxygen should yield a lower number density of stable islands. Since the path length of oxygen surface diffusion depends on the atomic structure of the substrate plane, different nucleation behavior of Cu_2O islands is, therefore, expected for different orientations of the Cu. The Cu(100) has a more close-packed structure, and is smoother than the corrugated Cu(110) surface. Similarly, the reconstructed $\left(\sqrt{2}\times 2\sqrt{2}\right)$R45º O-Cu(100) surface has a more compact oxygen chemisorption than (2×1)O-Cu(110) surface which has a corrugated structure, as shown in Figure 5.6. Therefore, it is reasonable to expect the activation barrier of surface diffusion of the dissociated oxygen will be higher on the Cu(110) surface, and thus have a shorter path length. The shorter diffusion path length will give rise to a smaller capture zone of oxygen and create a higher number density of oxide nuclei. This is confirmed by our results where the active zone of oxygen capture around each island on Cu(110) is 0.33μm, which is smaller than that on Cu(100), 1.09μm.

Energetics considerations

In order to form oxide islands on the surface, the system should overcome an activation barrier whose height is given by the work of formation of the critical nucleus. The number of critical nuclei per unit area is:

$$N_{r^*} = N_0 \exp\left(-\frac{\Delta G^*}{kT}\right) \tag{5.5}$$

where r^* is the radius of the critical nucleus, N_0 is the number of adsorption sites per unit area of substrate surface, ΔG^* is the Gibbs free energy of formation of the critical nucleus, and k and T have their usual meaning. The main contributions to ΔG^* are volume free energy, surface/interfacial energy, and interfacial strain energy due to lattice mismatch during the formation and growth of the oxide nuclei.

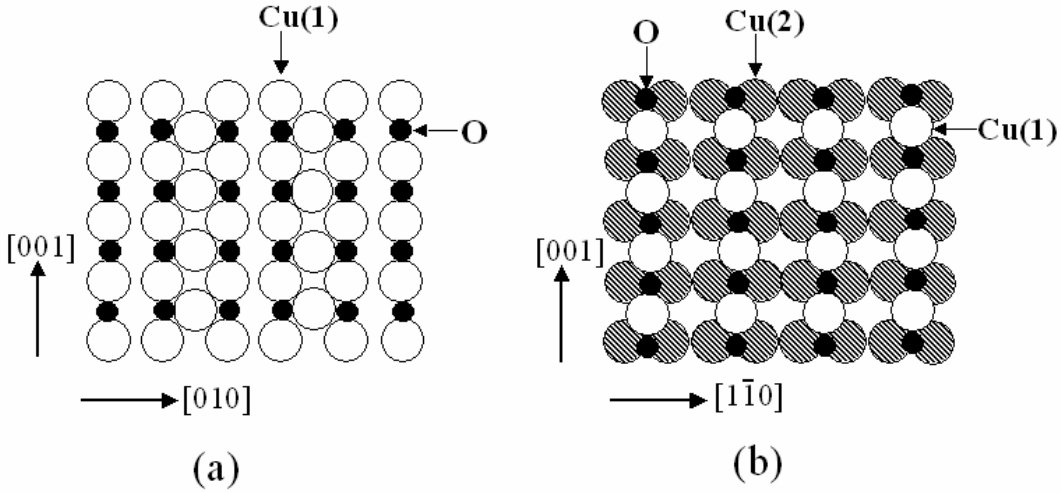

Figure 5.6 Schematic diagram of the reconstructed $\left(\sqrt{2}\times 2\sqrt{2}\right)$R45º O-Cu(100) surface (a), and (2×1)O-Cu(110) surface (b) due to oxygen chemisorption. Filled circles: O atoms; open circles: top layer Cu atoms; shaded circles: second layer Cu atoms.

The volume free energy should be the same for the oxide islands formed on Cu(100) and (110) surfaces since only Cu_2O was observed to form. The Cu/Cu_2O lattice mismatch will cause strain in the oxide islands, and this strain can be relaxed to some degree by the distortion of the substrate [77]. Therefore, the interfacial strain energy could depend on orientation since it is a function of the Poisson ratio, (ν), and shear modulus, (μ), of the substrate, and oxide island bulk stress (σ_b) [77, 86]. In the epitaxial growth of oxide islands, the difference in surface energies of Cu(110) and (100) should play an important role in the nucleation behavior. The surface energy of Cu(100) is 1280mJ/m^2, which is lower than the Cu(110), 1400mJ/m^2 [100]. Therefore, it is expected that the Cu(110) surface will be less stable and the nucleation of oxide islands will be

facilitated. As a result, the Cu(110) surface has a higher nuclei density of oxide and smaller overall activation energy for the nucleation of the oxide islands as confirmed by our measurements.

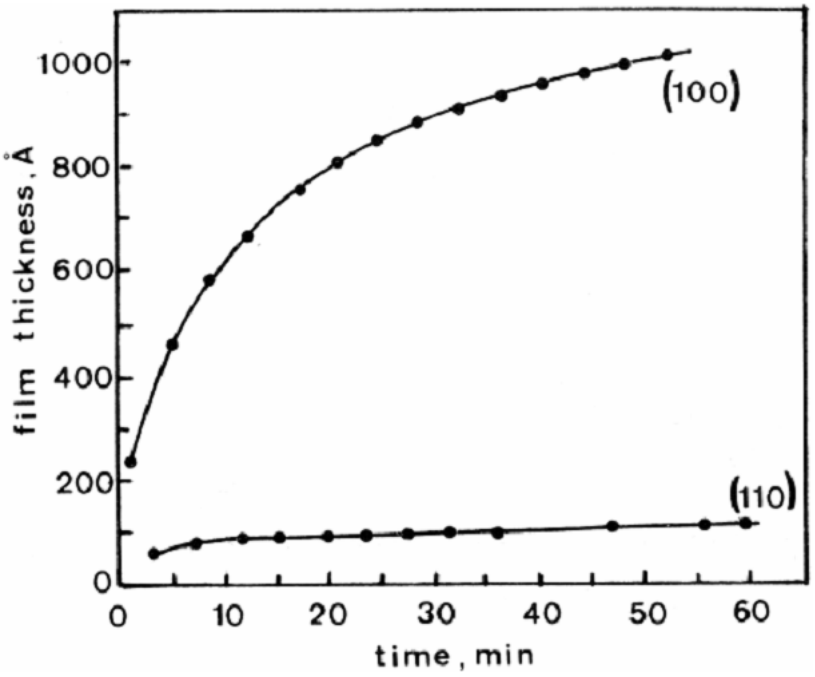

Figure 5.7 Oxidation kinetics of copper single crystals at 523K and 1 atm of oxygen from Lawless and Gwathmey (see reference [52]).

Comparison to previous research on Cu oxidation and impact on Cu passivation

Previous research by K.R. Lawless and A.T. Gwathmey [52] in the oxidation of a spherical single crystal of Cu with its multitude of surface orientations demonstrated the anisotropy of the oxidation rate on different faces. Figure 5.7 is a reproduction of their experimental data on Cu(100) and Cu(110) in which Cu(100) has a much faster oxidation rate than Cu(110). The early work on Cu(100) and the present Cu(110) work have demonstrated that the oxide film nucleates and grows as oxide islands, not as a uniform layer, even at atmospheric pressure [38-40]. During the progressive exposure of the Cu surface to oxygen, several stages are identifiable. The first stage is the dissociation and chemisorption of oxygen on the Cu surface. With the further exposure to oxygen, the epitaxial nuclei of oxide islands appear on the reconstructed surface after an incubation period. The islands will grow and begin to coalesce with the continued exposure to oxygen. In these stages oxygen transport is dominated by surface and interface

diffusion. Once coalescence has completed, there should then be a sudden reduction in the growth rate of the oxide, due the change of oxidation of the surface to diffusion through an oxide layer. Therefore, the self-limiting oxidation is due to the coalescence of islands, which switches off the surface diffusion route and requires much slower bulk diffusion for further oxidation.

As discussed in the preceding paragraph, Cu(110) shows a faster nucleation rate of oxide with higher oxide densities than that on Cu(100) in the initial stage of oxidation. Therefore, there is a faster coalescence of oxide islands on Cu(110) than that on Cu(100). In the oxidation of Cu(100), it takes a longer oxidation time for the coalescence of oxide islands due to a smaller density of oxide nuclei and slower growth rate. As a result, the Cu_2O formed on Cu(110) coalesces earlier to a thinner passive oxide layer than Cu(100) and the rate then slows down as compared to Cu(100) oxidation, as confirmed by Lawless and Gwathmey's work [52]. Surprisingly, orientations that form a higher density of oxide nuclei and have a faster initial oxidation rate, may have a slower long-term growth rate due to the rapid coalescence of the oxide which switches the oxide growth mechanism from surface diffusion to the slower diffusion through an oxide scale.

5.3 TEMPERATURE EFFECTS ON THE GROWTH OF OXIDE ISLANDS

In this work we investigated the effect of oxidation temperature on the oxide growth on a Cu(110) surface during the initial stages of oxidation and the effect of oxygen pressure on the nucleation of oxide islands. We examined the Cu_2O island formation on Cu(110) as a function of oxidation temperature in the range of 450°C to 650°C and oxygen pressure of 0.1 torr. Epitaxial, three-dimensional, trapezoid island formation was observed for oxidation at all the temperatures and it was found that increasing oxidation temperature increased the thickening rate of the oxide islands. The oxidation at 0.1 torr was noted to have a smaller nucleation activation energy for the oxide formation as compared to lower pressures. The results presented here reveal the differences observed for Cu(100) and Cu(110) and the effects of surface structure on the oxidation kinetics, thereby on oxide morphology.

5.3.1 Experimental observations

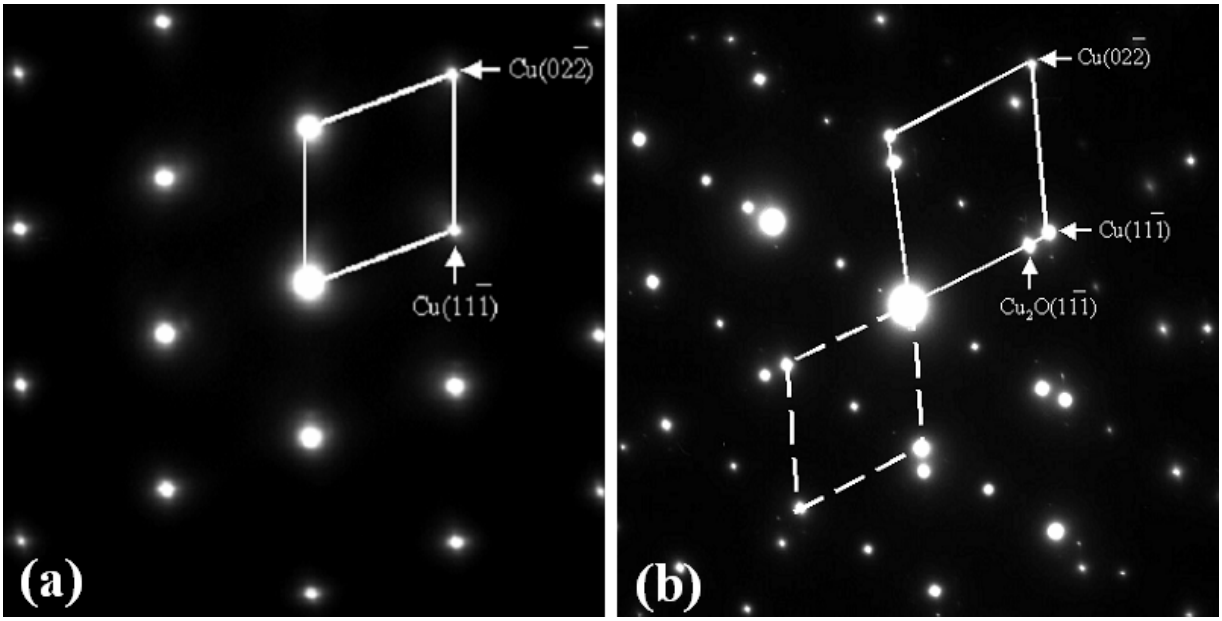

Figure 5.8 The epitaxial growth of the oxide on Cu(110) surface: (a) before oxidation; (b) after oxidation.

We examined the Cu_2O island formation as a function of oxidation temperature in the range of 450°C to 650°C at 0.1 torr of oxygen pressure. Three-dimensional island formation was observed for all the temperatures, and the selected area electron diffraction pattern of the Cu_2O island and the underlying Cu(110) substrate revealed that the oxide island is epitaxial with the Cu substrate, i.e. $(0\bar{1}\bar{1})$Cu//$(0\bar{1}\bar{1})$$Cu_2O$ and (100)Cu//(100)Cu_2O, as shown in Figure 5.8.

Figure 5.9 shows the dark field TEM images of the oxide islands formed at the different oxidation temperatures but constant oxygen pressure of 0.1 torr, where the Cu(111) reflection was used for imaging. The oxide islands formed at the different oxidation temperatures have the same trapezoid cross-sectional shape, but different TEM thickness fringe contrast. Figure 5.9 (a) shows that no thickness fringe contrast occurred in the islands with the lateral size of ~250nm at the low temperature oxidation (~450°C). Figure 5.9 (b) reveals that the oxidation at the elevated temperature (~500ºC) resulted in thickness fringe contrast in the island at the lateral size of ~250nm. The oxidation at 650ºC caused the sharp thickness fringe contrast in the island at the size of 200nm.

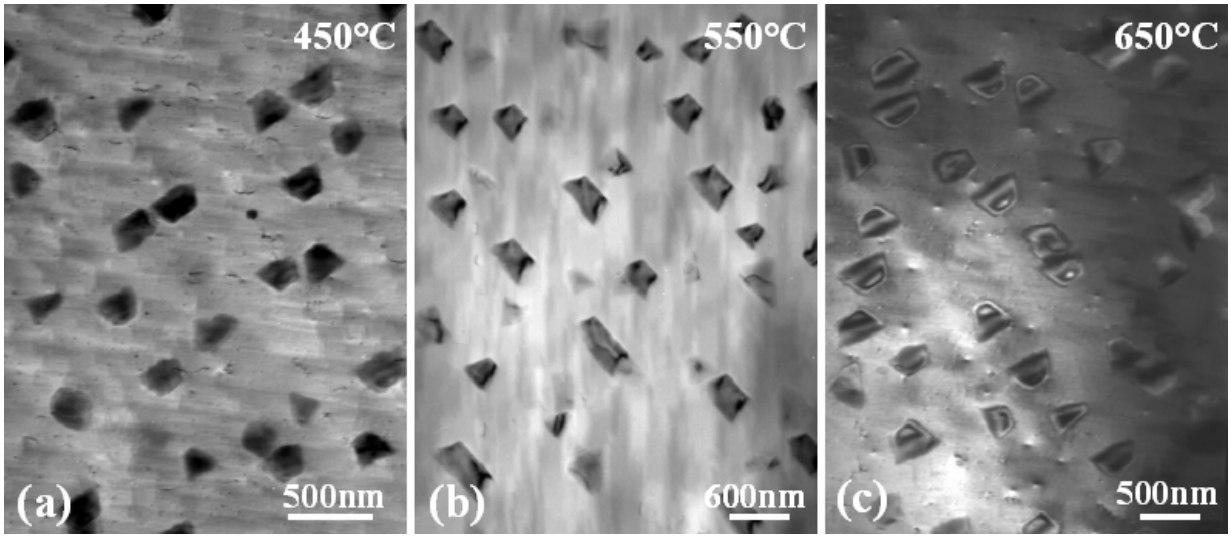

Figure 5.9 The dark field images of oxide islands formed on Cu(110) at the different oxidation temperatures, the oxygen pressure is 0.1 torr.

From the Howie-Whelan equations, the intensity from a diffracted beam, g, is directly proportional to $\sin^2(\pi t / \xi_g)$ in the Bragg condition, where t is sample thickness, and ξ_g is the extinction distance [101]. Therefore, the sample thickness can be estimated by the periodicity of the thickness fringe and ξ_g. By applying this relationship, we made an estimation of the island thickness. $\xi_{Cu(111)}$ is 24nm for the 100kV electron beam. In Figure 5.9 (a), since no thickness fringes occur in the islands, the thickness change of Cu from Cu surface to the bottom of the island along the inclined Cu/Cu_2O interface is less than 24nm. Therefore, the penetration thickness of the oxide islands inside the Cu film is less than 24nm. In Figure 5.9 (c), two dark fringes are observable, indicating the thickness change of the Cu film along the inclined Cu/Cu_2O is close to 36nm. The thickness of the Cu film in Figure 5.9 (b) is in the range of 24-36nm.

Figure 5.10 (a) shows the AFM image of the Cu_2O islands obtained at 650°C, which reveals the trapezoid cross-sectional morphology of the island, similar to the TEM observation. Figure 5.10 (b) shows the cross-sectional profile along the marked line in Figure 5.10 (a). The surface topology reveals that the oxide island has a flat top and the island height is approximately equal to 23nm. The island thickness in the Cu film was estimated to be ~40nm by considering the conversion of the displaced copper atoms that had occupied the region of the Cu_2O island. The

AFM image analysis of the islands obtained at the lower temperatures revealed similar features of the islands, i.e., contact angle, island surface flatness, as those in Figure 5.10 (a), but different island heights. The height of the islands formed at 550°C is ~16nm, and the island thickness underneath the Cu film was estimated to be ~25nm. Similarly, the penetration thickness of the islands formed at 450°C was calculated to be ~22nm. By measuring the contact angles between the island side-facets and the Cu substrate and combining the epitaxial relationship between Cu and Cu_2O (Figure 5.10 (c)), we determined the island structural geometry as shown in Figure 5.10 (d).

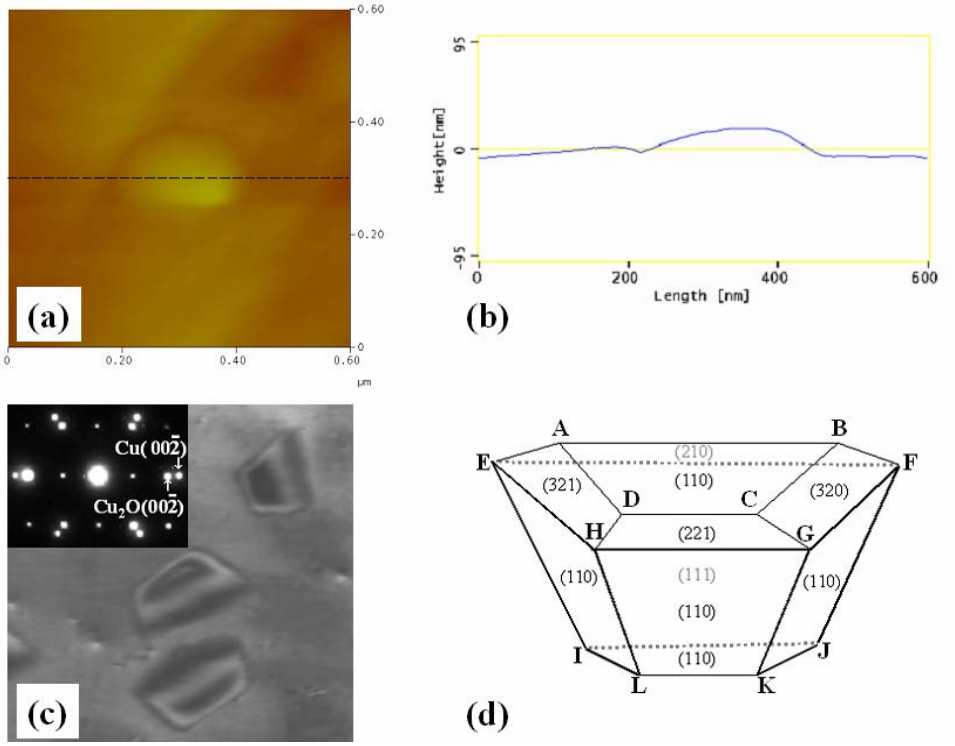

Figure 5.10 (a) AFM image of Cu_2O islands formed on Cu(110) at 650°C; (b) cross-sectional profile drawn along the marked lines indicated in (a); (c) the epitaxial relationship of the islands with substrate, where the SAD is oriented with the Cu film; (d) structure model of the island based on the AFM and TEM measurements.

One consequence of oxygen surface diffusion being the mechanism for nucleation is that there is a saturation density of oxide islands [39]. This is due to the existence of a zone of oxygen capture around each oxide island, where the radius of this zone is dependent on oxygen pressure and oxidation temperature. For a constant oxygen pressure, the saturation island density

dependence on temperature follows an Arrhenius relationship, $N_S \sim e^{-E_a/kT}$, where k is Boltzmann's constant, T is the oxidation temperature, E_a is the activation energy for the oxide nucleation which depends on the energies of nucleation, oxygen surface diffusion, adsorption and/or desorption of oxygen [33].

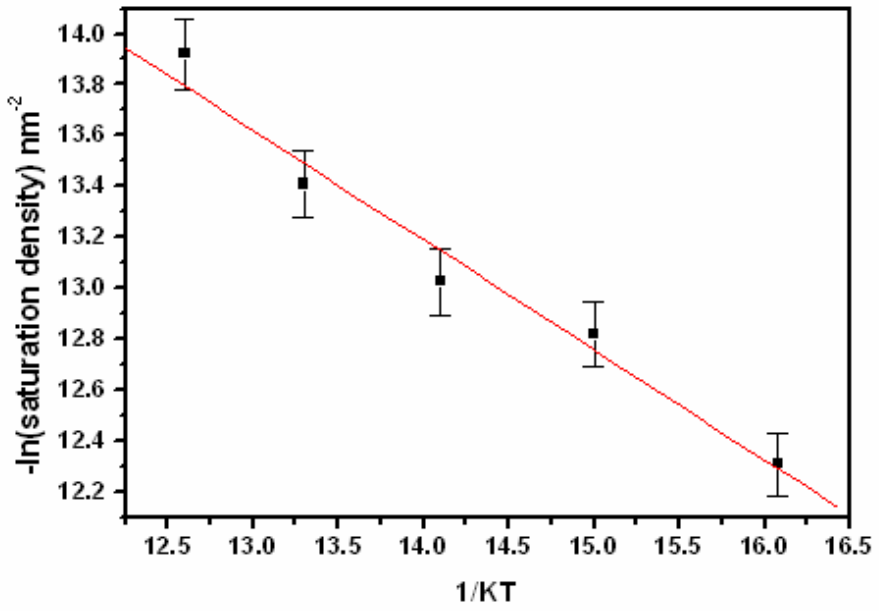

Figure 5.11 Cu_2O saturation island density versus inverse temperature. The absolute value of the slope is the E_a for the surface-limited process.

We measured the saturation density of the oxide islands at the temperatures from 450°C to 650°C at the oxygen pressure of 0.1 torr. Figure 5.11 shows the saturation density of islands follows an Arrhenius dependence on temperature. Since the nucleation process involves oxygen surface diffusion, adsorption and/or desorption, and these processes have an Arrhenius dependence on temperature. Therefore, the activation energy obtained from the saturation island density at the different temperatures includes the oxygen surface diffusion, adsorption and/or desorption. The activation energy, E_a, which is equal to the slope in Figure 5.11, was determined to be 0.4±0.04eV. In comparison, the activation energy, E_a, for Cu(110) at the temperatures between 300°C to 450°C at constant oxygen pressure of 5×10^{-4} torr, was measured to be a higher value of 1.1±0.2 eV [102]. Since we cannot follow the nucleation events and the growth of the oxide islands as a function of oxidation time inside the TEM at the high oxygen pressure

($P(O_2)>10^{-3}$ torr), therefore, a deeper understanding of the oxidation at high oxygen pressure needs more theoretical simulation work to determine the kinetics, such as the dominant mechanism for the oxide nucleation. Other investigators in this group are working on this subject.

5.3.2 Discussion

Effects of temperature on the kinetics/energetics of oxide formation

During the initial stages of oxidation, the growth of the oxide islands is accompanied by the conversion of copper atoms to Cu_2O islands along the Cu/Cu_2O edge. Figure 5.9 indicates that the oxidation temperature had a large effect on the island thickness growth, i.e., the oxidation at high temperature enhances a growth into the Cu substrate. The growth of the islands into the Cu substrate creates an inclined Cu/Cu_2O interface which causes the TEM thickness fringe contrast. Figure 5.12 is a schematic drawing of the islands formed at the different temperatures. At the low temperature, 450°C, the islands have a shallow penetration into the substrate, and a small thickness variation as shown in Figure 5.12 (a). The oxidation at the high temperature results in formation of the islands with deeper penetration, and a large thickness variation along the inclined interface as shown in Figure 5.12 (b, c).

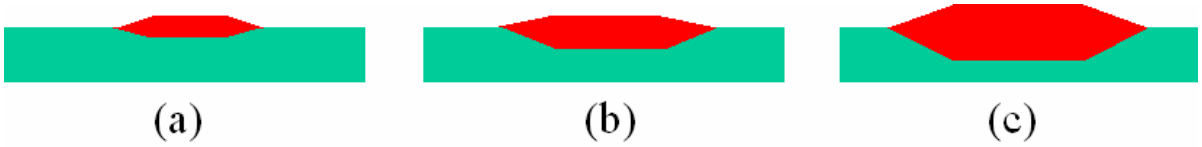

Figure 5.12 Schematics of the oxide islands formed at the different oxidation temperatures (a) 450°C; (b) 550°C; (c) 650°C.

The oxide island structure is controlled by thermodynamic and/or kinetic factors during the oxidation reaction. The free energy change for the formation of oxide islands can be expressed as

$$\Delta G = \Sigma A_s \gamma_s + \Sigma A_i \gamma_i + \Delta G_{vol}(Cu_2O) - \Sigma A_{Cu} \gamma_{Cu}, \qquad (5.6)$$

where $\Sigma A_s \gamma_s$ is the island surface energy, $\Sigma A_i \gamma_i$ is the interfacial energy, $\Delta G_{vol}(Cu_2O)$ is the volume free energy for the formation of Cu_2O, and $\Sigma A_{Cu} \gamma_{Cu}$ is the surface energy of Cu before the oxide formation. It is known that Cu_2O has a thermal expansion coefficient of 1.9×10^{-6} °C^{-1},

and Cu has a thermal expansion coefficient of 17×10^{-6} °C^{-1}. With increasing temperature, the lattice mismatch (~15%) between Cu and Cu_2O becomes smaller and this lattice mismatch induced interfacial strain is reduced. Therefore, the islands tend to prefer the structure with large interface area at higher temperature, such that a thicker oxide (and more compact) island formed at high temperature is more energetically favorable than an island with larger surface area.

We have considered the energetics, but the island growth depends also upon the kinetics. The formation of Cu_2O islands on Cu creates a Cu_2O/Cu interface. The oxygen diffusion coefficient, D, follows an Arrhenius relationship, $D \sim e^{-E_a/kT}$, where E_a is the activation energy for diffusion. Different oxidation mechanisms have different E_a values. It is well known that the activation energy for surface diffusion is typically smaller than the other diffusion mechanisms and it has been previously demonstrated that the oxide growth is dominated by the surface diffusion of oxygen to the perimeter of the oxide islands when the temperature is lower than 500°C in the oxidation of Cu(110)[102]. However, with the oxidation temperature increasing, there will be an enhanced kinetics of oxygen interfacial diffusion which may contribute to the growth of the oxide island into the Cu film.

Effect of oxygen pressure on the activation energy for the oxide nucleation

The initial stages of oxidation involve oxygen surface adsorption, surface mobility, rearrangements in the adsorbed layer and trapping of the mobile oxygen to form relatively stable and usually ordered structures. This sequence of steps is similar to condensed vapors to a first approximation. On the other hand, rigorous formulation of the nucleation and growth process for oxide formation is more complex than simple vapor condensation. The thermodynamic parameters characteristic of the reaction species are more difficult to evaluate, and the reaction path is more complex. However, it is possible to formulate a simple model which is helpful to make qualitative predictions from it for experiments where conditions are carefully controlled. In order to form oxide islands on the surface, the system should overcome an activation barrier whose height is given by the work of formation of the critical nuclei. For heterogeneous nucleation of oxide islands, this activation energy is

$$\Delta G^* = f(\theta)\sigma^3 \frac{1}{(\Delta G_V + \Delta G_S)^2}, \tag{5.7}$$

where $f(\theta)$ is the geometric factor of the surface energy, and σ is oxide surface energy, ΔG_V is the free-energy change which drives the oxidation reaction, ΔG_S is the strain energy due to the lattice mismatch between the oxide and the metal substrate. ΔG_V can be determined through the oxidation reaction, $2Cu(s) + 1/2O_2(g) = Cu_2O(s)$,

$$\Delta G_V = \left(\Delta G^0 - \frac{RT}{2} \ln P_{O_2} \right) / V^0, \tag{5.8}$$

where R is the gas constant, and T is the oxidation temperature, P_{O_2} is oxygen pressure, V^0 is molar volume, and ΔG^0 is the standard free change for the formation of Cu_2O and for the oxidation temperature range used in these experiments, ΔG^0 can be calculated suing Equation (5.9) [48]

$$\Delta G^0 = -130{,}930 + 94.5T \text{ J/mole} \tag{5.9}$$

By applying the above equations, we consider the effects of the oxygen pressure on the nucleation thermodynamics. Because the sign of ΔG^0 is negative, and ΔG_V will be more negative with the increase in the oxygen pressure. While ΔG_S is positive, the overall energy barrier to nucleation, ΔG^*, decreases with the increase in the oxygen pressure. This analysis is consistent with our measurements that activation energy for the oxide formation at the oxygen pressure of 0.1 torr is 0.4±0.04 eV, which is smaller than the oxidation at the oxygen pressure of 5×10^{-4} torr where the activation energy was measured to be 1.1±0.2 eV [102].

5.4 OXIDATION KINETICS OF ROUGHENED Cu(110) SURFACE

A systematic investigation of crystal surfaces plays an important role in the understanding of many physical and chemical processes ranging from surface reconstructions to adhesion, wetting, catalysis, crystal growth, *etc.*. The simplest surface one can conceive is an atomically smooth, low index facet that separates a crystalline surface from vapor. But the surface of a solid can go through different disorder stages from a perfectly flat, zero temperature configuration up to the melting temperature of the bulk material. A well-characterized phenomenon is surface roughening, first proposed by Burton, Cabrera, and Frank [103], which is typically characterized in terms of the appearance of hills and valleys of arbitrary height on the surface by the thermal

generation of atomic steps at the roughening temperature. Predictions of surface roughening transitions have been known for many years and several experimental studies have been reported for metallic surfaces [70, 104-107]. A surface undergoes a roughening transition, where steps form spontaneously at a critical temperature, when the free energy of step formation, $\Delta G = \Delta H - T \times \Delta S$, becomes zero. ΔH is the enthalpy required for step formation, and ΔS is the entropy change with the formation of steps. In general, the roughening transition temperature of a surface can be estimated from the step energies.

The low-index Cu(110) surface is known to show an anomalous thermal behavior. Previous experiments indicated that the Cu(110) surface has either a roughening or pre-melting transition, or both at temperatures below its bulk melting point (T_M=1356K) [70]. The thermal disorder of the Cu(110) surface below T_M has received considerable interest both experimentally and theoretically [70, 107-109]. It is generally believed that strongly anharmonic vibrations of surface atoms are responsible for the increase of disorder. The roughening transition temperature, T_R, can be estimated using Equation (5.10) [110, 111]

$$T_R = (2/\pi) d^2 \gamma / k_B , \tag{5.10}$$

where k_B is the Boltzman constant, d is the step height on the surface, and γ is the surface tension. In the case of Cu(110), d=1.28Å, and γ=1.3J/m^2. Using this expression, one obtains T_R=710ºC, which is very close to the experimental result [70].

Various surface probe techniques, such as low-energy ion scattering, inverse photoemission, thermal He scattering, X-ray scattering, high-resolution electron energy loss spectroscopy, have provided indirect evidence about the increase of disorder on Cu(110) between 500 and 1000K [112-114]. It is generally believed that strongly anharmonic vibrations of surface atoms are responsible for the increase of disorder in this temperature regime [115]. The advent of UHV and modern surface analysis, STM, low energy electron microscopy (LEEM) or surface X-ray diffraction have allowed observations of roughening phenomena down to atomic scales in well-controlled conditions [70, 107, 108, 116]. Until now, the thermal behavior of metal surfaces has not been investigated by TEM due to experimental difficulties, particularly in providing a UHV environment. Here we present a direct, real time, experimental investigation of the thermal surface roughening of Cu(110) surface by the *in situ* UHV TEM and its effect on the oxidation kinetics.

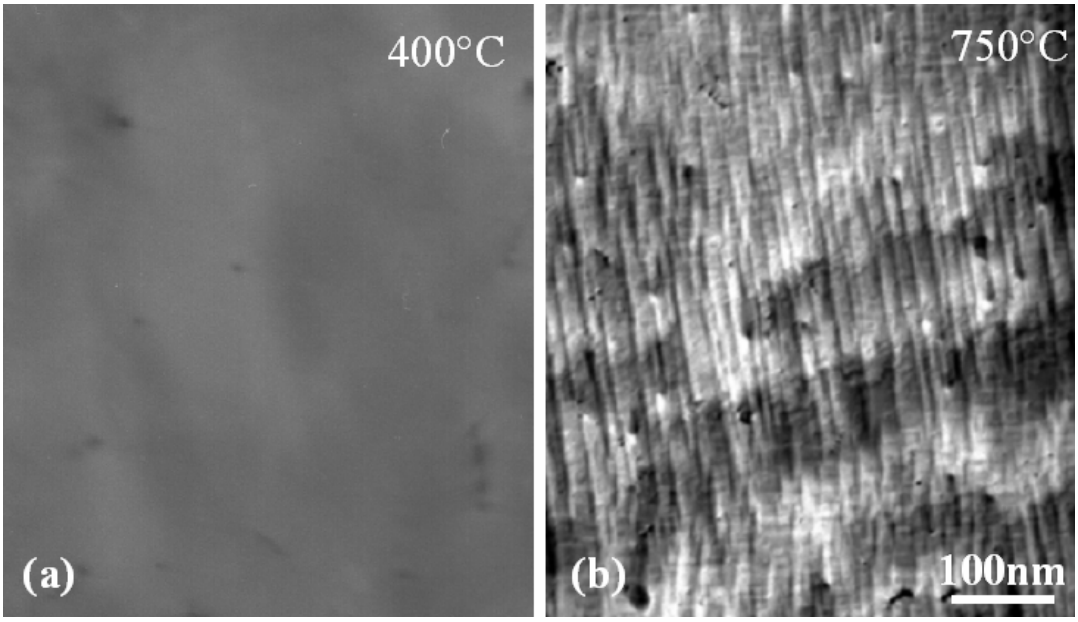

Figure 5.13 Cu(110) surface (a) before surface roughening; (b) thermal roughening at 750°C.

Figure 5.13 shows the surface morphology of Cu(110) before and after surface roughening. The surface resembled a hill-and-valley structure aligned along [001] direction over distances larger than 1000nm. The spacing between valleys or hills was typically 10 nm in the [110] direction.

It is known that surface oxidation includes many complex processes, such as oxygen surface adsorption, oxygen induced surface reconstruction, oxygen surface diffusions, etc. Thus, surface roughening, a dramatic surface structural change, will affect the oxidation kinetics greatly. Therefore, we investigated the kinetics of the oxide nucleation and growth on the roughened Cu(110) surface at temperatures above the roughening transition temperature.

5.4.1 Nucleation on roughened (110) surface

The *in situ* observation of the island nucleation events on the roughened surface as a function of time provides significant insights into the effects of surface roughening on the oxidation kinetics. Figure 5.14 shows the *in situ* oxidation of the roughened Cu(110) surface, where the oxidation temperature is 750°C and the oxygen pressure is 5×10^{-4} torr. Figure 5.14 (a) is a BF TEM image of the copper film which has undergone surface roughening at 750°C. No oxide islands are

visible in this region. Figure 5.14 (b-c) show the corresponding BF images at the same area as shown in Figure 5.14 (a) of the copper film at successive 2 minute time increments after oxygen was leaked into the column of the microscope. The partial pressure of oxygen was 5×10^{-4} torr and the temperature of the copper film was held at 750°C. After the introduction of oxygen gas, the nuclei appear after an incubation period of ~ten seconds. After 4 minutes, no new oxide islands formed, and the islands reached their saturation density. The SAD pattern of the Cu_2O island and underlying Cu(110) substrate revealed that the oxide island is epitaxial with the underlying Cu film, where $(1\bar{1}0)Cu//(1\bar{1}0)Cu_2O$ and [001]Cu//[001]Cu_2O. A same epitaxial relationship was noted for Cu(110) without surface roughening at the lower oxidation temperatures.

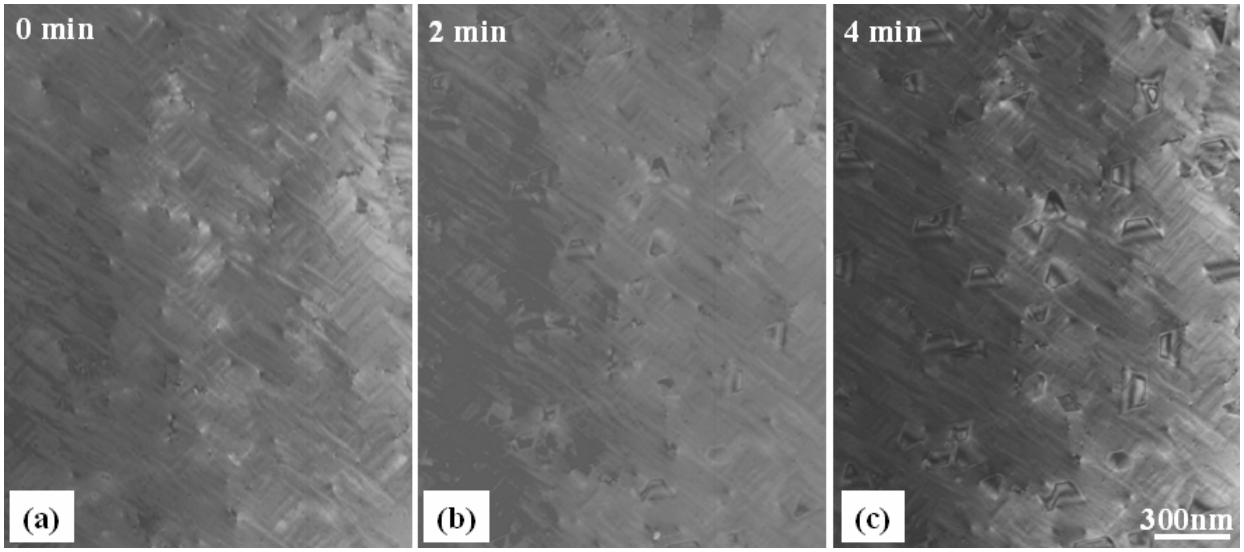

Figure 5.14 The *in situ* observation of the oxidation on the roughened Cu(110) surface at the temperature of 750°C and oxygen pressure of 5×10^{-4} torr, (a) 0 min, (b) 2 min, (c) 4 min

Figure 5.15 shows the experimental data and theoretical fit to equation (1), the "zone of oxygen capture" model. A good match is noted where the fit parameters, the initial nucleation rate, k, is 5.29 μm^{-2} min^{-1}, and the saturation island density, $1/L_d^2$, is 4.34 μm^{-2}. In comparison, the oxidation on Cu(110) at the lower temperature of 350°C, but same oxygen pressure of 5×10^{-4} torr revealed a larger saturation density of 9.01 μm^{-2}, but a slower initial nucleation rate, k, 1.74 μm^{-2} min^{-1}. The oxide island shape is the same as compared to the temperature lower than the surface roughening, but the density and nucleation and growth rate of the oxide islands is altered.

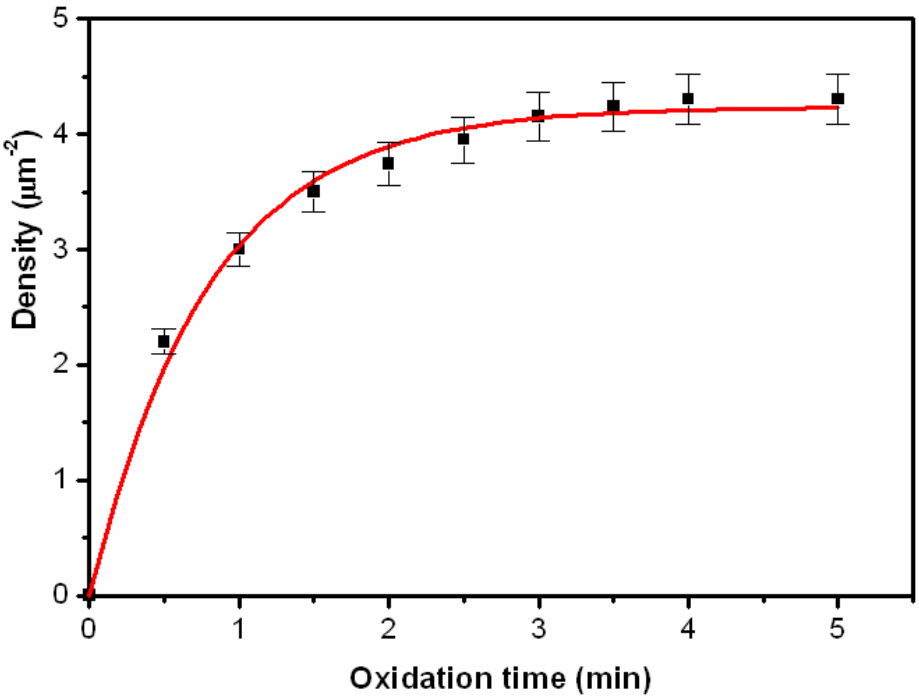

Figure 5.15 Cu_2O island density as a function of oxidation time at constant oxygen partial pressure of 5×10^{-4} and temperature of 750°C.

5.4.2 Growth of oxide islands on roughened (110) surface

Based on the surface diffusion of oxygen, for 2D lateral growth of oxide islands with constant thickness, and then by solving the differential equation, (5.3), the cross-sectional area increases parabolically with respect to time. Following a similar analysis for 3D growth of oxide islands, the cross-sectional area of the oxide islands increases linearly with respect to time. Since the 3D growth of the oxide occurs, confirming the linear dependence of the island growth on t implies that surface diffusion is the dominant transport mechanism. If the time dependence is not linear, then another mechanism must contribute or dominate the initial oxide growth.

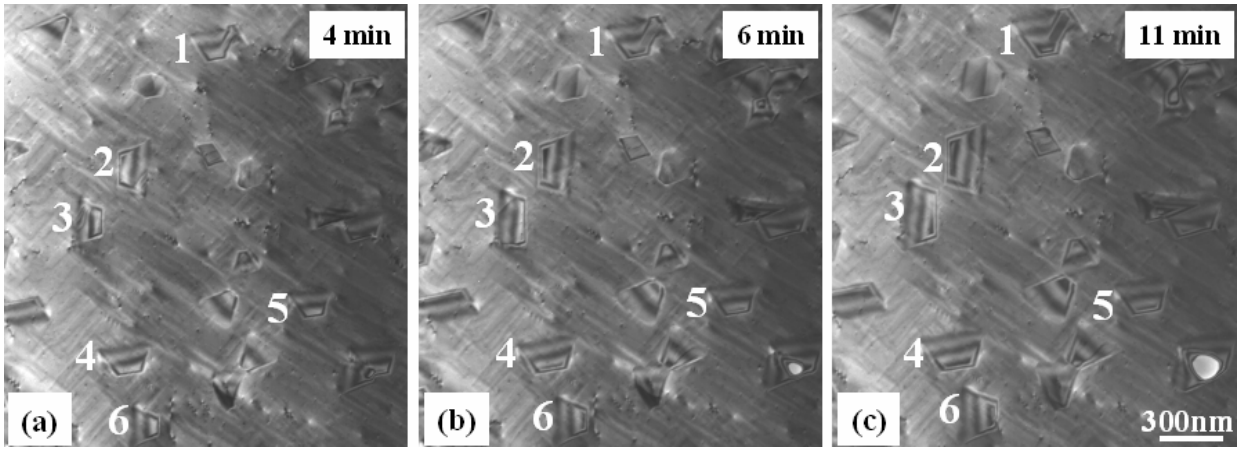

Figure 5.16 *In situ* observation of the growth of oxide islands on the roughened surface.

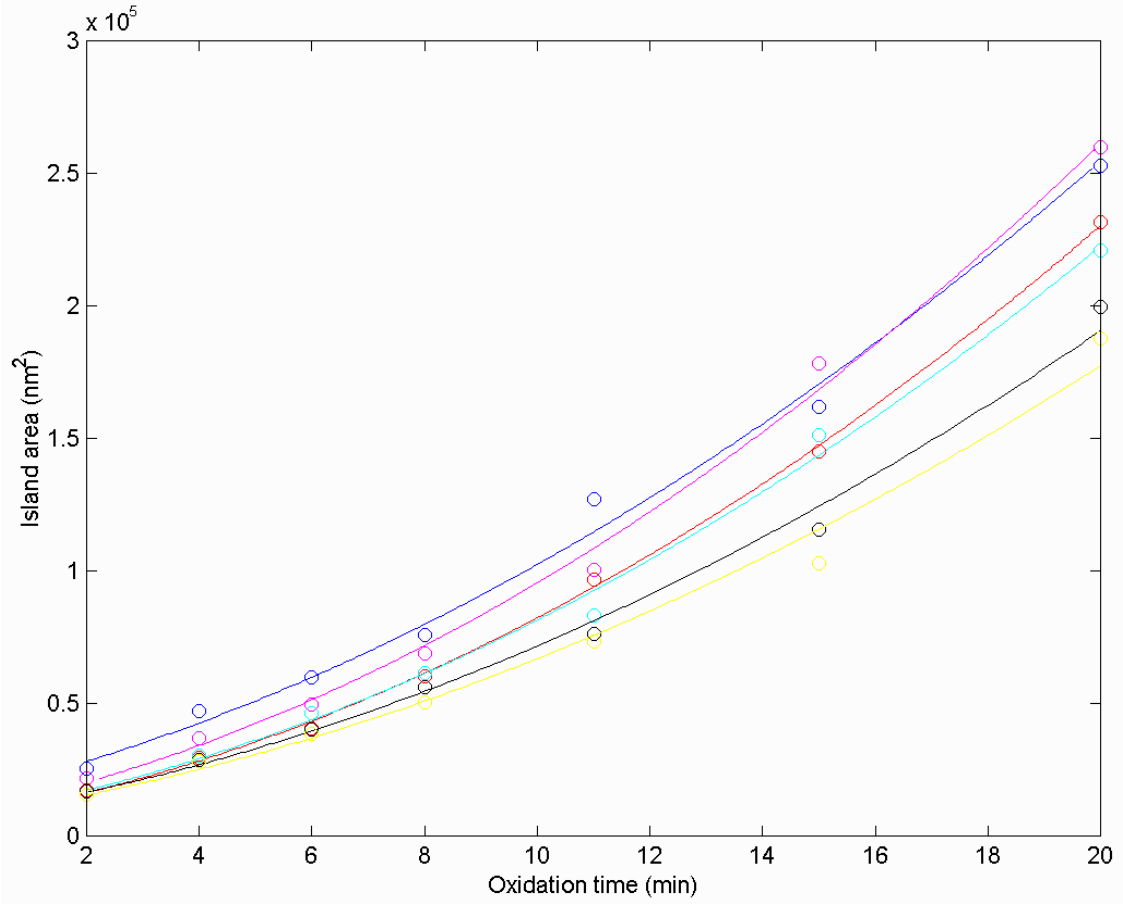

Figure 5.17 Comparison of the experimental data and the theoretical function for the surface diffusion for the 3-D growth of Cu_2O islands.

The evolution of cross sectional area of the islands was recorded *in situ*, and a sequence of images focusing on the growth of individual islands is shown in Figure 5.16, where the Cu(110) film was oxidized at 5×10^{-4} torr and 750°C. About 30 seconds after the introduction of oxygen gas, Cu_2O islands were observed to nucleate rapidly followed by growth of these islands. After the initial nucleation of the oxide islands, ~4 minutes, the saturation density of the island nuclei was reached and no new nucleation event was observed, which is much faster than the oxidation at 350°C, where the saturation is reached after 22 min oxidation.

The best power fit to the experimental data on the island growth is 1.4. This power law is higher than t — the predicted power law dependence for 3D growth by oxygen surface diffusion. To account for the deviation from a linear power law, other mechanisms besides oxygen surface diffusion were considered.

We expect that for the oxidation on the roughened Cu(110) surface at the high temperatures, the kinetics of island growth are as follows. As oxygen arrives on the surface and diffuse to the perimeter of oxide islands through surface diffusion, the oxygen atoms may be incorporated into Cu_2O islands by reacting with Cu atoms adjacent to the perimeter of the islands. Another likely possibility is the direct impingement of oxygen which is incorporated onto the oxide islands by further interface diffusion. The combination of surface diffusion of oxygen to the perimeter of the oxide island plus direct impingement and interface diffusion of oxygen into the oxide island creates a growth rate of the island

$$\frac{dN}{dt} = c_1 f_1 \times L + c_2 f_2 \times A \tag{5.11}$$

where N is the number of oxygen atoms in Cu_2O island at time t, c_1 is the sticking coefficient for oxygen surface diffusion, f_1 is the surface diffusion flux of oxygen, c_2 is the sticking coefficient for direct impingement, f_2 is the flux of oxygen for direct impingement, L is the island perimeter and A is the island surface area. By assuming a spherical shape of the island and solving the above differential equation (5.11), the cross-sectional area, A, of the oxide island increases with respect to oxidation time and can be expressed as follows [40]:

$$\frac{A^{1/2}}{\pi^{1/2}K_2} - \frac{K_1}{{K_2}^2}\ln\left(K_1 + \frac{K_2}{\pi^{1/2}}A^{1/2}\right) = t - t_0 \tag{5.12}$$

where

$$K_1 = \frac{C_1 f_1 \Omega}{2}, \qquad K_2 = \frac{C_2 f_2 \Omega}{2}$$

and Ω is the atomic volume of oxygen in Cu_2O. In this equation, K_1 is the parameter related to the contribution of oxygen surface diffusion to the oxide island growth, K_2 is the parameter related to the contribution of direct impingement and interface diffusion to the oxide growth. By using Equation (5.12), we obtained an excellent fit to the combined surface diffusion and direct impingement/interface diffusion model, as shown in Figure 5.17; The fit parameters for surface diffusion and direct impingement/interface diffusion are listed in Table 5.2. Hence, the growth of the oxide islands is initially dominated by both oxygen surface diffusion and direct impingement/interface diffusion.

Table 5.2 Comparison of fit parameters of the island growth on roughened Cu(110) surface

	Island 1	Island 2	Island 3	Island 4	Island 5	Island 6
$K_1\left(\frac{atom \cdot nm^2}{sec}\right)$	79.72	106.88	81.23	93.10	74.93	70.74
$K_2\left(\frac{atom \cdot nm}{sec}\right)$	10.51	9.94	10.13	10.99	9.14	8.79

5.4.3 Discussion

The present results indicate that temperature and surface roughness of the substrate play an important role in the oxidation behavior of Cu(110). The flatness of the surface influences the surface diffusion of oxygen, and the oxidation temperature influences both the surface and interface diffusion of oxygen. The comparison of the nucleation and growth behavior of roughened Cu(110) surface with that of smooth Cu(110) at the low oxidation temperature (350°C), but same oxygen pressure, (5×10^{-4} torr), revealed that the same surface diffusion model explains well the experimental data regarding the oxide nucleation, but does not quite match for the oxide growth. Accordingly, the nucleation of oxide islands on a roughened surface is still a surface controlled process, but the growth of oxide islands is controlled by both oxygen surface diffusion and direct impingement/interface diffusion. A possible reason for the difference is that the oxidation of Cu(110) at $T < T_{rough}$ was not carried out long enough for the Cu_2O islands to cover a large area where the direct impingement mechanism is not noticeable. It is reasonable to

expect with large oxide coverage, direct impingement will play a significant role in the oxide growth.

Effect of surface roughening on nucleation kinetics

Since nucleation is a surface process, it is reasonable to expect that surface structure of the underlying metal will have a major effect on the nucleation behavior. For the same surface structure, the surface diffusion of oxygen follows an Arrhenius relationship with temperature, i.e., higher mobility of oxygen at higher temperature. The attachment of oxygen to existing islands is more favorable than the nucleation of new nuclei at high temperature. Hence, the dependence of saturation island density on temperature for the same surface structure follows a similar Arrhenius relationship on oxidation temperature. Table 5.3 summarizes the values of the fit parameters for the oxidation on Cu(110) at 350°C (flat surface) and 750°C (roughened surface). Differences in the initial oxidation rate, capture zone of oxygen, and saturation island density, were noted. It is reasonable to expect that the initial oxidation rate, k, and the capture zone of oxygen, become larger with increasing temperature, as shown in the table. Assuming that the (110) surface does not undergo surface roughening at 750°C and has the same surface structure as in the temperature range (300°C~500°C), then the saturation density of oxide islands at 750°C can be deduced to be ~0.01 μm^{-2}, which is much smaller than the experimental measurement, 4.3 μm^{-2} for the same oxygen pressure (5×10^{-4} torr). Hence, it is reasonable to expect that the surface roughening increases the activation barrier for oxygen surface diffusion, thereby decreasing the mobility of oxygen, which gives rise to a smaller capture zone of oxygen and creates a higher number density of oxide nuclei.

Table 5.3 Comparison of fit parameters of Cu (110) oxidation before/after surface roughening

parameters	350°C	750°C
initial oxidation rate ($\mu m^{-2}min^{-1}$), k	1.74	5.29
saturation island density (μm^{-2}), $1/L_d^2$	9.01	4.34
radius of oxygen capture zone (μm), L_d	0.33	0.48

The comparison of the oxidation of Cu(100) and (110) at the same oxidation temperature (350°C) and oxygen pressure, (5×10^{-4} torr), indicated that Cu(110) surface has a much faster nucleation rate than Cu(100). This was explained by the enhanced roughness of Cu(110) due to its O-chemisorption corrugation, as discussed in chapter 5.2.3. The present observation of the oxidation on a roughened Cu(110) surface is consistent with the same argument, i.e., increased surface roughness enhances the oxide nucleation.

Effect of surface roughening on the oxide growth

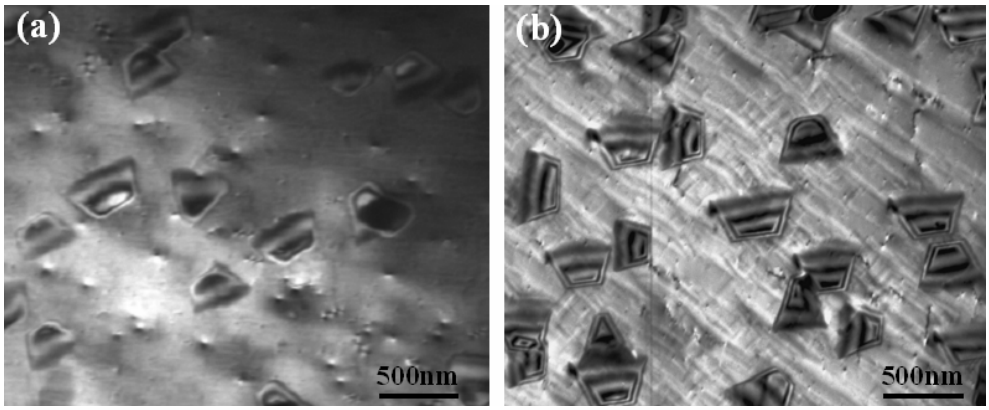

Figure 5.18 The dark field images of oxide islands formed on (a) flat Cu(110) surface (650°C); and (b) thermally roughened surface (750°C) at the same oxygen pressure (5×10^{-4} torr) and oxidation time (~10 min).

The oxidation of Cu(110) at the different temperatures resulted in the formation of the oxide islands with the same morphology, but different thickness contrast in the islands. We compare the island size with thickness fringes formed at the different oxidation temperatures. In the oxidation of flat Cu(110) surface, no thickness contrast appears in oxide islands with sizes up to 500nm when the oxidation temperature is lower than 500°C. When the oxidation temperature is at 650°C, thickness contrast appears in the oxide islands with a size of ~200nm. Figure 5.18 shows the dark field TEM images of the oxide islands formed at 650°C and 750°C, where Cu(111) reflection was used for imaging. The islands formed on a flat surface and roughened surface have similar trapezoid shape. However, the islands formed at the two temperatures have different periodicity of the thickness fringes although their difference in lateral size is small. The thickness of the islands underneath the Cu film was estimated to be ~36nm (650°C) and 48nm

(750°C) respectively, by the periodicity of the thickness fringes. Therefore, the oxide islands on the roughened surface have a faster thickening rate than that of the flat surface.

The formation of oxide islands with increased oxide thickness at the high temperature is energetically favorable. With increasing temperature, the lattice mismatch (~15%) between Cu and Cu_2O is reduced due to their different thermal expansion coefficients. As a result, the lattice mismatch induced interfacial strain is reduced. Therefore, the islands tend to prefer the structure with large interface area, which is thicker and more compact at high temperature. Also, this thicker and more compact structure can decrease the island surface area, which reduces the surface energy of the islands. Therefore, this morphology is more energetically favorable than an island with larger surface area.

5.5 OXIDATION ON FACETED Cu(110) SURFACE

Apart from the surface roughening, another important surface phenomenon is surface faceting, the breaking up of a flat surface into facets of different orientations [109, 117-122]. Faceting can be classified into thermal faceting, where the surface is altered at elevated temperatures due to the thermodynamic instability [109, 119], and reaction faceting [121, 122], where the surface is altered due to the adsorption of a chemical species. In the case of the surface being thermodynamically unstable, the faceting generally proceeds much slower than reaction faceting and is often observed only at higher temperatures. From a theoretical point of view, the thermal faceting is related to the macroscopic crystal equilibrium shapes and it was recognized that the driving force for the faceting is the anisotropy of the surface free energy which is a characteristic of solid surfaces. It is generally believed that faceting occurs in order to reduce the overall surface free energy.

Thermal faceting is generally a complex, multi-step process, and models for how surface faceting begins were first developed by Mullins [123]. Mullins predicted that faceting begins with the nucleation and growth of individual facets, where the driving force is the decrease in surface free energy caused by the formation of new surfaces of different orientations. In the later stages of faceting, the facets grow in size by a process of coarsening. Here, the increase in average facet size with time is due to the reduction of surface free energy because a completely

faceted surface can lower its free energy by reducing the facet nodes. Experimental evidence for faceting coarsening has been observed for stepped Si(113) surfaces where the mechanism was attributed to attractive interactions between thermally fluctuating steps [124].

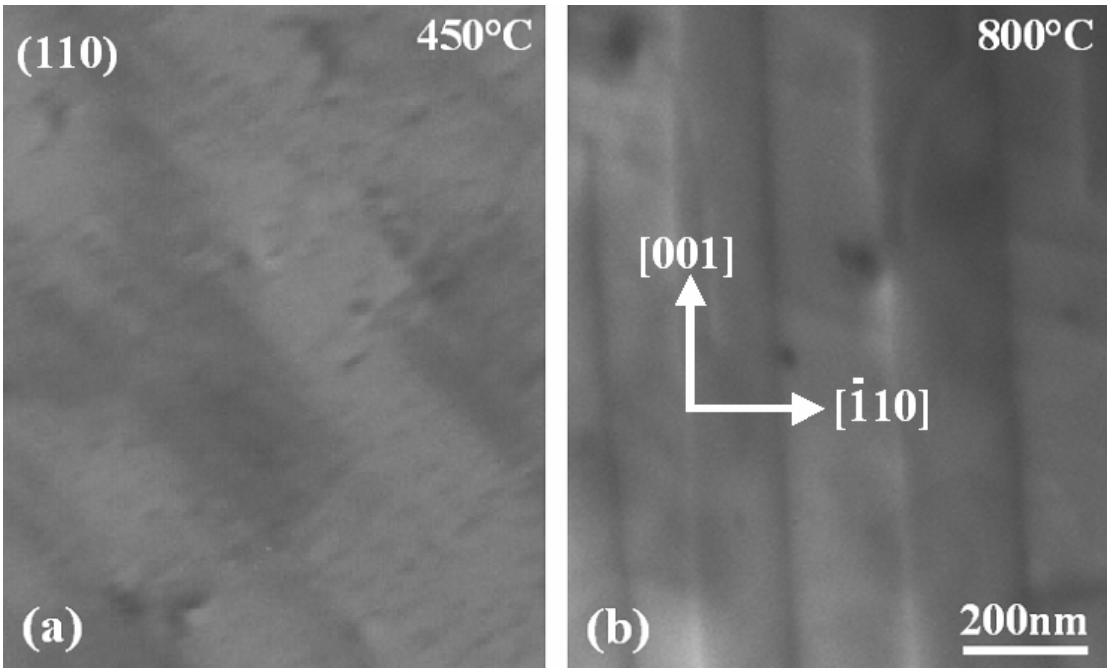

Figure 5.19 The surface faceting of Cu(110) films at the elevated temperature (a) Cu(110) surface originally annealed at 450C; (b) after 40 minutes annealing at ~800C.

As we have discussed, Cu(110) exhibits surface roughening at 710ºC. However, when the Cu(110) film was heated to a slightly higher temperatures, surface faceting was also observed. Figure 5.19 shows the surface faceting of Cu(110) films at the temperature of 800ºC, where Figure 5.19 (a) is the surface before faceting, and Figure 5.19 (b) is a completely faceted surface due to long time annealing (~40 mins) at this temperature.

As introduced earlier, the faceting involves the nucleation and growth of individual facets. Therefore, faceting coarsening can be thought of as the elimination of small facets from the surface. For a complete facet surface, the increase in its average facet size must eliminate some number of facets over a given area. Figure 5.20 is a surface annealed for 20 minutes at 800ºC. Many facet junctions appear during this faceting stage. It was proposed that a mechanism for the elimination of facets is the motion of facet junctions [125]. By this mechanism, the surface could increase the average facet size and decrease the boundaries separating the two surface

orientations. Therefore, the density of the facet junctions will decrease with long time annealing. This is confirmed in Figure 5.19 (b), where the sample was annealed at the temperature for 40mins.

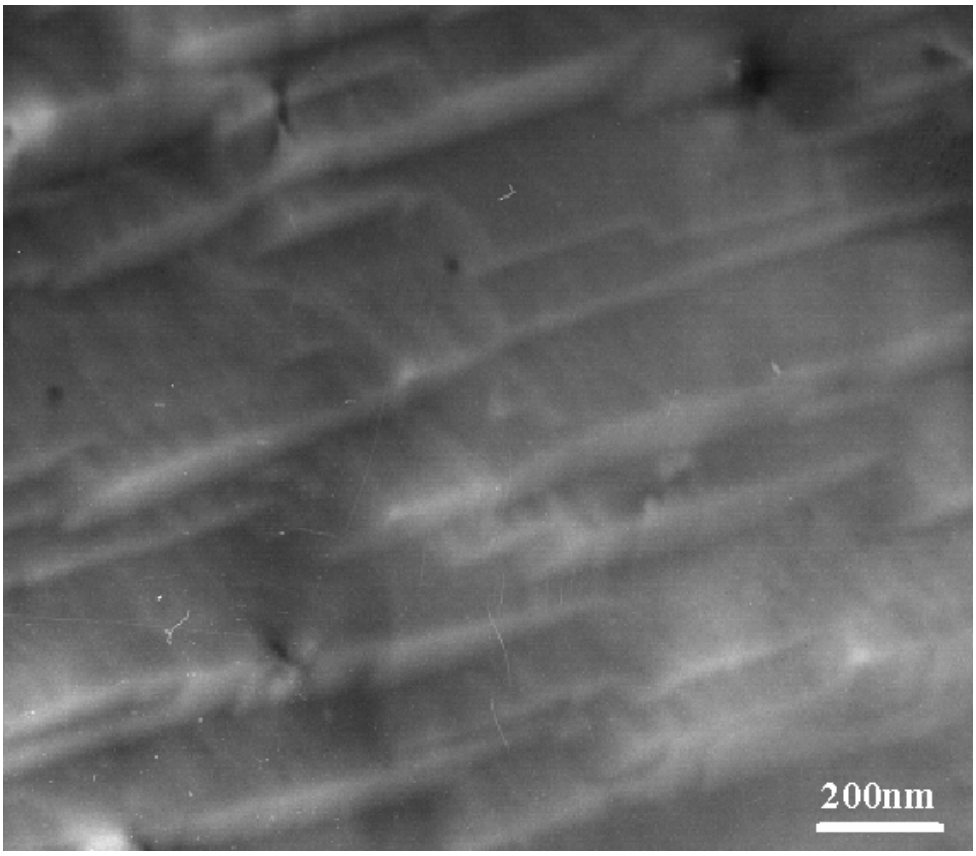

Figure 5.20 The surface with numerous facet junctions.

It is known that the faceting process includes individual facet nucleation and growth, and once facet nucleation has begun, surface diffusion can become the dominant process in facet growth and coarsening and significant mass transfer is involved during this process. Therefore, the reason why we observed the surface faceting on the Cu(110) surface near the roughening temperature could be due to the specific sample geometry in our experiments, where the Cu thin films were very thin and were free standing. So the surface diffusion of Cu atoms can occur on both surfaces of the Cu film during the faceting process. The faceting of free standing thin films should differ from the semi-infinite surface because the fast surface diffusion of atoms occurs on both sides of the films, which provides a significant contribution to the mass transfer involved in the growth of facets, especially at very high temperatures.

It has been reported that vicinal surfaces are used for fabricating magnetic wires by an epitaxial growth method [126-128]. Similarly, the faceted surfaces provide many hill-valley structures which could be used as templates for fabricating nanostructures. We demonstrated this by oxidizing the faceted Cu(110) surface and obtaining the template-patterned distribution of oxide island arrays on it as shown in Figure 5.21, where the oxide islands grew as elongated islands along [110] directions and were aligned to each other along [110], where they nucleated in the "valleys" of the surface facets.

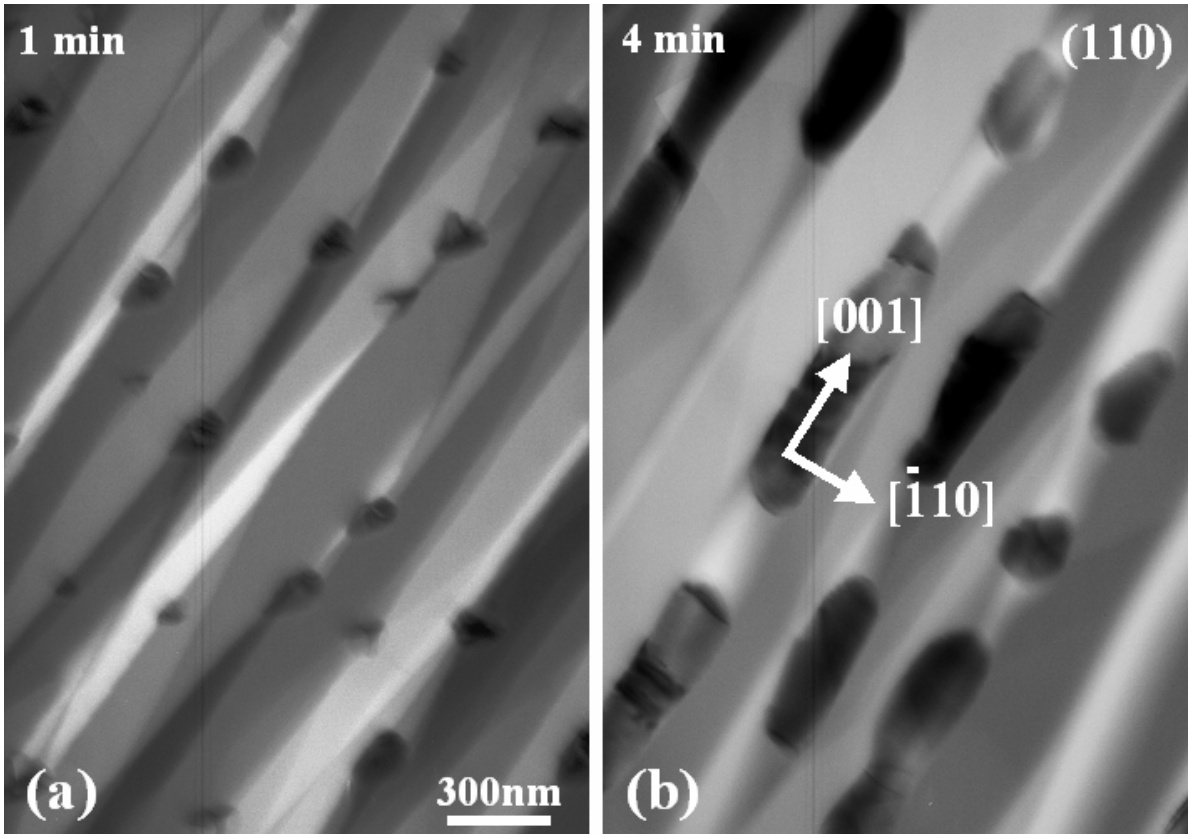

Figure 5.21 The oxidation on the faceted surface Cu(110) surface at 800ºC.

The epitaxial formation of oxide islands on surfaces includes nucleation and growth processes. The nucleation of oxide islands at nadirs of the intersection of the two facets seems to be more energetically favorable than at the intersection top, as shown in Figure 5.22 because the configuration in Figure 5.22 (a) minimizes the surface and interface of the island as compared to (b). Therefore, the intersection nadirs provide the preferred sites for oxide nucleation. Similarly, the growth along the intersection direction will be also more energetically favorable. This

mechanism is responsible for the formation of one dimensional Cu_2O structures within the "valley" of the faceted surface.

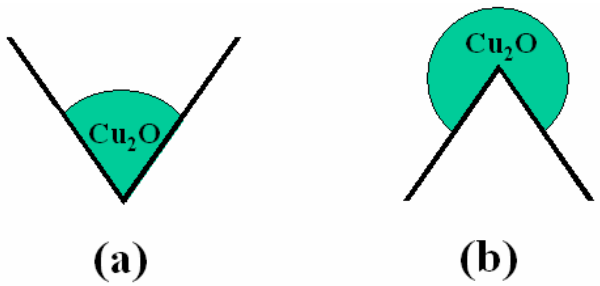

Figure 5.22 Nucleation of an oxide island at (a) nadir and (b) top of the intersection of two facets.

5.6 CONCLUSIONS

Cu(110) surface shows thermal roughening (T_r=700°C) and thermal faceting (T_f=800°C). When the temperature is below T_r, the surface can be considered to be smooth. The kinetic data on the nucleation and growth of the 3-dimensional oxide islands on the smooth surface (300°C<T<700°C) agree well with the heteroepitaxial model of surface diffusion of oxygen. The data in this temperature range indicate that a fast initial oxidation rate will give rise to a slow, long term, oxidation rate due to the rapid coalescence of the oxide islands which switches off the fast surface diffusion of oxygen to slow bulk diffusion, and which may explain the passivation difference between Cu(100) and Cu(110). The oxidation on the roughened surface (T_r<T<T_f) results in homogeneous distribution and a very high number density of oxide islands. The fit of the dynamic data on the nucleation and growth of the oxide islands to the oxygen surface diffusion model shows a much smaller oxygen capture zone, thereby providing a highly enhanced nucleation rate on the roughened Cu(110) surface as compared to a smooth Cu(110) surface. The oxidation on the faceted surface (T>T_f) temperature results in heterogeneous nucleation of oxide islands in facet valleys and growth along the valleys.

6.0 Cu(111) OXIDATION

The oxidation on Cu(111) surfaces has been reported to be less than on the other two orientations and some controversy on the structures of the oxide formed on this surface exists. Some investigators reported that the oxidation of Cu(111) results only in disordered structures, not only at room temperature, but also even at elevated temperatures [129-132]. However, other investigators reported the formation of epitaxial oxide films on Cu(111) by exposure to O_2 with subsequent annealing, and the oxide thin films have the Cu_2O structure and are well-ordered [52, 133, 134]. Also, other types of ordered structures formed on Cu(111) by high temperature oxidation have been reported [1, 12, 135-138]. However, from this body of work, it has been established that for exposures $<10^4$ L a disordered oxygen chemisorbed layer is formed and that exposures $>10^5$ L cause the formation of a Cu_2O film. It is generally accepted that within the disordered chemisorbed layer, the positions of Cu atoms are severely perturbed from those that are adopted in the clean surface.

Although all investigators agree on this particular aspect, there is still no consensus on the exact structures of the chemisorbed oxygen layer and the subsequent oxides. The earliest structural investigation of the oxygen chemisorbed layer on Cu(111) was a low energy ion scattering study by Niehus [130]. This work indicated a lateral displacement of surface Cu atoms and formation of a rough oxygen overlayer with a corrugation of ~0.3 Å. In two later investigations, attempts were made to determine the local registry of the chemisorbed species [139, 140]. In both of these studies, it was suggested that the chemisorbed surface layer has a Cu_2O-like structure, and oxygen atoms occupy threefold hollow sites and partially penetrate the surface layer, causing a lateral expansion of the Cu atoms in the hollow site. It was postulated that the lateral expansion was accommodated by the surface through rumpling, causing the formation of a roughened surface. The structure of the disordered chemisorbed oxygen on Cu(111) was also investigated by normal incident X-ray standing wavefield absorption (NIXSW) and it was found that the oxygen atoms within the Cu_2O-like structure overlayer have more than

one well-defined height with respect to the copper surface [141]. Toomes. *et al.*, postulated a significantly different structure in a photoelectron diffraction study of the Cu(111) surface [142]. It was suggested that within the disordered overlayer, Cu atoms reconstruct to form a Cu(100)-like structure with oxygen atoms occupying fourfold hollow sites. The oxygen atoms in the reconstructed overlayer are incommensurate with the underlying un-reconstructed (111) surface.

Although the initial interaction of oxygen with the Cu(111) surface has been studied, in none of these studies has sufficient information been obtained to determine unequivocally the overall kinetics of the reaction process from the chemisorption to oxide formation. It is advantageous to prepare well-ordered flat surfaces in order to gain an understanding of the oxidation occurring on this surface on a nanometer scale. In this study, we investigated the oxidation of Cu(111) at different temperatures. We have examined the dependence of oxide island density, morphology, and coalescence on oxidation temperature and time. It has been found that the oxidation behavior on Cu(111) is dramatically different from Cu(100) and (110) surfaces, and the surface structure of initial oxygen chemisorption can greatly affect the kinetics of oxide nucleation and growth, and the epitaxial oxide growth also affects the surface structure of the O-chemisorbed Cu(111). When the temperature is lower than 550°C, the oxidation is dominated by the rapid oxide island nucleation followed by slow growth, whereas the oxidation at temperatures higher than 550°C is dominated by rapid lateral growth. Therefore, the oxidation of Cu(111) has a transition from island nucleation to almost layer-by-layer growth with increasing oxidation temperature.

6.1 EFFECT OF TEMPERATURE ON OXIDE NUCLEATION AND GROWTH

We first present the systematic investigation of the effect of temperature on the oxidation of Cu(111) at temperatures ranging from 350°C to 700°C.

6.1.1 Oxidation at 350°C

Figure 6.1 is a time sequence of BF TEM images showing the change of oxide island density with oxidation time. The partial pressure of oxygen was 5×10^{-4} torr and the temperature of the

copper film was held at 350°C. Figure 6.1 (a) is the Cu(111) surface which was cleaned with methanol gas. After the introduction of oxygen gas, the nuclei appeared very quickly, followed by growth. Figure 6.1 (b-c) show the corresponding BF images of the same area after oxygen was leaked into the column of the microscope for 2 minutes and 3 minutes, respectively.

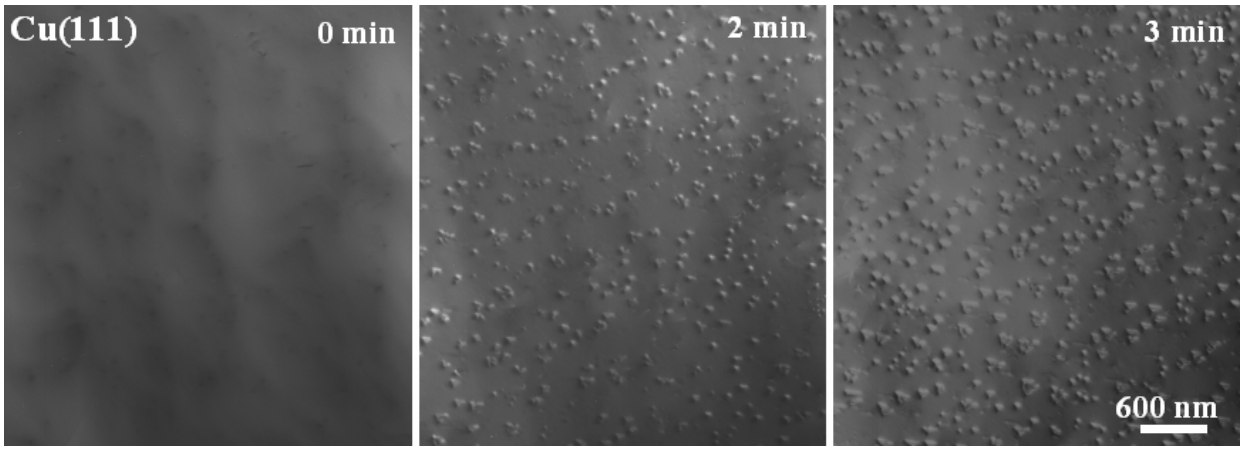

Figure 6.1 *In situ* BF TEM images taken as a function of oxidation time, (a) 0 min, (b) 1 min, (c) 5 min at constant oxygen partial pressure of 5×10^{-4} torr and temperature of 350°C.

Figure 6.2 shows the AFM image of the islands formed at this temperature. The islands have a triangular shape morphology, which is similar to the TEM observation. The surface profile analysis indicates that the range of the island height is 2 ~ 4.5 nm, and the island top is not flat.

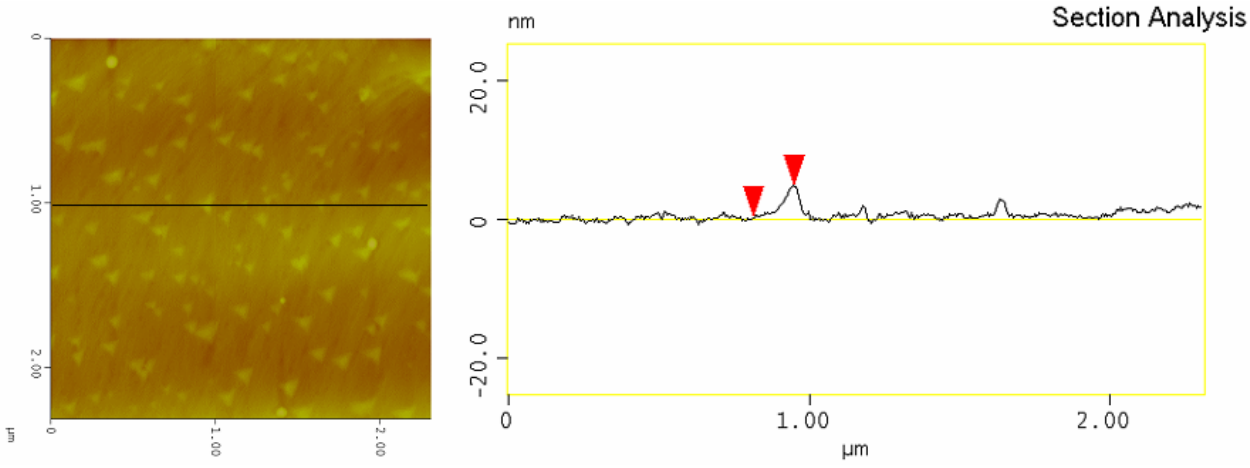

Figure 6.2 AFM image (left) of the oxide islands formed 350C, the surface profile analysis (right) indicates that the islands have tip structure, and the islands with larger lateral size have larger height.

6.1.2 Oxidation at 450°C

Figure 6.3 is a time sequence of BF TEM images showing the change of oxide island density with oxidation time at a temperature of 450°C. The partial pressure of oxygen was 5×10^{-4} torr. The density of oxide islands is less than the oxidation at 350°C. At the very beginning of the oxidation, the oxide islands had a random distribution. But with the continuous oxidation, it is interesting to note that the nucleation of new islands was not random, and the new islands nucleated near the old islands, creating a cluster of oxide islands with an overall triangular shape. The oxide islands grew along $[1\bar{1}0]$Cu to form elongated structures. The rate of this one dimensional growth was ~200nm/min in the first 3 minutes, and then slower with the nucleation of more islands to form the triangular-shaped cluster of oxide islands.

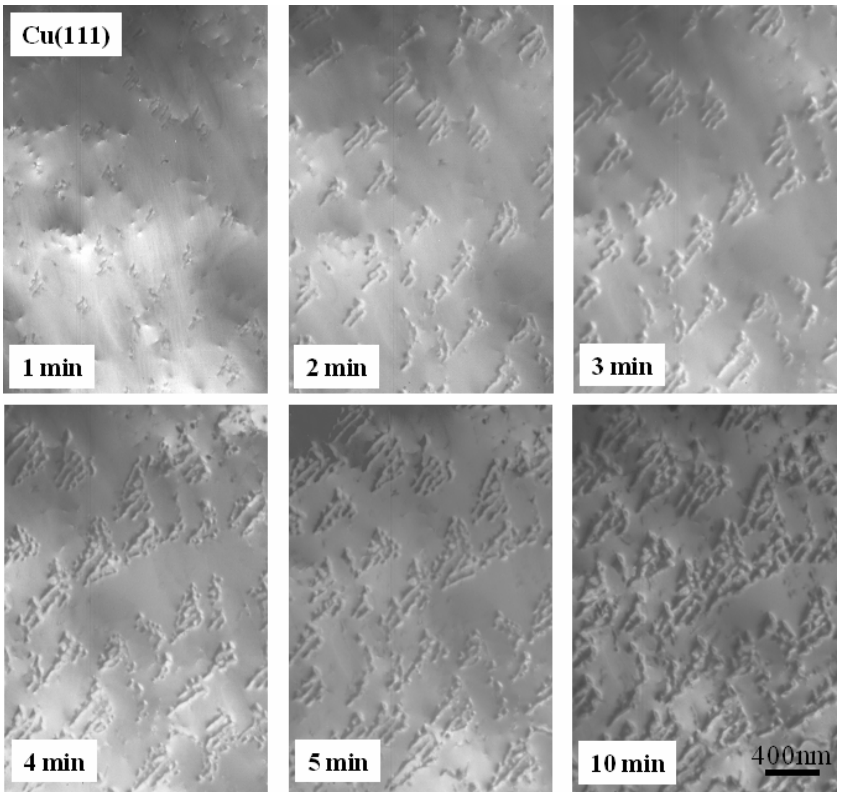

Figure 6.3 *In situ* BF TEM images taken as a function of oxidation time at constant oxygen partial pressure of 5×10^{-4} torr and temperature of 450°C, where the oxide islands had a elongated structure by growing along $[1\bar{1}0]$ on Cu(111) surface with the continuous oxidation.

6.1.3 Oxidation at 550°C

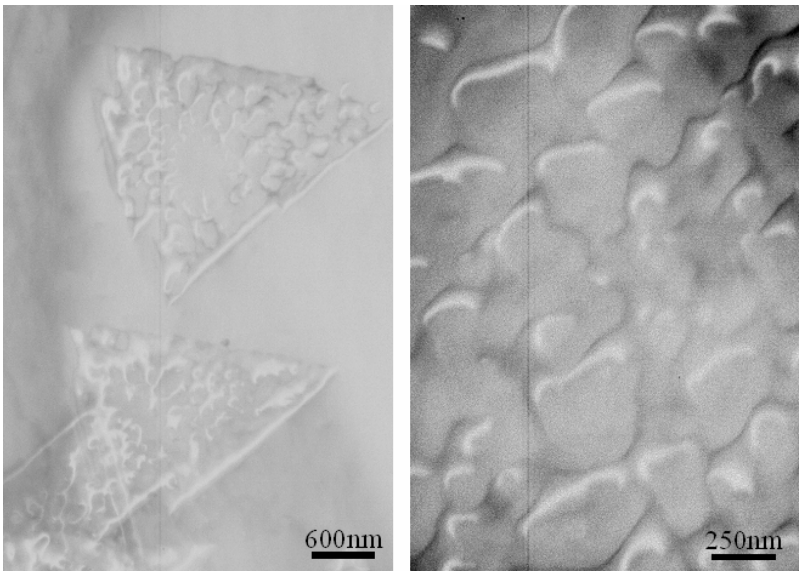

Figure 6.4 (a) Oxide islands oxidized at constant oxygen partial pressure of 5×10^{-4} torr and temperature of 500°C after 6 min oxidation; (b) the enlarged picture from (a).

The oxidation behavior at 550°C was dramatically different than that at lower temperatures. The exposure of Cu(111) resulted in rapid formation of the copper oxide followed by fast lateral growth of the oxide, which appeared similar to the two dimensional development of a discontinuous oxide layer. Figure 6.4 (a) shows the general morphology of oxide formed at this temperature and oxygen partial pressure of 5×10^{-4} torr. The overall morphology of the oxide was a triangular shape, however, the oxide layer is discontinuous and has a disordered "network" structure inside the oxide. Figure 6.4 (b) is the enlarged picture from the inside of the oxide, which reveals that the disordered oxide does not have definite facet structures within the discontinuous areas. The initially formed oxide layer evolved laterally, and formed a highly discontinuous Cu_2O film, but finally formed a continuous perimeter that is triangular and faceted. The density of the oxide islands formed at this temperature was much smaller than that at the lower temperatures, and the oxide has a much faster growth rate and appears more like a discontinuous oxide "layer" than an island.

Figure 6.5 is an AFM image from the inside of the oxide formed at this temperature. Again, the image indicates that the oxide layer is discontinuous with a disordered distribution of oxide

"droplets" in the oxide layer. The surface profile indicates that oxide "droplets" have a height range of 10~14 nm, and most of them have a flat top as shown in the right side of Figure 6.5.

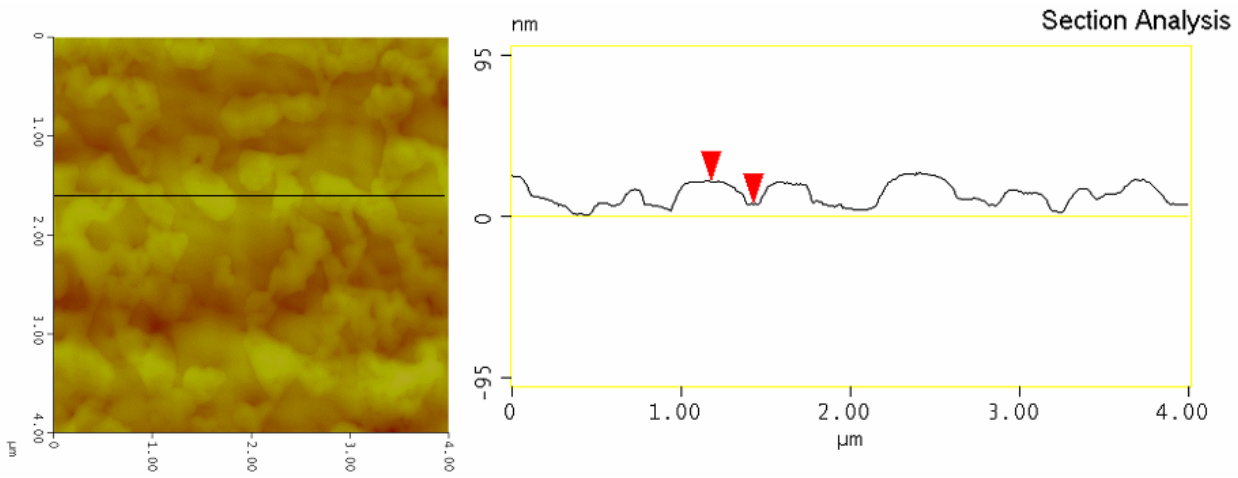

Figure 6.5 AFM image (left) from the inside of the discontinuous oxide layer, the surface profile (right) of the oxide layer indicates that oxide droplets have a flat top and height range of 10~14 nm.

6.1.4 Oxidation at 600°C

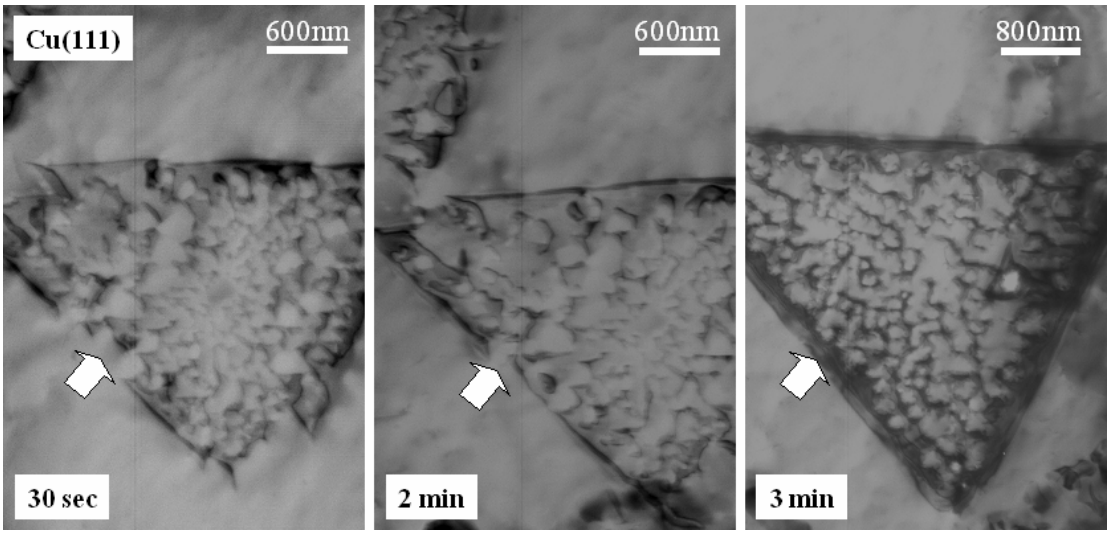

Figure 6.6 *In situ* BF TEM images taken as a function of oxidation time, (a) 30 sec, (b) 2 min, (c) 3 min at constant oxygen partial pressure of 5×10^{-5} torr and temperature of 600°C.

The oxidation at this temperature was similar to that at 550°C — rapid formation of oxide followed by the fast lateral growth, where the oxide layer had a discontinuous structure. Figure 6.6 shows the *in situ* observation of the growth of one island. In Figure 6.6 (a), the oxide had a discontinuous layer structure with a triangular perimeter. The arrow points to where the triangular perimeter of Cu_2O layer was not well developed. With continued oxidation, Cu_2O grew laterally and the triangular perimeter developed into a continuous structure as shown in Figure 6.6 (b, c).

6.1.5 Oxidation at 700°C

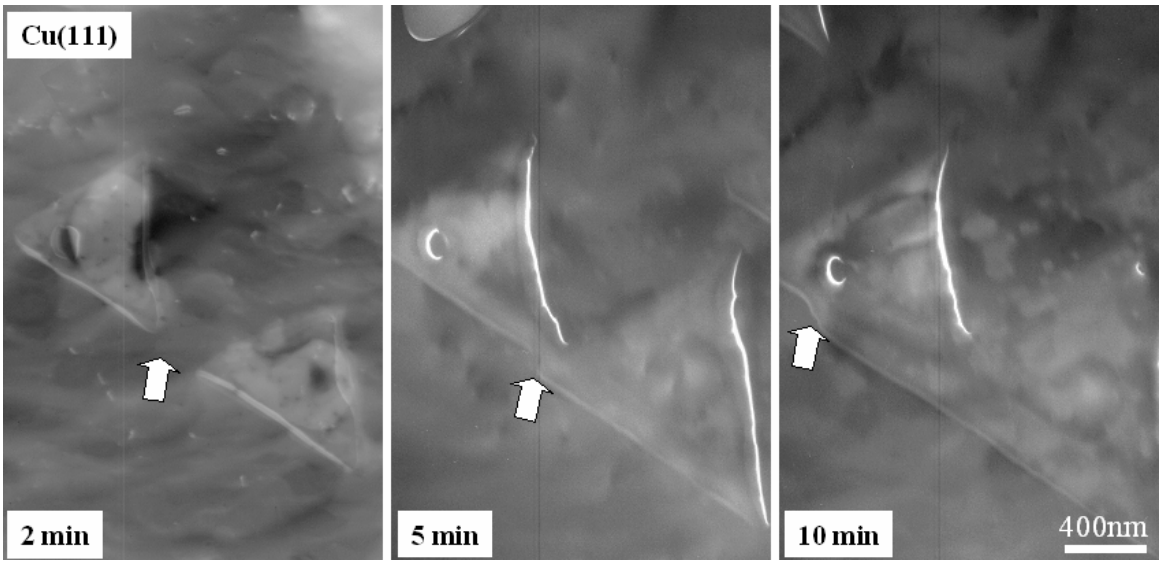

Figure 6.7 *In situ* BF TEM images taken as a function of oxidation time, (a) 2 min, (b) 5 min, (c) 10 min at constant oxygen partial pressure of 5×10^{-5} torr and temperature of 700°C.

The structure of the oxide islands formed at this temperature is different from that at the lower temperatures we have investigated. The oxide had a triangular perimeter with continuous film structure and appeared almost similar to a "layer-by-layer" growth. The AFM investigation indicates that thickness of the oxide formed at this temperature is similar as that formed at 600°C. Figure 6.7 shows the *in situ* observation of the morphology evolution of the oxide islands formed at this temperature. Figure 6.7 (a) shows two separate oxide islands with continuous film

structure (with the exception of a small hole in one island). With continued oxidation, coalescence occurs between these two islands, as shown in Figure 6.7 (b). A kink formed after the coalescence of the islands, as indicated by the arrow. Figure 6.7 (c) shows that the kink moved to the island corner along the island edge during the further growth of these two oxides. No grain boundary structure was found between the two islands, which indicates that there is a perfect merging of the two islands. The coalescence behavior of islands on Cu(111) is different from Cu(100). In the oxidation of the Cu(100) surface, a neck structure between the two oxide islands formed first just prior to coalescence.

6.2 THE EPITAXIAL GROWTH OF THE OXIDE ISLANDS ON Cu(111)

The oxidation of Cu(100) and (110) surfaces resulted in the epitaxial growth of Cu_2O islands. Similarly, the *in situ* oxidation of Cu(111) surfaces also resulted in the epitaxial Cu_2O formation.

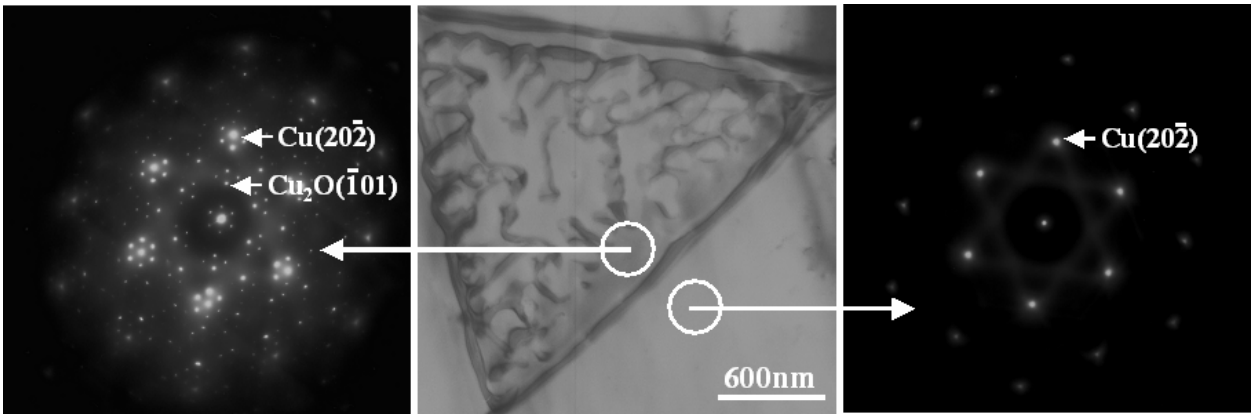

Figure 6.8 (a) Selected area electron diffraction pattern (SAED) from the (111)Cu film; (b) SAED pattern from Cu_2O/(111)Cu film, where the additional spots are due to double diffraction.

Figure 6.8 shows the diffraction patterns taken from the oxidized Cu(111) film, where the sample was first oxidized at 600°C and an oxygen pressure of 5×10^{-4} torr. Figure 6.8 (a) is an SAED pattern from the Cu surface near the oxide. Figur 6.8 (b) is the diffraction pattern from the area with oxide as shown in the figure, where the oxide has the Cu_2O structure and is epitaxial

with the underlying Cu substrate, i.e., $Cu_2O(111)//Cu(111)$ and $Cu_2O\left(20\bar{2}\right)//Cu\left(20\bar{2}\right)$, as shown in Figure 6.8 (b). Additional spots due to double diffraction between the Cu_2O and the Cu film also appear in the pattern.

By measuring the spacings from the diffraction patterns, it is interesting to note the lattice spacing of Cu near the oxide is different from the Cu under Cu_2O. The spacing of Cu(220) of the Cu film near the oxide is 1.29Å, which is larger than the bulk value, 1.276Å. However; the Cu(220) spacing under the Cu_2O layer is reduced to 1.258Å, which is not only smaller than the spacing in the bare Cu region, but also the bulk Cu value. The Cu_2O layer also has a smaller (220) spacing than its bulk value. The lattice parameters of Cu and Cu_2O and their comparison to the bulk values are shown in Table 6.1.

Table 6.1 The lattice parameters of Cu and Cu_2O and the comparison to their bulk values.

	Cu film near oxide	Cu_2O-Cu(111) region	bulk value
Cu (Å)	3.65±0.02	3.56 ±0.02	3.61
Cu_2O (Å)		4.15 ±0.02	4.22

Table 6.1 indicates that the Cu lattice in the Cu_2O-Cu region has a ~2.5% decrease as compared to the Cu film near the oxide, and the lattice of the epitaxially grown Cu_2O has a ~1.7% compression from its bulk value. Matthews proposed that large misfit systems may be interpreted in terms of the lattice coincidence model [143]. According to this theory, the bilayer would be in a local minimum energy state and is said to be in perfect coincidence if the m^{th} atom of the overgrowth coincides with the n^{th} atom of the substrate surface layer, where $n=m \pm 1$. If ma_o and na_s are not exactly equal, the system would have a coincidence misfit defined as

$$f = -\left(ma_o - na_s\right)/ma_o \tag{6.1}$$

where a_o and a_s are the lattice constants for the overgrowth and substrate, respectively. For the Cu_2O-Cu system, $6\,a_{Cu_2O}$ are almost equal to $7a_{Cu}$, and hence the Cu_2O/Cu bilayer have a coincidence misfit of f = -1.22% [133]. According to the epitaxial relationship between Cu_2O and Cu as shown in Figure 6.8, the coincidence misfit is 0.08%, which is much smaller than the reported data [133]. Therefore, the epitaxial growth of Cu_2O on Cu(111) has a nearly perfect 6 to

7 coincident lattice by having ~1.4% compressive strain in the underlying Cu lattice and 1.7% compressive strain in Cu_2O lattice from their unstrained states. Figure 6.9 shows the schematic illustration of the overgrowth of Cu_2O on Cu(111) by the coincidence lattice misfit of 0.08% such that three times the oxide periodicity is equal to seven times that of the Cu substrate. Equivalently six Cu atom spacings in the oxide equal seven Cu atoms in the substrate.

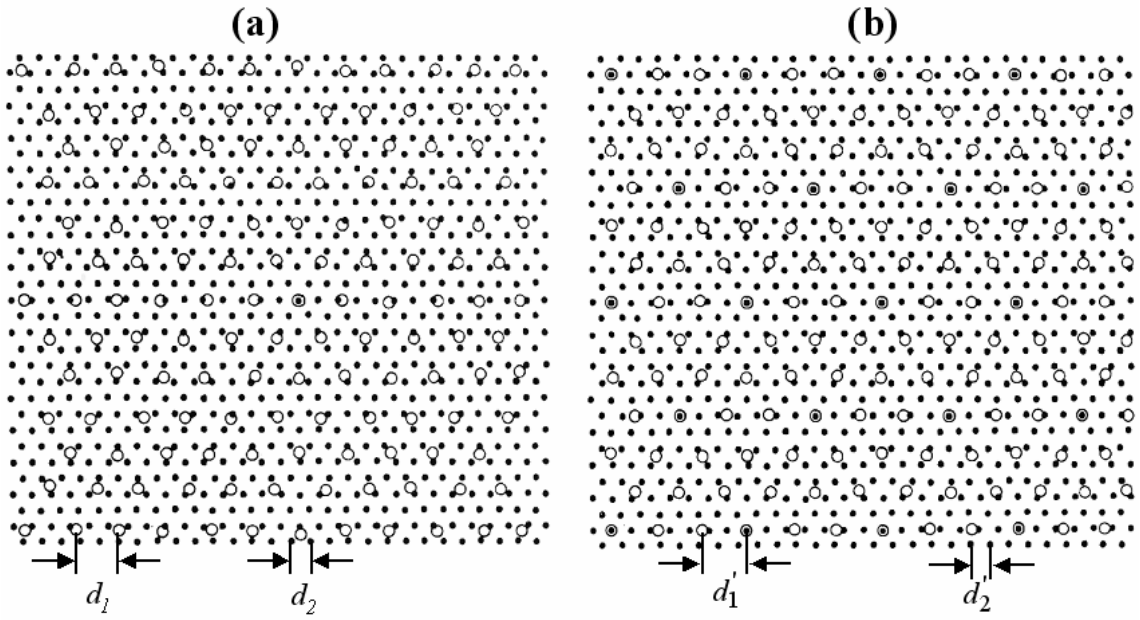

Figure 6.9 (a) Cu atoms in the substrate (•), and Cu_2O (O) periodicities at (111) interface plane for unstrained lattices; (b) Cu atoms (•) and Cu_2O (O) periodicities by the coincidence lattice misfit of 0.08% to assume a superlattice structure which has a periodicity of 3 times that of the oxide. $d_1' = 0.986\, d_1$, $d_2' = 0.983 d_2$.

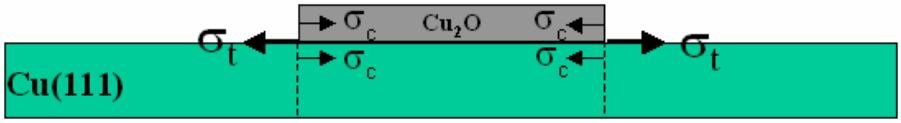

Figure 6.10 The force balance for atoms on the oxide island edge, where compressive stress in the oxide and the underlying Cu substrate is balanced by the tensile stress in the Cu film next to the island.

One question relates to the force balance for the occurrence of the compressive strain in both the oxide layer and the underlying Cu substrate. As shown in Table 6.1, the lattice of the Cu film near the oxide island has a lattice expansion from its bulk value. This tensile strain caused by the compressive strain in the Cu film under the epitaxial Cu_2O layer can balance the compressive stress in the oxide and the underlying Cu substrate as shown in Figure 6.10. The distribution of the compressive and tensile strain in the Cu film is determined by the position and morphology of the oxide islands. Figure 6.11 shows the schematics of the distribution of compressive and tensile strain in the Cu film.

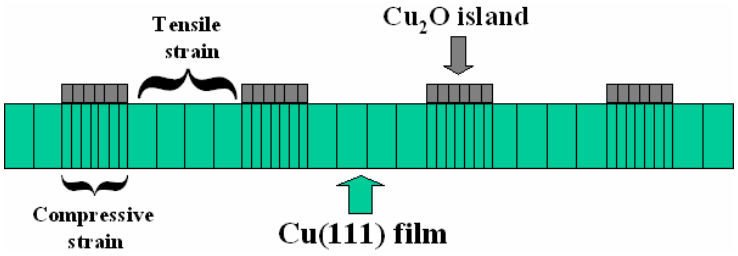

Figure 6.11 Schematics of the distribution of compressive and tensile strain in Cu(111) film, where the oxide islands have a shallow penetration into the Cu film, the oxide islands and the Cu film underneath the oxide islands have compressive strain, which cause tensile strain the Cu film near the oxide islands.

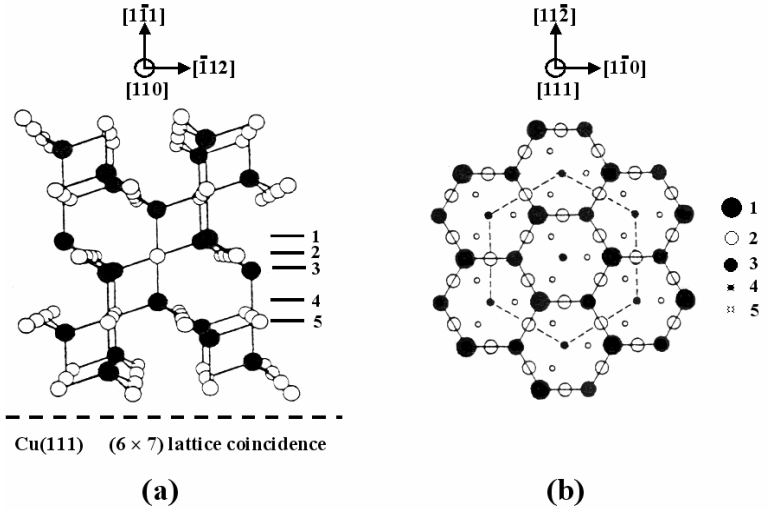

Figure 6.12 Structure of Cu_2O, the oxygen and copper atoms are represented by filled (•) and open (O) circles, respectively. (a) Side view of the atomic model Cu_2O attached to the Cu(111) substrate; (b) the top view of (111) projection of the five marked planes in (a).

6.3 GROWTH DIRECTIONS OF THE OXIDE ISLANDS

In order to understand the epitaxial growth of the oxide islands on Cu(111), the structure of Cu_2O is shown in Figure 6.12. The structure has close-packing of Cu ions with O ions in two tetrahedral sites. Figure 6.12 (a) is the side view of the Cu_2O structure, the [111] axis of Cu_2O is parallel with [111] axis of Cu substrate, and $Cu_2O(10\bar{1})$ is parallel with $Cu(10\bar{1})$. At the Cu_2O(111)-Cu(111) interface, they have 6×7 lattice coincidence, as inferred from the analysis of the electron diffraction patterns.

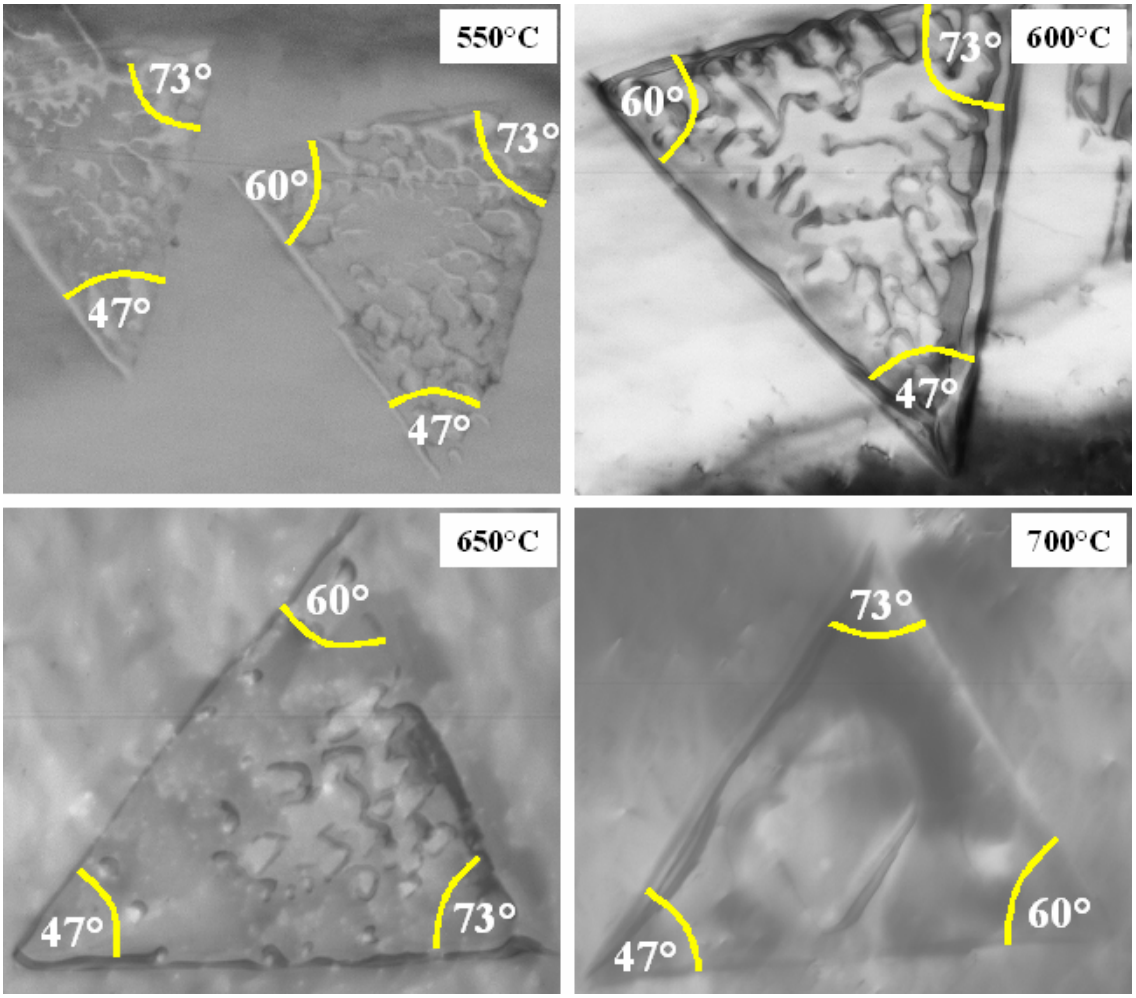

Figure 6.13 The angles of the oxide islands formed at the different temperatures.

It is known that oxide islands formed on Cu(111) surfaces at the different temperatures have triangular shape. In order to determine the growth direction of the oxide islands, the angles of the oxide islands were measured and are presented in Figure 6.13, which shows that all the islands have the angle set of 73°, 60° and 47°. Since the oxide islands are epitaxial with the Cu(111) substrate, i.e., $Cu_2O(111)//Cu(111)$, and $Cu_2O(10\bar{1})//Cu(10\bar{1})$. From this relationship, the growth direction of Cu_2O islands on Cu(111) surface is determined and is shown in Figure 6.14.

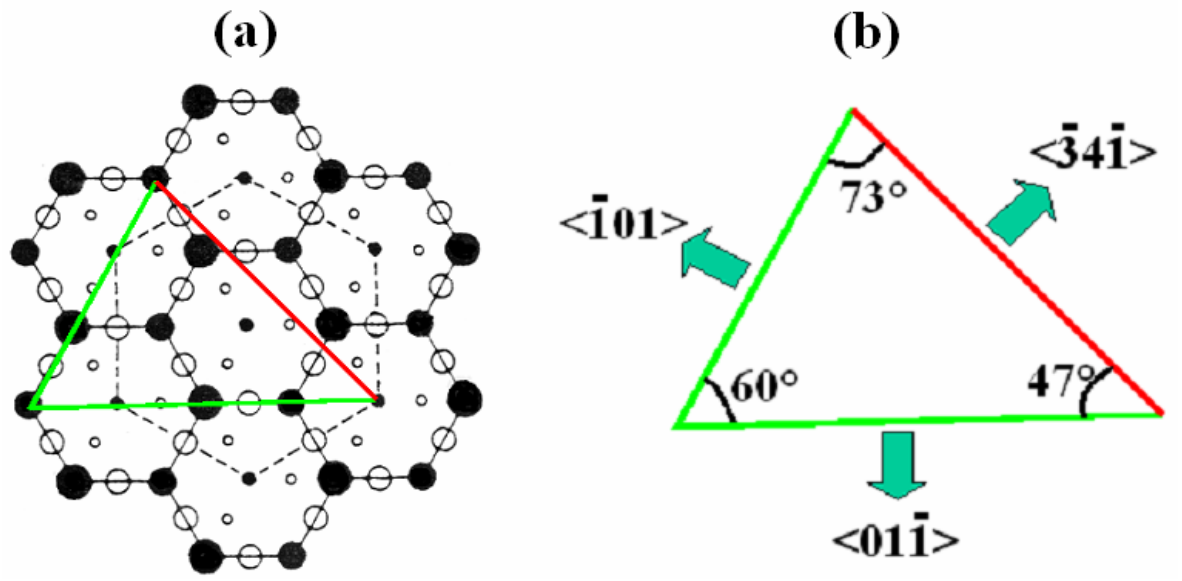

Figure 6.14 The projection of Cu_2O along its [111] axis, and the crystalline angles and growth directions of the oxide islands.

The formation of oxide islands with the triangular shape on the Cu(111) surface was also observed in the earlier investigation and the growth direction of oxide islands was assumed to be {110} [133]. The present results indicate that only two directions of the triangular islands are along [110], the other one is a high index direction, $<\bar{3}4\bar{1}>$. {110} directions are the closest-packing rows on the (111) plane, and have the fastest growth rate. Figure 6.15 shows that the $<\bar{3}4\bar{1}>$ growth direction can be considered as composed of $<\bar{1}10>$ and $<01\bar{1}>$, which gives rise to the fast growth along this direction.

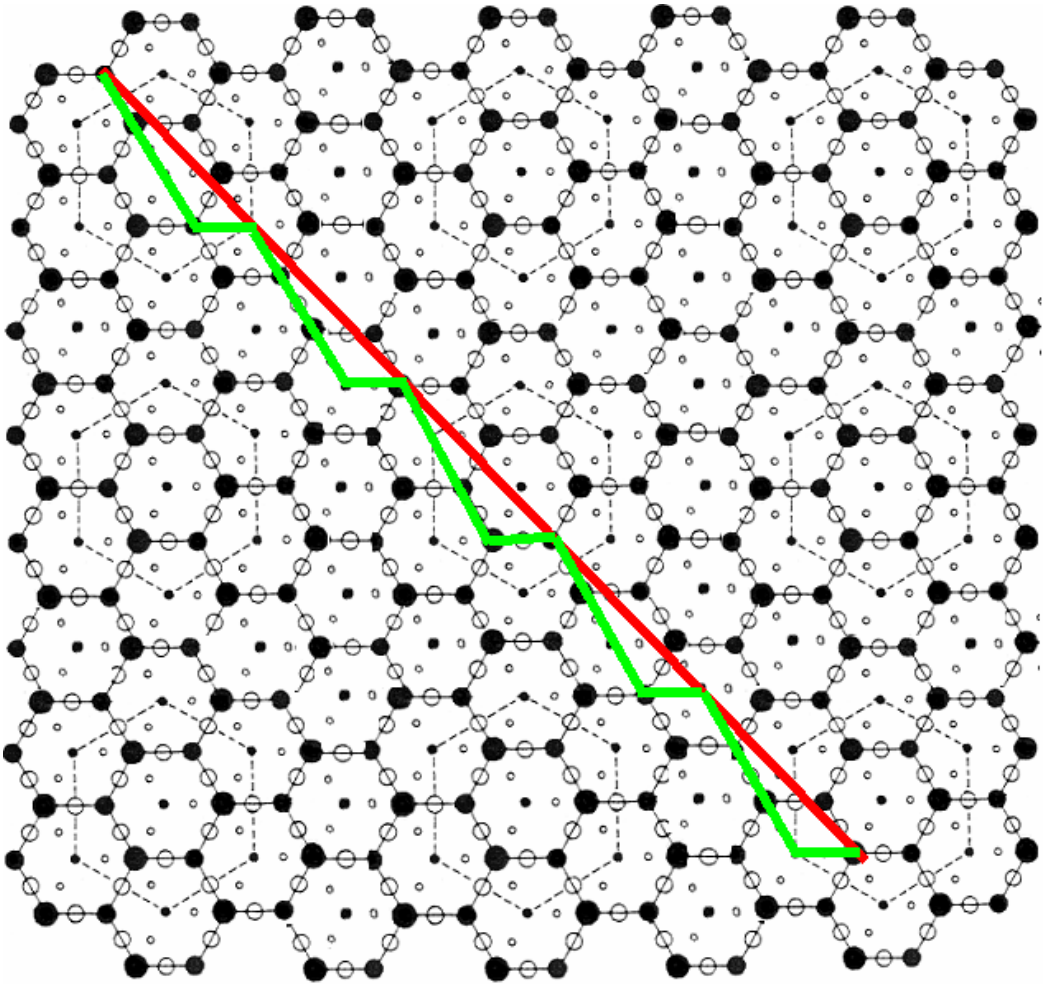

Figure 6.15 The projection of Cu_2O along its [111] axis, the growth directions of $<\bar{3}4\bar{1}>$ can be considered as composed of steps of $<\bar{1}10>$ and $<01\bar{1}>$.

6.4 DISCUSSION

Before discussing the effects of temperature on the oxidation of Cu(111), we first compare the nucleation and growth rates of oxide islands on Cu(111) at the different oxidation temperatures. Table 6.2 shows their comparison in the oxidation of the first 5 minutes. The oxidation in the temperature range of 350°C-450°C followed the similar process of nucleation and growth of oxide islands. But the oxidation at 550°C and higher temperatures resulted in the very fast

"droplet" or layered oxide growth and the formation of the oxide did not follow the "islanding" process. Therefore, the "island density" at these temperatures loses its meaning, and no island density and nucleation rate were listed in Table 6.2 in the temperature range of 550°C-700°C. The growth rate of the oxide increased with increasing oxidation temperature. One exception was that the oxide formed at 700°C had a slower growth rate than that at 550°C and 600°C.

Table 6.2 The comparison of oxidation kinetics of Cu(111) at the different temperatures

	350°C	450°C	550°C	600°C	700°C
island density (μm^{-2})	6.13	3.7			
nucleation rate ($\mu m^{-2}min^{-1}$)	2.05	1.23			
growth rate (nm^2/min)	1.17×10^3	7.22×10^3	1.36×10^7	2.61×10^7	1.1×10^6

6.4.1 Effect of temperature on the oxide nucleation

The oxidation in the temperature range of 350~450°C had two obvious features — the high number density and the fast nucleation rate of the oxide islands. As introduced previously, the O-chemisorption on Cu(111) causes a disordered surface overlayer at room temperature, in which oxygen atoms have more than one well-defined height with respect to the Cu surface [141]. As temperature increases to 200-350ºC, the chemisorption of oxygen on Cu(111) results in ordered '29'-$\left(\sqrt{13}R46.1^\circ\times 7R21.8^\circ\right)$ and '44'-$\left(\sqrt{73}R5.8^\circ\times\sqrt{21}R-10.9^\circ\right)$ lattice structures [1, 9, 12, 144, 145]. These structures comprise distorted hexagonal arrays of O atoms arranged in parallel lines in the first layer, with the unit cell areas 29 and 44 times larger than those of the substrate Cu(111), which appears strikingly similar to the (111)Cu_2O structure. Both chemisorbed oxygen layers were considered to be analogous to the planes of the Cu_2O(111) which has a structure with equilateral hexagons of oxygen atoms in the first layer. Therefore, the reconstructed Cu{111} surface is almost a template for the Cu_2O {111} structure, which facilitates the nucleation of the Cu_2O structure and gives rise to a fast initial nucleation rate of oxide islands.

The oxidation in the temperature range of 550ºC-700ºC resulted in a very fast oxide island growth process with no obvious nucleation of an "island". As we have discussed in the oxidation of Cu(100) and Cu(110), the oxidation goes through the similar sequence of nucleation and growth of 3D oxide islands. A number of fundamental aspects of the growth of 3D islands in heteroepitaxy is now well documented [25, 28, 146]. The heteroepitaxial theories typically assume that misfit strain drives the formation of the 3D epitaxial islands. The elastic energy of the initially planar, strained, layer increases with growing film thickness, until the system can lower its free energy by nucleating faceted 3D islands, thus relaxing part of the misfit strain at the expense of somewhat increased surface energy. Minimizing the total free energy (surface and interface free energy and relaxation of the lattice-mismatch caused strain energy) of a strained island gives an activation energy barrier for the formation of a 3D island, and this barrier scales with lattice misfit f as f^4. [147]. Therefore, the lattice misfit plays a prominent role in determining the mode of growth. The larger the misfit, the greater is the tendency towards island-like growth, and vice versa (layer-by-layer growth). On the other hand, the crystallographic orientation of the substrate also affects the mechanism of growth. The more densely packed the substrate plane, the greater the tendency towards layerlike growth in comparison with the less densely packed planes. In particular, this tendency is expressed by the fact that the more densely packed the substrate planes are, the flatter the 3D crystallites will grow [88].

It is known that Cu_2O has a thermal expansion coefficient of 1.9×10^{-6} °C^{-1}, and Cu has a thermal expansion coefficient of 17×10^{-6} °C^{-1}. With increasing temperature, the lattice mismatch between Cu and Cu_2O becomes smaller. When the oxidation temperature exceeds 550°C, there will be a low misfit on the Cu/Cu_2O (111) interface, as demonstrated from the electron diffraction investigation where the coincidence lattice misfit was found to be only ~0.08%. Therefore, Cu(111) forms an ideal template for layer-by-layer growth of Cu_2O without the "islanding" process at these temperatures. In comparison with Cu(100) and Cu(110), Cu(111) surface also provides a substrate with the most densely packed planes which facilitates the layer-by-layer growth of the oxide.

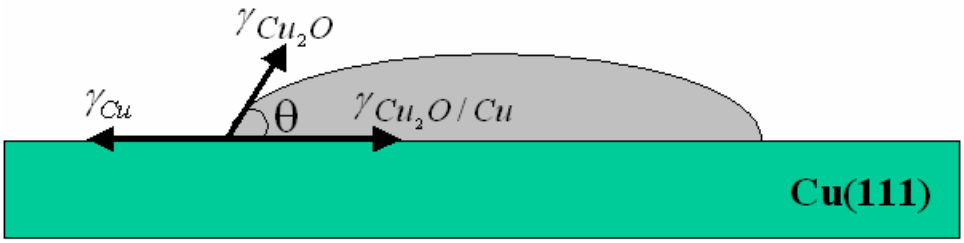

Figure 6.16 Schematics of the mechanical equilibrium between surface energies and interfacial energy

According to capillarity theory, the contact angle, θ, between the epitaxial film and substrate is related to the surface/interface energies of the film and substrate. From the mechanical equilibrium on the substrate surface, the contact angle θ between the oxide layer and Cu substrate can be determined to be

$$\cos\theta = \frac{\gamma_{Cu} - \gamma_{Cu/Cu_2O}}{\gamma_{Cu_2O}} \tag{6.2}$$

where the parameters are defined in Figure 6.16. This relationship can be used to estimate, roughly, the interface energy by measuring the contact angles. Assuming the simplest situation, $\gamma_{Cu} = \gamma_{Cu_2O}$, the formation of a complete wetting oxide layer, (θ=0), will have $\gamma_{Cu/Cu_2O} = 0$. Therefore, if the interface energy is small, the contact angle, θ, will be small, also. AFM measurements indicate that the oxide layer has a flat top and the contact angle between the oxide layer and Cu(111) substrate varies from 1° to 5°, indicative of the very small interfacial energy compared to the surface energies. Therefore, the oxidation of Cu(111) at 550°C and the higher temperatures had a layer-by-layer growth mode of the oxide due to the decreased interface strain energy between the oxide layer and Cu(111) substrate. As we have introduced previously, the oxidation of Cu(100) and Cu(110) results in the formation oxide islands, and the contact angles between the side facets of the islands and substrate are usually larger than 25°, which is much larger than the Cu(111) case, indicative of the larger interface energy in Cu_2O/Cu(100) and Cu_2O/Cu(100).

6.4.2 Effect of temperature on the oxide growth

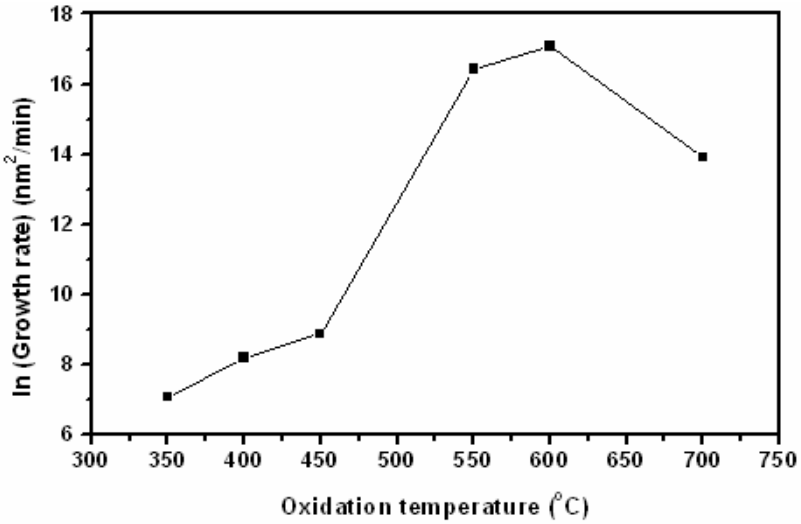

Figure 6.17 The growth rate of the oxide islands in the first 5 minutes of oxidation at the different temperatures, it is noted that the oxidation at 700ºC shows a slower growth rate of the oxide islands than 550ºC and 650ºC.

The general trend of the growth rate (increase of cross-sectional area of the islands per minute) of the oxide islands is that it increases with increasing temperature, as shown in Figure 6.17. Since at the high temperatures the surface diffusion of oxygen is enhanced, the oxygen atoms are more likely to be captured by existing islands, which causes the island growth, rather than the nucleation of new oxide islands. Especially when the oxidation temperature exceeded 550ºC, the growth rate of the oxide layer was faster than at the lower temperatures by a factor of ~10^4. Again, this dramatic increase in growth rate of the oxide islands may be related to the low misfit between Cu and Cu_2O which occurred at this temperature, where the Cu(111) surface provides an ideal template for oxide growth.

However, it is noted that there is an exception from this increased trend of the growth rate of the oxide islands. The growth rate of the islands at 700ºC was decreased by approximately an order of magnitude as compared with that at 600ºC. This exception of the growth rate can be easily understood by considering the different structures of the oxide islands formed at the different temperatures. The investigation of the morphology of the islands shows that the islands

formed at 700ºC had an almost continuous film structure (Figure 6.7). However, the oxide islands formed at 550ºC and 600ºC had a discontinuous film structure (Figure 6.6). Obviously, the oxide layer with the continuous structure has more Cu_2O per unit area than the discontinuous structure by considering the similar thickness of the oxide layer formed in the temperature range of 550°C~700°C. Therefore, it will take more time for the oxide layer with the continuous structure than for the islands with discontinuous structure to grow to the same size, even at a higher temperature.

An important feature for Cu(111) oxidation is that the oxidation on this surface resulted in the formation of a discontinuous oxide layer in the temperature range of 550-650ºC. This discontinuous oxide layer developed a triangular shaped perimeter as shown in Figure 6.4 and Figure 6.6. Earlier studies have demonstrated that disordered O/Cu(111) surface forms by room-temperature adsorption of O_2 on clean Cu(111) [1, 9, 12, 144, 145] and this disordered surface can be converted into ordered '29' and '44' surface structure domains by annealing at ~550ºC. The formation of a discontinuous oxide layer on Cu(111) may be related to these ordered and disordered domain structures of O-Cu(111). As shown in Figure 6.4 and Figure 6.6, we speculate that the regions having Cu_2O oxide could have '29' or '44' ordered surface structures, whereas the discontinuous regions could be associated with the disordered surface structure. Further surface analysis is needed to confirm this.

The oxidation at 700ºC resulted in the almost continuous oxide layer structure with very few and small holes in the oxide layer, as shown in Figure 6.7. Again, the formation of this continuous oxide layer may be related to the change of strain between Cu_2O and the Cu(111) surface at 700°C. At the elevated temperature, the interface strain energy is decreased; as a result, the interface energy, composed of the chemical energy due to the interfacial bonding and strain energy, is also decreased. Therefore, the contact angle will decrease even further at the elevated temperature, leading to an almost "layer-by-layer" growth. Also, the formation of a continuous oxide layer at 700°C suggests that the Cu(111) surface at this temperature has an almost continuous ordered oxygen chemisorbed layer which provides a perfect template for the formation of a continuous oxide layer.

6.4.3 Comparison to the oxidation of Cu(100) and Cu(110)

The comparison of oxidation of Cu(100), (110) and (111) may provide important information regarding the effects of surface structure on the oxidation mechanism. Table 6.3 shows the comparison of the nucleation and growth rate of oxide islands on Cu(100), (110) and (111) at 350ºC and 5×10^{-4} torr oxygen pressure. Cu(111) shows the fastest nucleation and growth rate of oxide islands among these three surfaces.

Many investigations have elegantly demonstrated that metal surfaces experience a reconstruction due to the oxygen chemisorption. Oxygen chemisorption on Cu(100) and Cu(110) results in restructuring of a surface with $\left(\sqrt{2}\times2\sqrt{2}\right)$R45º O-Cu(100) and (2×1) O-Cu(110) surface structures [2-6]. The $\left(\sqrt{2}\times2\sqrt{2}\right)$R45º O-Cu(100) has a more compact oxygen chemisorption than (2×1)O-Cu(110) surface which has a corrugated structure (see Figure 5.6). Therefore, the activation barrier for surface diffusion of oxygen could be higher on the Cu(110) surface than the Cu(100). This smaller coefficient of oxygen surface diffusion results in a smaller capture zone of oxygen and creates a higher number density of oxide nuclei on Cu(110) than Cu(100). Furthermore, the "corrugated" Cu(110) surface could provide more preferential nucleation sites than Cu(100), and thereby lead to greater island density.

Table 6.3 Comparison of the oxidation on Cu(100), (110) and (111) at 350ºC and 5×10^{-4} torr oxygen pressure.

	Cu(100)	Cu(110)	Cu(111)
nucleation rate ($\mu m^{-2}min^{-1}$)	0.1	1.22	2.05
growth rate (nm^2/min)	6.7×10^2	7.0×10^2	1.17×10^3

The oxygen adsorption on (111) at 350ºC results in the adlayer domains with ordered '29'-$\left(\sqrt{13}R46.1^\circ\times7R21.8^\circ\right)$ and '44'-$\left(\sqrt{73}R5.8^\circ\times\sqrt{21}R-10.9^\circ\right)$ lattice structures comprising distorted hexagonal arrays of O atoms which were considered to be analogous to the planes of $Cu_2O(111)$ which has a structure with equilateral hexagons of oxygen atoms in the first layer [1,

9, 12, 144, 145]. Therefore, the reconstructed Cu{111} surface is almost a template for the Cu_2O {111} structure, and will easily facilitate the nucleation and growth of the oxide islands as compared to that on the other two surfaces. As a result, Cu(111) exhibits a faster nucleation and growth rate compared with Cu(100) and Cu(110).

6.4.4 Impact to the passivation property of copper surfaces

As we discussed earlier, the orientation with faster initial oxidation rate will have a faster coalescence of the oxide islands, which switch the fast surface diffusion of oxygen to slow bulk diffusion. Therefore, the oxide islands formed on the orientation with the fast initial oxidation rate coalescence prior to a passivation oxide layer, and then the bulk oxidation rate slows down. This thought explained the different initial and bulk oxidation rate of Cu(100) and Cu(110) as introduced in the chapter of Cu(110) oxidation.

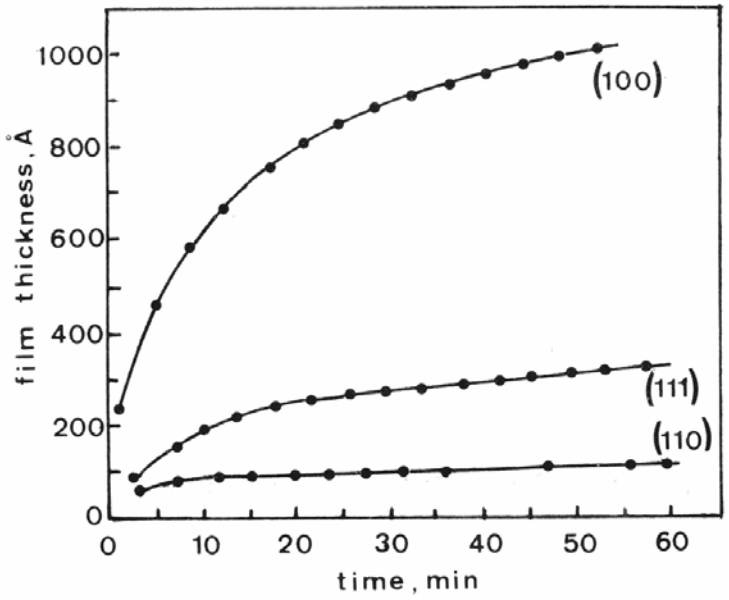

Figure 6.18 The passivation properties of copper single crystals at 523K and 1 atm of oxygen pressure (see reference [52])

The Cu(111) surface shows the fastest initial oxidation rate (nucleation rate and growth rate of the cross-sectional area of the oxide islands) as compared with the Cu(100), (110) oxidation. Therefore, Cu(111) will be expected to have the slowest bulk oxidation rate compared with

Cu(100) and Cu(110). However, Lawless and Gwathmey's work indicates that Cu(111) has a faster bulk oxidation rate than Cu(110), as shown in Figure 6.18. This difference can be explained by the different oxide thickness formed on Cu(110) and Cu(111). The AFM investigation indicates that the oxide islands formed on Cu(111) have a thickness of ~ 5nm on a Cu surface, while the oxide islands formed on Cu(110) have a thickness of ~ 25 nm on a Cu surface. The oxide layer formed on the Cu(111) is much thinner than that formed on the Cu(110), although there is a faster coalescence of the oxide islands on the Cu(111) surface due to its faster initial oxidation rate. The thickness of the oxide layer will affect the rate of the bulk diffusion, and, therefore, the passivation properties. Usually, the oxide layer with thin thickness will have a faster bulk diffusion rate, i.e., poor passivation property. Thus, this different thickness of the oxide formed on the Cu(110) and the Cu(111) during the initial stages of oxidation may explain their different bulk oxidation rate. Since the Cu(111) has a thinner thickness of the oxide layer than the Cu(110), there will be a faster bulk diffusion rate in the later stages of oxidation, which gives rise to the poor passivation property as shown in Figure 6.18.

6.5 CONCLUSIONS

The effects of temperature on the kinetics of the Cu(111) oxidation were investigated. Nucleation and growth of oxide islands dominates the oxidation processes at temperatures lower than 500°C, while the growth of oxide approaches a layer-by-layer growth at higher temperatures. The oxide formed at ~600°C has a discontinuous layer structure and the oxide formed at ~700°C has a more continuous layer structure. The rapid nucleation and growth of Cu_2O on the Cu(111) is explained by the surface reconstruction of the Cu(111) that forms an ideal template for the (111)Cu_2O. The change of the oxide structure is explained by the decreasing interfacial lattice strain with increasing temperature. As temperature increases, the interfacial strain and interfacial energy decreases; therefore, the contact angle between the Cu and the Cu_2O layer decreases, leading to the "layer" growth at the high temperatures. The Cu_2O on the Cu(111) has a nearly perfect 6 to 7 lattice coincidence due to the ~1.4% compressive strain in the underlying Cu and 1.7% compressive strain in the Cu_2O lattices as compared to their unstrained states. The

compressive strain in the Cu film under the oxide layer causes ~1.1% tensile strain in the Cu film near the oxide layer.

7.0 STABILITY OF OXIDE ISLAND NANOSTRUCTURES

We investigated the thermodynamic stability of oxide islands, created by nano-oxidation of metal surface, at different oxygen pressures and temperatures. The *in situ* UHV-TEM has been used to observe the dynamic reduction process of Cu_2O islands on the Cu(100) surfaces. The energetics analysis of the oxide reduction indicates that oxide islands have a higher oxygen dissociation pressure than bulk oxide. The kinetics analysis indicates that the reduction of the oxide islands is a surface controlled decomposition process. The reduction of the oxide island arrays present an effective way to create nano-indentation arrays on surfaces.

7.1 INTRODUCTION

The dynamic observation of the nucleation/growth of oxide islands revealed that completely different oxide structures (disks, nanorods, container pyramids, disordered networks, continuous layer, etc.) can be obtained by simply altering the oxidation temperature and substrate orientation. Oxidation is a reversible process and oxides can decompose at high temperature. Fundamental understanding of the stability of the oxide island arrays provides key insights needed for important advances in a variety of technologies where nano-oxide structures are essential for their potentially novel properties, such as optical, magnetic and sensor.

Generally, a phase diagram of the metal-oxygen system is not enough to explain the behavior of the nano-oxides, because the phase equilibrium of nano-oxides on the metal surfaces is different from that of the bulk oxides. The nano-oxide has large surface/interface to volume ratio, and the interface free energies ($\sigma_{metal\text{-}oxide} + \sigma_{oxide\text{-}vapor}$) can influence the phase equilibria. We have investigated the stability of the oxide islands at different oxygen pressure and temperatures. The energetics consideration reveals that the oxide islands have a higher dissociation oxygen

pressure than the bulk oxide. The dynamic observation of the shrinkage of oxide islands suggests the reduction of the oxide islands is a metal-air-oxide perimeter controlled decomposition process. These results present a novel method for producing nano-indentation arrays by reducing nano-oxide arrays initially formed by oxidation. These surface templates can serve as building blocks for the design and development of nano-devices.

7.2 EXPERIMENTAL OBSERVATIONS

Figure 7.1 (a) is a bright field image of a Cu film after the complete reduction of the oxide islands, where the original oxide islands were formed at 600°C and oxygen pressure of 5×10^{-4} torr. The area with bright contrast in the image corresponds to the thickness contrast due to the indentations in the Cu film. Figure 7.1 (b) is an AFM image of the same Cu film shown in Figure 7.1 (b), which reveals the nano-indentation array formed on the surface, where the typical depth of the indentations is ~35nm.

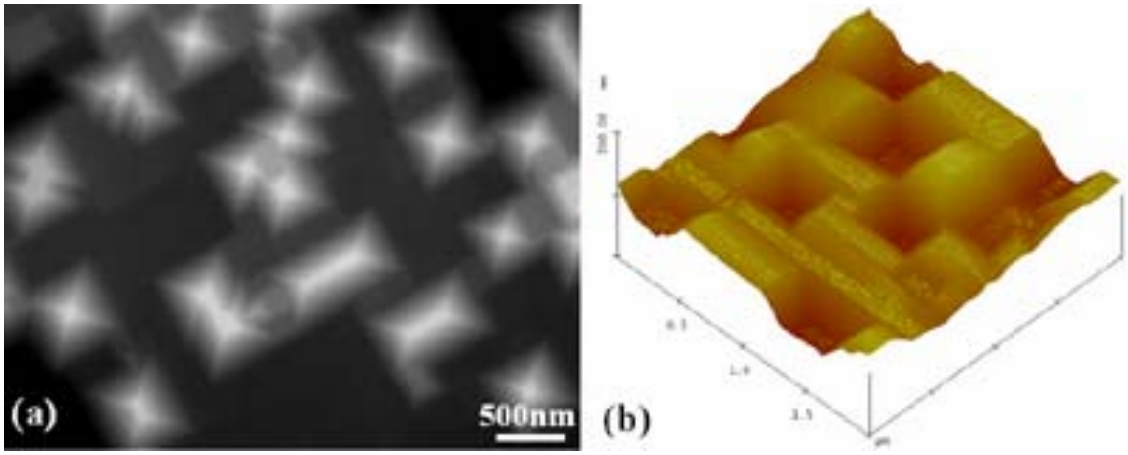

Figure 7.1 (a) Bright field image of the Cu(100) film after the complete reduction of the oxide islands, where the original oxide islands were formed at ~600°C and $P(O_2)= 5\times10^{-4}$ torr, the area with bright contrast is the thinned regions due to the oxide reduction; (b) AFM image showing the surface topology of the Cu film after the oxide reduction, which reveals the nano-indentation arrays formed on the surface, where the typical depth of the indentation is ~35nm.

We investigated the detailed morphology evolution of the oxide islands during reduction reaction to determine the kinetics of the reduction. Figure 7.2 is a BF image showing the morphology of the islands in the initial stages of the island reduction, where the area with bright contrast along the metal-oxide interface is the remaining Cu after the oxide reduction, which indicates that the metal-oxide interface is the preferred reduction site.

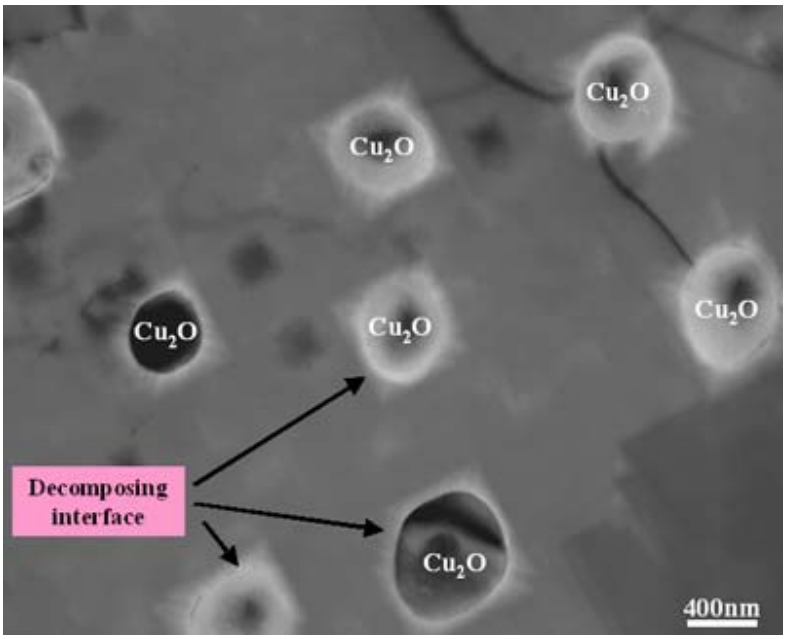

Figure 7.2 The morphology of the oxide islands in the initial stages of reduction reaction at 700°C and $P(O_2)= 8\times10^{-7}$ torr, which indicates that the metal-oxide interface is the preferred decomposition site.

The *in situ* observation of the morphology evolution of oxide islands provides more detailed information regarding the oxide reduction. Figure 7.3 shows the *in situ* reduction of an oxide island. The original oxide island had a square shape and the epitaxial relationship between the island and the Cu film is cube-on-cube. The normals to the edges of the islands are along <110> directions. The reduction started from the corners of the oxide islands, which causes the formation of <100> edges and its size increased with the shrinkage of the <110> edges. With the continuous reduction, V-shape trenches were formed at each corner. The oxide island had a fast decomposition rate at the beginning of the reaction, and there was a decrease in the rate with the continuous reduction. A DF image from $Cu_2O(110)$ reflection of the island corresponding to ~4min reduction in Figure 7.3(a) is shown in Figure 7.3(b). The bright contrast in the image

further confirmed that the oxide island was truncated square shaped, and the oxide in the trench area was completely reduced after 4 minutes. Figure 7.3 (c) is an AFM image of an island after the complete reduction, where the original island had the similar structure feature as Figure 7.3(a). The *in situ* observation also demonstrates that the oxide arrays with different intermediate shapes can be obtained by controlling the degree of the island decomposition, such as the annealing time.

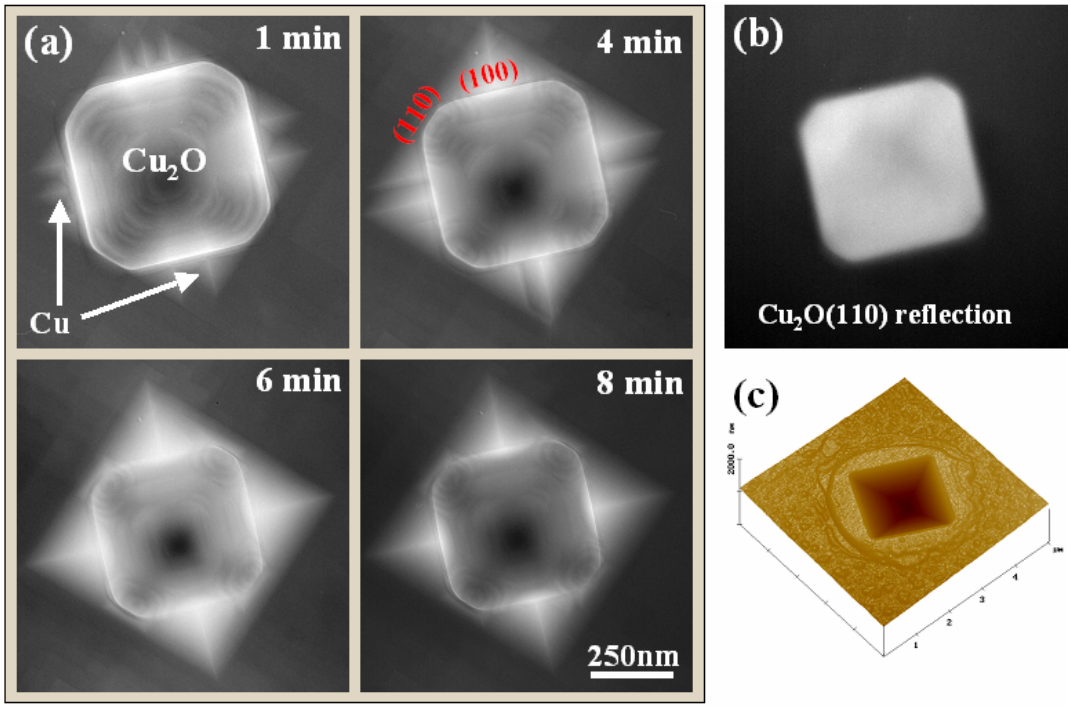

Figure 7.3 (a) The *in situ* observation of the reduction of an island at 800°C and oxygen pressure of 4×10^{-7}, where the original oxide islands were formed at the same temperature. (b) The DF TEM image from $Cu_2O(110)$ reflection of the island in above figure; (c) AFM image after the complete reduction of the oxide island, where the area with higher surface level around the indentation is the newly formed Cu surface after reduction of Cu_2O.

Pastorek and Rapp investigated the solubility of oxygen in bulk copper in the temperature range 800°C to 1030°C by electrochemical measurements and found the oxygen solubility increased from ~0.0018 atom% at 800°C to ~0.02 atom% at 1030°C [148, 149]. Therefore, the reduction of Cu_2O to Cu^0 is accompanied by the formation of a new metallic surface and oxygen dissolved in bulk Cu or desorbed from the surface as oxygen gas. Figure 7.4(a) shows the

morphology of the Cu film around the decomposing Cu_2O islands, the area with dark contrast around the islands is the newly formed Cu surface. The 4-fold symmetry of the newly formed Cu surface is related to the (100) surface structure of the Cu film. Figure 7.4(b) is an AFM image of the partially reduced oxide islands. The surface profile analysis indicates the thickness of the newly formed Cu is ~10nm, and there is a deep trench (~35nm) along the perimeter (Cu_2O-Cu-air interface) of the islands (Figure 7.4 (c, d)). The formation of the deep trench along the island perimeter suggests that the metal-oxide interface is the preferred site for oxide decomposition, and the Cu atoms decomposed from the oxide islands diffuse to Cu surface to form a new metallic surface.

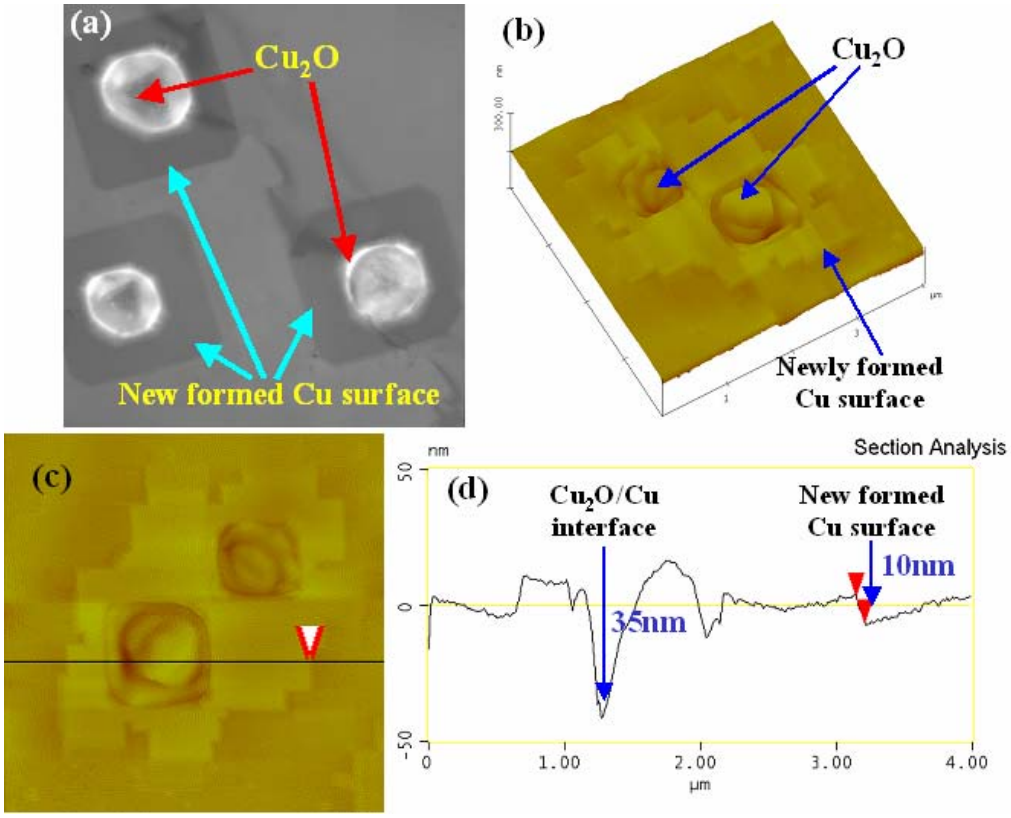

Figure 7.4 (a) BF image of the Cu film in the initial stages of the island reduction at ~700°C and oxygen pressure of 8×10^{-7} torr, where the area with dark contrast around the islands is the newly formed Cu surface; (b) AFM image of partially reduced oxide islands; (c, d) Surface profile analysis of the AFM along the marked line crossing the island and the new formed Cu surface indicates the new formed Cu surface has a height of ~10nm, and there is a deep trench (~35nm) along the perimeter (Cu_2O-Cu-air) of the islands.

7.3 DISCUSSION

7.3.1 Energetics of the oxide island reduction

For a theoretical understanding of the stability of the oxide islands, we first examine the energetics of formation of oxide islands. For the formation of an oxide island on metal surfaces, the total Gibbs free energy is expressed by

$$\Delta G = \frac{\Delta G^{f}}{V_0} \times V + \sigma^{Cu_2O} \times S^{Cu_2O} - \sigma^{Cu} \times S^{Cu} + \sigma^{I} \times S^{I} \tag{7.1}$$

where ΔG^f is molar bulk Gibbs free energy of the bulk oxide, V_0 is the molar volume of the oxide, V is the island volume, σ^{Cu_2O} represents the surface energy of the oxide, σ^{Cu} is the surface energy of Cu, σ^I represents the energy of the interface between the metal and oxide, S^{Cu_2O}, S^{Cu} and S^I denote the area of oxide island surface, Cu surface underneath the island, and island-metal interface, respectively. In most cases, experimental values are not available for the energies between the metal substrate and the oxide film. In our earlier calculation regarding the formation of one dimensional Cu_2O at 600°C, the experimentally obtained critical size (~110nm) was used to estimate the overall surface energies and interface energy (Γ) of the island, but the interface energies cannot be separated from the Γ due to the other unknown numbers in the Γ. Jeurgens, *et al.*, have given an expression, Equation (7.2), based on the macroscopic atom approach, to estimate the interface energies of the epitaxial growth of oxide on the surface [150].

$$\sigma_I \cong \frac{1.2\Delta H^{f} + 1\times 10^5}{(3/2)\times N_0 \times a^2} + h \times \left(\frac{E}{1-\nu}\right) \times \varepsilon^2 \tag{7.2}$$

where ΔH^f is the oxide formation enthalpy per mole oxygen, N_0 is Avogradro's number, a is lattice constant of metal surface; h is the thickness of the oxide island that is significantly strained, ε is the lattice mismatch between the oxide and metal, ν and E denote the Poisson and Young's modulus of the oxide, respectively. The first term in the above expression is the chemical energy that arises from interfacial bonding and the second term is the strain energy which arises from the lattice misfit.

To evaluate σ_I, the standard value of Young's modulus (30GN/m^2) and Poisson ration (0.455) of Cu_2O was used, the formation enthalpy of Cu_2O in the experimental temperature range is -1.67×10^5 J/mol [151], the lattice mismatch on the interface is $\frac{a_{Cu_2O} - a_{Cu}}{a_{Cu}}$, the thermal expansion coefficients, 1.9×10^{-6} °C^{-1} (Cu_2O) and 17×10^{-6} °C^{-1} (Cu), were included. The surface energy of the Cu_2O is unknown. But it has been reported that the surface energy of Cu_2O is equal to the surface energy of Cu at very low oxygen pressure, ~1.4J/m^2 [48, 152]. In our reduction experiments, the usual oxygen pressure is in the range of ~ 10^{-8} torr, therefore, we assumed that the surface energy of Cu_2O is equal to the surface energy of the Cu, 1.4J/m^2 in the calculation. For simplicity, we assume the oxide island to be a circular disk shape with radius of 100nm, and height of 25nm, which are the typical island sizes examined in our experiments.

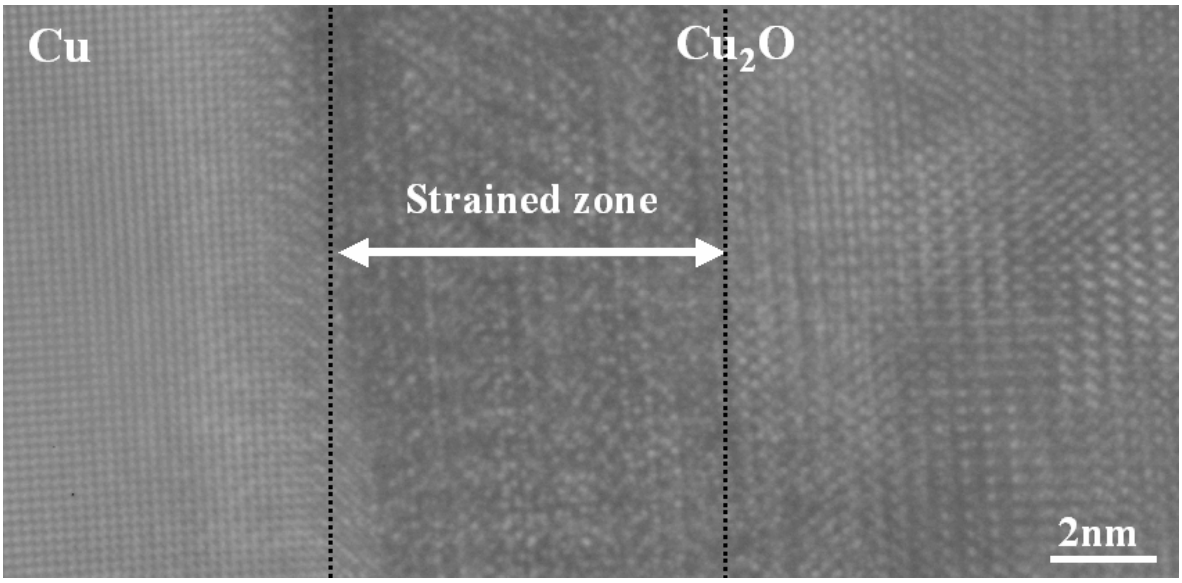

Figure 7.5 The HREM image of Cu/Cu_2O interface, where a highly strained zone of Cu_2O exists near the interface.

It is usually assumed that the mismatch between the oxide film and the substrate is accommodated elastically by the oxide near the metal-oxide interface. Therefore, the oxide film is most highly strained at the oxide-metal interface and has, virtually, bulk properties at the oxide-vapor interface. For most metal-oxide systems with lattice mismatch of 0.02-0.07, the strained oxide layer has a critical thickness of 5-10nm [150]. In the estimation of the interfacial strain energy of Cu_2O/Cu(100), we assumed that oxide island has a strained thickness of h=7nm

in the metal-oxide interface area as indicated by the HREM image in Figure 7.5. In this analysis, we assume that the Cu substrate is rigid, and the strain in the substrate is not considered. However, as we introduced in the Cu(111) oxidation, the lattice mismatch between Cu and Cu_2O can give rise to the strain not only in the oxide islands, but also in the Cu film. The occurrence of the strain in the substrate will affect the interface energy, and, therefore, this effect needs to be considered for the purpose of a more accurate estimation of the interface energy and the equilibrium oxygen pressure of the oxide islands.

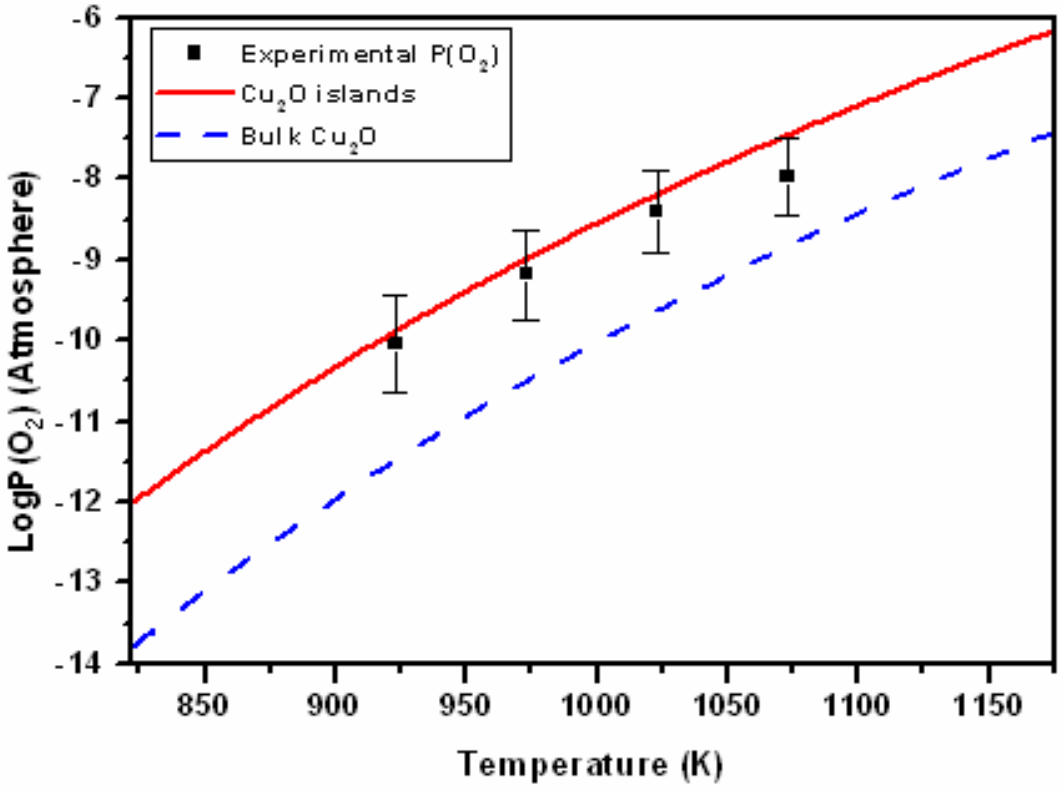

Figure 7.6 The equilibrium oxygen pressure of oxide islands and its comparison to bulk Cu_2O, where the square dots are the experimental oxygen pressures at which the oxide reduction was observed at the corresponding temperatures.

The Gibbs free energy of formation ΔG^f of 1 mole Cu_2O, $2Cu(s) + 1/2O_2(g) = Cu_2O(s)$, for a given temperature and oxygen pressure, is defined as

$$\Delta G^f = \Delta G^0 - \frac{RT}{2} \ln P_{O_2} \qquad (7.3)$$

where ΔG^0 is standard free energy of formation, R is gas constant, T is the oxidation temperature, and P_{O_2} is oxygen partial pressure. In the experimental temperature range (924-1328K), ΔG^0 is –166,900 + 71.1T (J/mol). At the dissociation pressure, the total Gibbs free energy for the formation of the oxide islands should be equal to zero. When the oxygen pressure is lower than the dissociation oxygen pressure, oxide islands tend to decompose, or oxide islands are not expected to form. The dissociation oxygen pressure of the oxide islands was experimentally determined by finding the temperature for a fixed oxygen pressure where decomposition of the oxide is observed. In Figure 7.6, the square dots are the experimental oxygen pressures at which the oxide reduction was observed at the corresponding temperatures. On the other hand, the formation of the oxide islands was not observed when the oxygen pressure is lower than the dissociation oxygen pressure. The dissociation oxygen pressures obtained from the thermodynamic data of bulk Cu_2O oxide are also shown in Figure 7.6. The oxide islands have a higher dissociation oxygen pressure than the bulk oxide, which demonstrates that the oxide islands have less stability than the bulk oxide.

7.3.2 Kinetics of the oxide island reduction

So far we have considered the energetics, but the oxide reduction depends also upon the kinetics. The comparison of the island size as a function of annealing time provides significant insights into the reduction kinetics. The AFM images (Figure 7.4(b, d)) indicate that the oxide perimeter is the preferred site for oxide reduction. The model for the oxide reduction is as follows. The reduction of Cu_2O along the perimeter of the islands results in Cu atoms and oxygen, where the Cu atoms diffuse to Cu surface around the islands and form unstrained Cu free surface, the oxygen is desorbed from the surface as oxygen gas. The interface reduction along the perimeter of the oxide island creates a shrinkage rate

$$\frac{dN(t)}{dt} = -CKJ \tag{7.4}$$

where $N(t)$ is the number of Cu atoms in a Cu_2O island at time t, K is the dissociation constant, J is the diffusive flux of copper atoms leaving the islands, and C is the perimeter of an island. Since the oxide islands have a lateral size of ~300nm, which is much larger than the island thickness (~30nm), therefore, we assume the islands have an oblate shape (the cross-sectional

area of the island on Cu surface has a circular shape) with radius r on the Cu surface and radius/height aspect ratio of β, the perimeter (C) of the island is $2\pi r$, the number of Cu atoms in the oxide island at time t is

$$\frac{dN(t)}{dt} = \frac{4\pi\beta}{\Omega} r^2 \frac{dr}{dt} \tag{7.5}$$

By solving the above differential equations (Eqn. 7.4 and 7.5), the island size decreases parabolically with respect to the reduction time

$$r^2 = r_0^2 - \frac{\Omega JK}{\beta} t \tag{7.6}$$

where Ω is the atomic volume of Cu in Cu_2O, r_0 is the island size before reduction.

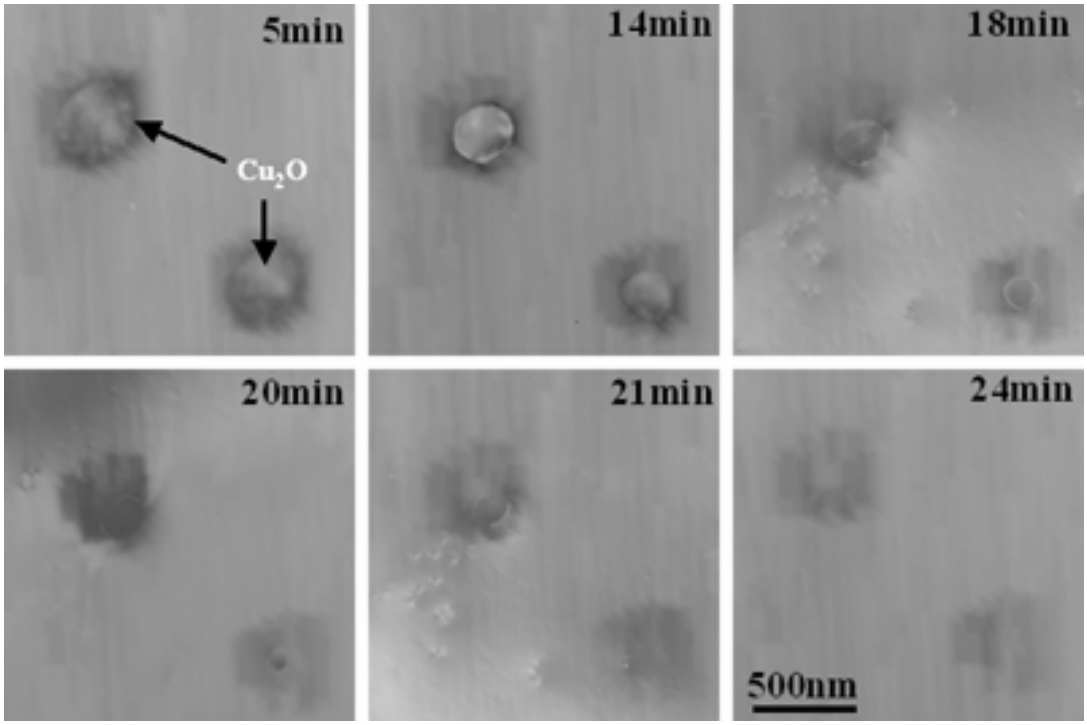

Figure 7.7 The *in situ* observation of the island reduction, where the original islands were formed at 750°C and 5×10^{-4} torr of oxygen pressure, and the islands were then annealed at the same temperature, but lower oxygen pressure, ~8×10^{-7} torr.

The evolution of Cu_2O islands size under isothermal annealing was followed inside the microscope and Figure 7.7 shows a time sequence of images focusing on the reduction of the oxide islands at the temperature of 750°C. The islands have circular cross-section shape, and the

formation of the dark contrast around the islands is due to the formation of new Cu surface during the oxide reduction. Figure 7.8 is the diagram of the oxide reduction based on the kinetics model described above. The island size at the different time was measured and shown in Figure 7.9 as the scattered dots. The solid line is the fit by Equation (7.6), where the coefficient ($\frac{JK}{\beta}$) of t in Equation (7.8) is the fit parameter. It is noted that the interface-controlled reduction model provides a good fit with the experimental data. The other mechanisms such as island surface-controlled or surface plus interface controlled reduction provide a linear or complex dependence of the island size on the reduction time (Appendix 4). Therefore, from the in-situ TEM observation and the AFM analysis of the surface topology of the partially decomposed Cu_2O islands, the parabolic law of the island size with the reduction time indicates that the reduction of the Cu_2O islands is related to the metal-oxide interface decomposition.

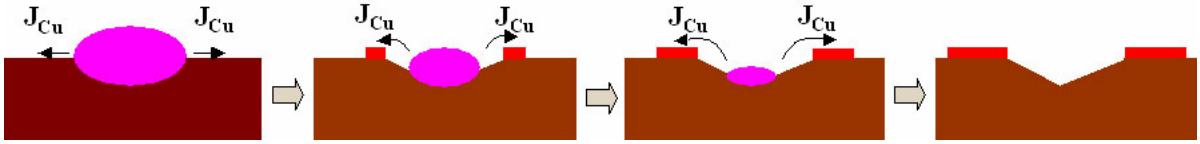

Figure 7.8 The schematics of the oxide reduction based on the kinetics model described in the text.

7.4 CONCLUSIONS

In conclusion, the stability of the oxide island arrays created by nano-oxidation was investigated by an *in situ* TEM. The calculation based on an energetics model by taking account of the interface energies into the reduction reaction shows that the Cu_2O islands have a higher dissociation oxygen partial pressure than bulk oxide. The kinetic data on the size evolution of the islands during the reduction reaction agree well with the model of metal-oxide interface controlled decomposition. These observations reveal an effective way to create nano-indentation arrays on metal surfaces by the reduction of oxide island arrays produced by nano-oxidation.

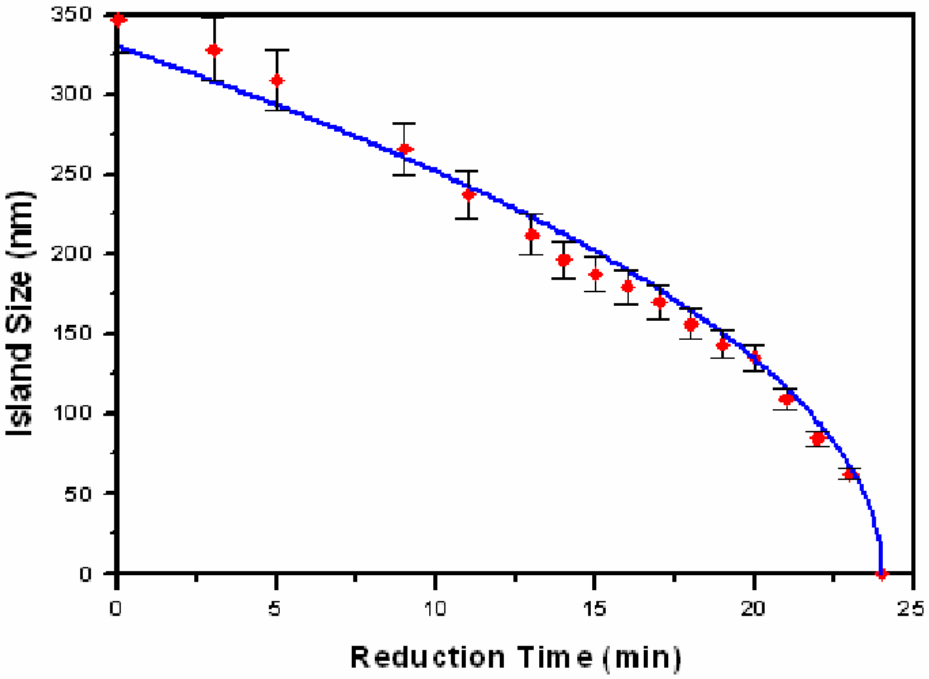

Figure 7.9 The evolution of the cross-section area of the oxide island with the reduction time, where the solid line corresponds to the theoretical fit of the metal-oxide-air interface limited reduction model to the experimental data.

8.0 CONCLUSIONS

The initial stages of oxidation of Cu(100), (110), and (111) surfaces have been investigated by *in situ* UHV-TEM. It has been demonstrated that the surface structure and the strain between the oxide and copper substrate have a dramatic effect on the kinetics and energetics of oxide formation.

In Cu(100) oxidation at a low oxygen pressure of ~10^{-4} torr, dramatically different oxide morphology was obtained by simply altering the oxidation temperature. Oxidation at temperatures lower than 400ºC resulted in triangular-shaped Cu_2O islands. Oxidation at temperatures between 400ºC and 550ºC resulted in square-shaped islands. Epitaxial Cu_2O islands on Cu(100) surfaces, formed at 600°C, were observed to undergo a shape transition from initially square shaped islands to elongated islands at a critical size of ~110nm. We have observed such elongated islands with aspect ratios as large as 40:1. The experimental data on the elongation of Cu_2O islands agree with energetic calculations based on the balance between surface plus interface energies and the elastic stress relaxation in the three dimensional islands. We developed a kinetic model based on oxygen surface diffusion that fits well with the observed volume evolution of the Cu_2O islands at T=600°C and $P(O_2)=5\times10^{-4}$ torr. A peculiar hollow pyramid structure was formed when Cu(100) films were oxidized at 1000°C. A model based on the plastic slip in the oxide to release the transformation strain induced by the large lattice change accompanied with oxidation of Cu to Cu_2O was proposed to explain the hollowing process within the pyramids.

The oxygen surface diffusion model that was developed to describe nucleation and growth of Cu_2O on clean single crystals of Cu(100) have been extended to the case of the Cu(110) surface. The dynamic observation of the nucleation and growth of Cu oxide showed a highly enhanced oxidation rate on Cu(110) surface as compared to Cu(100). The larger island density and increased growth rate may explain the improved passivation behavior of Cu(110) vs Cu(100). The kinetic data on the nucleation and growth of the 3-dimensional oxide islands at oxidation

temperatures lower than 500°C agree well with the heteroepitaxial model of surface diffusion of oxygen. Increasing oxidation temperature only increased the thickness of the Cu_2O islands. We speculate that the elevation of the oxidation temperature decreases the interfacial strain and energy, and thereby permits a more compact oxide island with increased oxide thickness to grow into the Cu film as opposed to a "flatter" island with larger surface area and smaller interface area. The investigation of the oxidation on thermally roughened Cu(110) surface revealed that increased surface roughness will increase the nucleation density of oxide islands. The oxidation on the faceted Cu(110) surface resulted in the preferred nucleation and growth of oxide islands along the "valley" of the facets.

The Cu(111) surface revealed a completely different oxidation behavior than that of Cu(100) and (110). The nucleation and growth processes of oxide islands dominate when the oxidation temperature is lower than 550°C. However, when the oxidation temperature is between 550°C and 600°C, the lateral growth process of the oxide dominates, which results in "cellular oxide" structure. Oxidation at 700°C results in the formation of continuous oxide thin films that have a triangular perimeter. This different oxidation behavior is explained by the Cu-O surface reconstruction, providing a near perfect template for (111)Cu_2O. The change of the oxide structure is explained by the different growth modes of the oxide at the different temperatures. The oxidation at temperatures lower than 500°C has an "islanding" mode of the oxide formation, while the oxidation at 500°C and at higher temperatures has a layer-by-layer growth mode caused by the decreasing interfacial lattice strain with increasing temperature. It is found that Cu_2O on Cu(111) has a nearly perfect 6 to 7 lattice coincidence due to the ~1.4% compressive strain in the underlying Cu and 1.7% compressive strain in Cu_2O lattices as compared to their unstrained states. The compressive strain in the Cu film under the oxide layer causes ~1.1% tensile strain in the Cu film near the oxide layer.

The stability of the oxide island created by nano-oxidation was also investigated. The experimental observation revealed that the oxide islands have a higher dissociation oxygen pressure than bulk oxide. Energetic calculations also confirmed this phenomenon when interfacial energies were included. The kinetic data on the size evolution of the islands during the reduction reaction suggest that the reduction of the islands is a "metal-oxide-air" perimeter controlled decomposition process. These observations also reveal an effective way to create

nano-indentation arrays on metal surfaces by the reduction of oxide island arrays produced by nano-oxidation.

9.0 OUTLOOK

9.1 INTRODUCTION

This work has demonstrated the unusually wide variety of nano-oxide structures created by simple nano-processes. The opportunity exists to provide important advances in a variety of advanced technologies via exploitation of the potentially novel optical, magnetic and sensor properties of these metal–oxide arrays. Furthermore, such oxide nanoparticle arrays may provide the needed template for the nanopatterning of a variety of biological molecules [153-155]. Surface-pattern based biotechnology is a fascinating field of research, which impacts biotechnology and medicine since the investigation of patterned surfaces can be templates for isolated organelles, living cells and macromolecules. Nano oxidation can pattern metal surfaces to form hydrophilic and hydrophobic regions on the nanometer scale and this opens up possibilities for selectively patterning interesting organic molecules on the oxide array or metal surface [156-159]. Future experimental investigations can combine fundamental and applied studies to: 1) provide fundamental understanding of formation, distribution, stability, and morphological evolution of nanoscale oxide arrays in different materials system, 2) demonstrate the feasibility of using nano-oxide arrays in applications such as nano-magnetism and nano field-emission, 3) demonstrate the feasibility of making new kinds of biosensors/biocomputers by functionalizing organic molecules onto oxide arrays.

9.2 EXPERIMENTAL REQUIREMENTS

As introduced in the preceding chapters, the initial surface conditions, such as surface impurities and surface morphology, can greatly influence the oxide nucleation, growth and, hence, the

morphology, distribution, size, stability, etc. of the oxide island arrays. Therefore, the experiments must be performed under UHV conditions. For the production of large scale of oxide island arrays, a preparation chamber with UHV, controlled gas leakage and high temperature annealing capabilities is needed.

The surface cleaning is also very important for formation of well ordered arrays of oxide islands. In the present work, we used methanol gas (this is special to Cu_2O) or high temperature annealing to remove the native oxide layer on Cu surfaces. For other materials systems, some other reactive gas may be needed to remove the native oxide on the surfaces. Therefore, the chamber needs the capability to leak in different chemical gas species. A sputtering gun is also needed to remove the native oxide layer which cannot be cleaned by chemical gas reaction or high temperature annealing.

The structural characterization can be realized by TEM, SEM, AFM, MFM to reveal the morphology, microstructure, distribution, size, etc. of the oxide island arrays. X-ray diffraction can be used to measure the strain evolution in the islands. The characterization of the properties of the oxide island arrays may include optical, magnetic, electric, sensor, etc., properties.

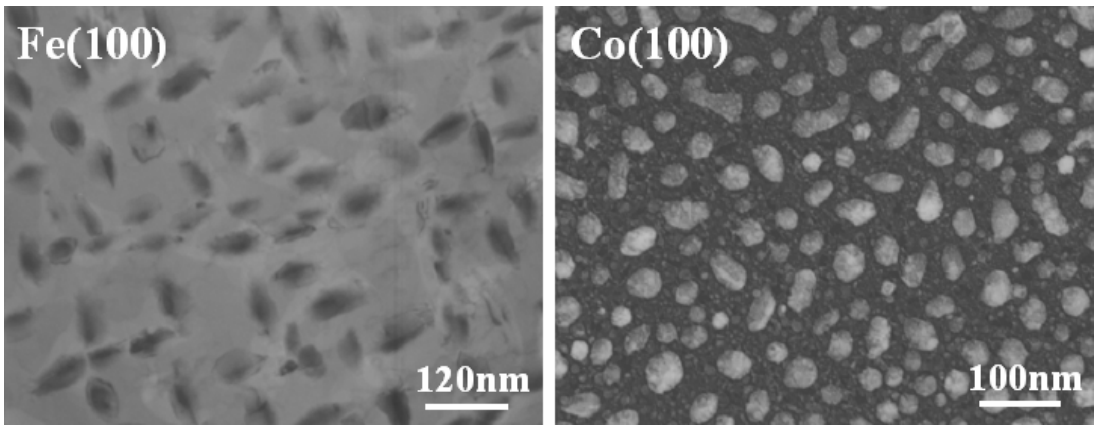

Figure 9.1 The oxidation of Fe(100) and Co(100) film at 800°C

9.3 PRELIMINARY RESULTS

Island formation during oxidation has been observed in several other metal systems, such as Ni, Fe, Al, Ti, Co, Pd, Ir, Sn, as well as in Cu. By carefully choosing the oxidation parameters, such

as oxidation temperature, oxygen pressure, substrate orientation, etc, these principles developed formerly could be applied to other metal systems and the nano- oxide arrays with different structures could be realized.

Figure 9.1 shows the preliminary results regarding the oxide island patterns obtained by nano oxidation of Fe and Co films which have the technological importances for memory devices. The array of these nanometer sized magnetic oxide islands could have a preferred magnetization direction and consists of a single domain. These nanosized magnet patterns are attractive candidates for highly spin polarized transport in spin valve applications (spintronics) and in the magnetic recording industry.

Titanium has several stable oxide states, TiO_2, TiO, Ti_2O_3 and Ti_3O_5 [160-162]. It has been known that TiO_2 shows the hydrophilicity and exhibits the outstanding decomposition ability toward organic compound and fairly good antibacterial activity with its strong photocatalytic reaction activated by the illumination of ultraviolet (UV) light [156-159]. The formation of TiO_2 array by controlled oxidation of Ti films will enable us to nanopattern many macromolecules on Ti surface under certain photocatalytic reaction conditions. Figure 9.2 shows the oxidation of Ti(100) film at 800°C and oxygen pressure of 5×10^{-4} torr, the electron diffraction pattern indicates that many Ti oxide phases exist on the surface. To obtain single phase of TiO_2 arrays on surface, intensive experimental investigation regarding the effect of the different oxidation conditions, such as oxidation temperature, oxygen pressure, etc., on the oxide structure, is needed.

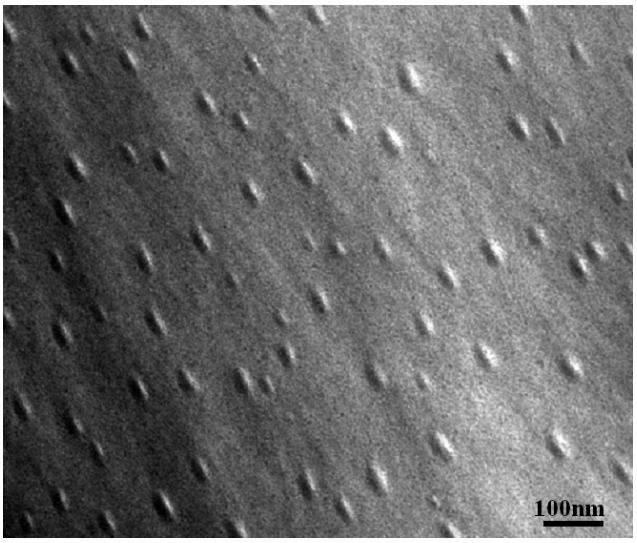

Figure 9.2 The oxidation of Ti(100) film at 800°C and oxygen pressure of 5×10^{-4} torr

APPENDIX A

OXYGEN SURFACE DIFFUSION MODEL

Nucleation of oxide islands

Probability of nucleation is proportional to the surface area remaining free (not within an active zone of capture), which gives rise to the nuclei density as a function of time

$$dN = k(1 - L_D^2)dt \tag{A.1.1}$$

where k is the initial oxidation rate which depends on probability of Cu-O bonding, and L_D^2 is the area of oxygen zone capture. The first order of linear differential equation of nuclei number of the oxide islands is

$$\frac{dN}{dt} + kL_D^2 N = k \tag{A.1.2}$$

The homogeneous solution of equation A.1.2 is

$$\frac{dN}{dt} + kL_D^2 = 0 \tag{A.1.3}$$

$$\int \frac{dN}{dt} = \int -kL_D^2 dt \tag{A.1.4}$$

$$N_h(t) = e^{-kL_D^2 t} \tag{A.1.5}$$

The particular solution of equation A.1.2 is a(t)

$$N_h(t)\frac{da(t)}{dt} = k \tag{A.1.6}$$

a(t) is obtained by solving the above equation

$$\int da(t) = \int k e^{kL_D^2 t} dt \tag{A.1.7}$$

$$a(t) = \frac{1}{L_D^2} e^{kL_D^2 t} + C \tag{A.1.8}$$

The nuclei number as a function of oxidation time is obtained as

$$N(t) = a(t)N_h(t) = \frac{1}{L_D^2} + Ce^{-kL_D^2 t} \tag{A.1.9}$$

Applying the boundary condition: N=0 at time t=0, *N(t)* is determined as

$$N(t) = \frac{1}{L_D^2}\left(1 - e^{-kL_D^2 t}\right) \tag{A.1.10}$$

The initial nucleation rate is $\frac{dN}{dt}\big|_{t=0} = ke^{-kL_D^2 T} = k$; and nuclei density saturation is $\frac{1}{L_D^2}$.

Kinetics of Cu_2O growth

Assumption: Oxygen surface diffusion to perimeter of island in the "active" zone.

N(t): the number of oxygen atoms in Cu_2O at time t.

$$\frac{dN(t)}{dt} = c \times f \times 2\pi r \tag{A.1.11}$$

where c is sticking coefficient, f is flux of oxygen, and 2πr is the island perimeter (assuming circular shape).

For 2D lateral growth only, the number of O atoms in an oxide island with radius of r and constant height of a is $N = \frac{\pi a r^2}{\Omega}$, Ω is volume occupied by 1 O atom in Cu_2O.

$$\frac{dN}{dr} = \frac{2\pi a}{\Omega} r \tag{A.1.12}$$

Then

$$\frac{dN}{dt} = \frac{2\pi a}{\Omega} r \frac{dr}{dt} = c \times f \times 2\pi r \tag{A.1.13}$$

By solving the above equation, the radius of the island as a function of oxidation time is determined as

$$r(t) = \frac{cf\Omega}{a}(t - t_0) \tag{A.1.14}$$

The cross-sectional area of the island is

$$A(t) = \pi\left(\frac{cf\Omega}{a}\right)^2 (t - t_0)^2 \tag{A.1.15}$$

For 3D growth: oxygen surface diffusion to perimeter of 3D island. Now the number of oxygen atoms in the island is $N = \frac{\frac{4}{3}\pi r^3}{\Omega}$, and $\frac{dN}{dr} = \frac{4\pi r^2}{\Omega}$. By inserting the determined N into equation (A.1.11), the radius of the island is determined as

$$r^2 = \Omega c f (t - t_0) \tag{A.1.16}$$

The cross-sectional area of the island with 3D growth mode is

$$A(t) = \pi \Omega c f (t - t_0) \tag{A.1.17}$$

Consider the island growth caused by surface diffusion of oxygen to perimeter plus impingement or interface diffusion:

$$\frac{dN}{dt} = c_1 f_1 \times 2\pi r + c_2 f_2 \times 2\pi r^2 \tag{A.1.18}$$

For 3D sphere with radius of r,

$$\frac{dr}{dt} = \frac{c_1 f_1 \Omega}{2} \times \frac{1}{r} + \frac{c_2 f_2 \Omega}{2} \tag{A.1.19}$$

Define $k_1 = \frac{c_1 f_1 \Omega}{2}$; $k_2 = \frac{c_2 f_2 \Omega}{2}$, and solve the above equation, the radius of the island can be determined as

$$\frac{r}{k_2} - \frac{k_1}{k_2^2} \ln(k_1 + k_2 r) = t - t_0 \tag{A.1.20}$$

Therefore, the cross-sectional area, A, of the island is

$$\frac{A^{1/2}}{\pi^{1/2} k_2} - \frac{k_1}{k_2^2} \ln\left(k_1 + \frac{k_2}{\pi^{1/2}} A^{1/2} \right) = t - t_0 \tag{A.1.21}$$

APPENDIX B

SIZE AND VOLUME EVOLUTION OF ONE-DIMENSIONAL Cu_2O STRUCTURE

Size evolution

According to Tersoff model [77], the energy per volume of the strained island is

$$\frac{E}{V} = 2\Gamma\left(\frac{1}{s}+\frac{1}{t}\right)+\frac{1}{h}\left(r_i + r_t - r_s\right) - 2ch\left[\frac{1}{s}\ln\left(\frac{se^{3/2}}{h\cot\theta}\right)+\frac{1}{t}\ln\left(\frac{te^{3/2}}{h\cot\theta}\right)\right] \tag{A.2.1}$$

where V=hst=hA is the island volume (A=st, the island cross-sectional area). We can rewrite the island energy as a function of s (island width).

$$E(s) = Ah\times\left\{2\Gamma\left(\frac{1}{s}+\frac{s}{A}\right)+\frac{1}{h}\left(r_i + r_t - r_s\right) - 2ch\left[\frac{1}{s}\ln\left(\frac{se^{3/2}}{h\cot\theta}\right)+\frac{s}{A}\ln\left(\frac{Ae^{3/2}}{sh\cot\theta}\right)\right]\right\} \tag{A.2.2}$$

By minimizing the island energy with respect to s at fixed area (A)

$$\frac{\partial E(s)}{\partial s} = 0 \tag{A.2.3}$$

Then s can be calculated numerically for different areas from the following equation

$$2\Gamma\left(-\frac{1}{s^2}+\frac{1}{A}\right) - 2ch\left[-\frac{1}{s^2}\ln\left(\frac{se^{3/2}}{h\cot\theta}\right)+\frac{h\cot\theta}{s^2e^{3/2}}+\frac{1}{A}\ln\left(\frac{Ae^{3/2}}{sh\cot\theta}\right)-\frac{1}{A}\right] = 0 \tag{A.2.4}$$

Similarly, t can be also known once s is determined for different area A.

Volume evolution of the oxide island based on oxygen surface diffusion

The island growth is caused by the oxygen surface diffusion to the island perimeter, and the number of oxygen atoms in the island at time t is

$$\frac{dN(t)}{dt} = c\times f\times perimeter \tag{A.2.5}$$

c is sticking coefficient and *f* is oxygen flux.

Assuming the island has constant height of a, before shape transition, the island has a square shape with equal width and length of s. The island perimeter is 4s, and the number of O atoms in the island is $N = \frac{s^2 h}{\Omega}$. By solving equation (A.2.5) with these numbers, the island size, s, can be determined to be

$$s(t) = \left(\frac{cf\Omega}{2h} \right) \times (t - t_0) \tag{A.2.6}$$

Therefore, the island volume increases parabolically with oxidation time as follows

$$V^I(t) = \left(\frac{cf\Omega}{2h} \right)^2 \times h \times (t - t_0)^2 \tag{A.2.7}$$

During the shape transition zone, where the island width (t) and length (s) change simultaneously, the oxygen surface diffusion to the island perimeter (2s+2t) creates a growth rate

$$\frac{dN(t)}{dt} = 2 \times c \times f \times (s + t) \tag{A.2.8}$$

The O atom number in the island at time t is $N = \frac{V(t)}{\Omega}$, and $\frac{dN}{dt} = \frac{1}{\Omega}\frac{dV}{dt}$. By inserting these numbers into equation A.2.8, the island volume at time t during shape transition zone is

$$V^{II}(t) = 2cf\Omega \int [s(t) + t(t)] dt \tag{A.2.9}$$

After shape transition, the island has an almost constant width a_0, but its length continues to growth. The O atom number in the island at time t is $N = \frac{s \times a_0 \times h}{\Omega}$, and $\frac{dN}{dt} = \frac{a_0 \times h}{\Omega}\frac{ds}{dt}$, which gives a differential equation to calculate length change, $\frac{a_0 \times h}{\Omega}\frac{ds}{dt} = 2cf(s + a_0)$. By solving this equation, we can have the island length, s, at time t

$$s(t) = \frac{a_0 \times h}{2cf\Omega} \left[e^{\frac{2cf\Omega}{h a_0}} - \frac{2cf\Omega}{h} \right] \tag{A.2.10}$$

The island volume is

$$V^{III}(t) = \frac{(\alpha_0 h)^2}{2cf\Omega} \left(e^{\frac{2K_S J_S \Omega}{\alpha_0 h}(t - t_0)} - \frac{2cf\Omega}{h} \right) \tag{A.2.11}$$

APPENDIX C

TRANSFORMATION STRAIN ENERGY AND WORK DONE BY SLIP

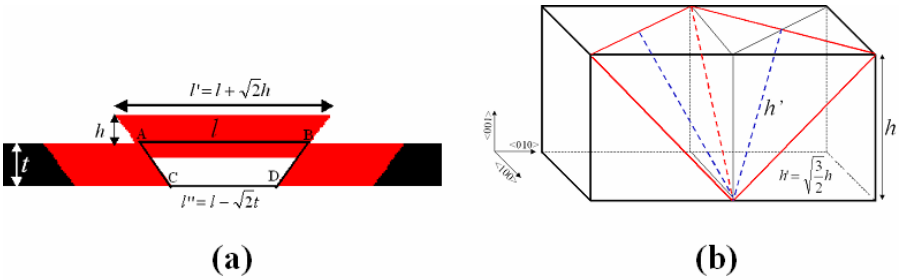

Figure A.1 The schematics of container structure (a) and the crystallorgraphic geometry of Cu_2O

We first consider the first layer of the pyramid as shown in Figure 9.3(a). ABCD is the strained part which provides driving force for slip. The structure geometry is shown in Figure 9.3(b). The volume of frustrum ABCD is $V = \frac{1}{3}t\left[l^2 + \left(l-\sqrt{2}t\right)^2 + l\times\left(l-\sqrt{2}t\right)\right]$.

$$V = \frac{1}{3}t\times\left[3l^2 - 3\sqrt{2}tl + 2t^2\right] \tag{A.3.1}$$

The lateral surface area of the frustrum ABCD is $S = \sqrt{6}\times t\times[l+(l-\sqrt{2}t)]$,

$$S = \sqrt{6}\times t\times(2l-\sqrt{2}t) \tag{A.3.2}$$

Strain energy per unit volume U_0 of Cu_2O due to the transformation from Cu:

$$U_0 = \int\sum_{i=1}^{3}\sigma_i d\varepsilon_i = \int\left(\sigma_x d\varepsilon_x + \sigma_y d\varepsilon_y + \sigma_z d\varepsilon_z\right) \tag{A.3.3}$$

where $\sigma_z = 0$ (i.e., the oxide can not support a stress in the free direction) and the x and y components of the normal strain are equal. From Hooke's law,

$$\varepsilon_x + \varepsilon_y = \frac{1-\nu}{E}\left(\sigma_x + \sigma_y\right) \tag{A.3.4}$$

in which E is Young's modulus of the Cu_2O, and ν is the Poisson's ratio of the Cu_2O. Combining equations A(3.3) and A(3.4) yields

$$U_0 = 2\int \frac{E}{1-\nu}\varepsilon d\varepsilon = \frac{E}{1-\nu}\varepsilon^2 \tag{A.3.5}$$

where E=30GPa, ν=0.455, $\varepsilon = \dfrac{\left(a_{Cu_2O} - a_{Cu}\right)}{a_{Cu}}$,

$a_{Cu_2O} = 4.217 + 4.217 \times \left(1000^\circ C - 27^\circ C\right) \times 1.9 \times 10^{-6}\left(^\circ C^{-1}\right)$,

$a_{Cu} = 3.61 + 3.61 \times \left(1000^\circ C - 27^\circ C\right) \times 17 \times 10^{-6}\left(^\circ C^{-1}\right)$.

The work done by slip

$$W = S \times \tau \times d = S \times \tau \times \sqrt{\frac{3}{2}}h \tag{A.3.6}$$

where S is surface area for slip, τ is the shear stress along the slip direction on the slip plane, d is the slip distance. Consider the integrated work w by slip, $S = \sqrt{6} \times n \times \left(2l - \sqrt{2}n\right)$. Assume z=t-n, n(h)=t-h, $W = \int_0^h \tau \times S(z)dz \times \left(\sqrt{\frac{3}{2}}\right)$

$$W = -\int_t^{t-h} \tau\sqrt{6}n\left(2l - \sqrt{2}n\right)dn \times \left(\sqrt{\frac{3}{2}}\right) = 3\tau\int_{t-h}^{h}\left(2l \times n - \sqrt{2}n^2\right)dn$$

$$W = 3\tau \times \left[l \times n^2 - \frac{\sqrt{2}}{3}n^3\right]_{t-h}^{t} = 3\tau \times \left\{l \times [t^2 - (t-h)^2] - \frac{\sqrt{2}}{3} \times [t^3 - (t-h)^3]\right\}$$

$$W = 3\tau \times l \times [t^2 - (t-h)^2] - \sqrt{2} \times \tau \times [t^3 - (t-h)^3] \tag{A.3.7}$$

Assuming the whole stored strain energy is released by the slip process, then the shear stress for the slip can be determined.

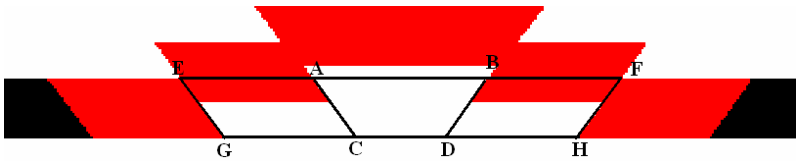

Figure A.2 The schematics of a container with two terraces

Now we consider the second layer: $AB = l_1$, $EF = l_2$, $CD = l_1 - \sqrt{2}t$, $GH = l_2 - \sqrt{2}t$ (Figure 9.4). The volume of the frustrum of ABCD is $V_1 = \frac{1}{3} \times t \times \left[3{l_1}^2 - 3\sqrt{2}tl_1 + 2t^2 \right]$, The volume of the frustrum of EFGH is

$$V_2 = \frac{1}{3} \times t \times \left[3{l_2}^2 - 3\sqrt{2}tl_2 + 2t^2 \right] \tag{A.3.8}$$

The strained volume which provides driving force for second slip is:

$$V_2 - V_1 = \frac{1}{3} \times t \times \left[3 \times \left(l_2^2 - l_1^2 \right) - 3\sqrt{2} \times t \times \left(l_2 - l_1 \right) \right]$$

$$V_2 - V_1 = t \times [\left(l_2^2 - l_1^2 \right) - \sqrt{2} \times t \times \left(l_2 - l_1 \right)] \tag{A.3.9}$$

The lateral surface area of the frustrum EFGH is $S_2 = \sqrt{6} \times t \times (2 l_2 - \sqrt{2} t)$, Therefore, the strain energy is

$$S.E = t \times [\left(l_2^2 - l_1^2 \right) - \sqrt{2}t\left(l_2 - l_1 \right)] \times \left(\varepsilon^2 E + \gamma^2 G \right) \tag{A.3.10}$$

The work done by slip is:

$$W = 3\tau \times l_2 \times [t^2 - \left(t - h \right)^2] - \sqrt{2} \times \tau \times [t^3 - \left(t - h \right)^3] \tag{A.3.11}$$

Similarly, we can calculate the strain energy of multiple slips:

$$S.E = t \times [\left(l_i^2 - l_{i-1}^2 \right) - \sqrt{2}t\left(l_i - l_{i-1} \right)] \times \left(\varepsilon^2 E + \gamma^2 G \right) \tag{A.3.12}$$

The work done by slip is:

$$W = 3\tau \times l_i \times [t^2 - \left(t - h \right)^2] - \sqrt{2} \times \tau \times [t^3 - \left(t - h \right)^3] \tag{A.3.13}$$

APPENDIX D

REDUCTION KINETICS CONTROLLED BY METAL-AIR-OXIDE INTERFACE

The reduction along the perimeter of the oxide island creates a shrinkage rate

$$\frac{dN(t)}{dt} = -CKJ \tag{A.4.1}$$

where *N(t)* is the number of Cu atoms in a Cu_2O island at time t, *K* is the dissociation constant, *J* is the diffusive flux of copper atoms leaving the islands, and *C* is the perimeter of an island. By assuming a simple ellipsoid shape of the island with circle cross-section shape (radius of *r*) on Cu film surface and height/radius (h/r) aspect ratio of β, the number of Cu atoms in the island is expressed

$$N = \frac{\frac{4}{3}\pi r^3 \beta}{\Omega} \tag{A.4.2}$$

where Ω is the atomic volume of Cu in Cu_2O. The number of Cu atoms at time t is

$$\frac{dN}{dt} = \frac{4\pi\beta}{\Omega} r^2 \frac{dr}{dt} \tag{A.4.3}$$

The reduction rate of the island along the metal-air-oxide perimeter is

$$\frac{dN(t)}{dt} = -KJ \times 2\pi r \tag{A.4.4}$$

Equating Eq. (A.4.3) and (A.4.4) gives rise to the reduction rate of the island

$$r\frac{dr}{dt} = -\frac{KJ\Omega}{2\beta} \tag{A.4.5}$$

By solving the above differential equations, the island size decreases parabolically with respect to the reduction time

$$r^2 = r_0^2 - \frac{\Omega JK}{\beta} t \tag{A.4.6}$$

where r_0 is the island size before the reduction.

If the reduction occurs on the island surface, then the reduction rate will be

$$\frac{dN(t)}{dt} = -KJ \times S \tag{A.4.7}$$

where S is the surface area of the island, and can be calculated as

$$S = \pi r^2 \times \left[1 + \frac{\beta^2}{\sqrt{1-\beta^2}} \times \ln\left(\frac{1+\sqrt{1-\beta^2}}{1-\sqrt{1-\beta^2}} \right) \right] = \pi \alpha r^2 \tag{A.4.8}$$

Therefore, the reduction rate of the island can be calculated as,

$$\frac{dN}{dt} = \frac{4\pi\beta}{\Omega} r^2 \frac{dr}{dt} = -KJ\pi\alpha r^2 \tag{A.4.9}$$

By solving the above equation, we can have a linear reduction rate of the island size as a function of reduction time:

$$r = r_0 - \frac{KJ\Omega\alpha}{4\beta} t \tag{A.4.10}$$

Similarly, if the reduction is controlled by both the metal-air-oxide interface and the island surface, then the reduction rate of the island will be

$$\frac{dN}{dt} = -K_1 J_1 \times 2\pi r - K_2 J_2 \times \alpha \pi r^2 \tag{A.4.11}$$

where K_1, J_1 are the dissociation coefficient and flux of Cu atoms for the interface reduction, K_2, J_2 are the dissociation coefficient and flux of Cu atoms for island surface reduction. The reduction rate of the island can be calculated as,

$$\frac{dN}{dt} = \frac{4\pi\beta}{\Omega} r^2 \frac{dr}{dt} = -K_1 J_1 \times 2\pi r - K_2 J_2 \times \alpha \pi r^2 \tag{A.4.12}$$

Solving the above equation gives an expression to describe the island size as a function of time as follows

$$\frac{4\beta}{K_2 J_2 \Omega \alpha}(r_0 - r) - 4\left(\frac{K_1 J_1}{K_2 J_2 \alpha} \right)^2 \ln\left[\frac{K_2 J_2 \alpha \Omega}{4\beta} \right] \times (r_0 - r) - \frac{K_1 J_1 \Omega}{2\beta} = t \tag{A.4.13}$$

BIBLIOGRAPHY

1. Besenbacher, F., and Norskov, J.K., Progress in Surface Science, 1993. **44**: p. 5-66.

2. Tanaka, K., Fujita, T., and Okawa, Y., Surface Science, 1998. **401**: p. L407-412.

3. Leibsle, F.M., Surface Science, 1998. **337**(1-2): p. 51-66.

4. Lederer, T., Arvanitis, D., Comelli, G., Troger, L., Baberschke, K., Phys. Rev. B., 1993. **48**: p. 15390-15404.

5. Knight, P.J., Driver, S.M., Woodruff, D.P., J Phys-Condens Mat., 1997. **9**(1): p. 21-31.

6. Coulman, D.J., Wintterlin, J., Behm, R.J., Ertl, G., Phys. Rev. Lett., 1990. **64**: p. 1761-1764.

7. Schroeder, T., Giorgi, J.B., Hammoudeh, A., Magg, N., Baumer, M., Freund, H.J., Phys. Rev. B., 2002. **65**(11): p. 115411-115418.

8. Africh, C., Ssch, F., Comelli, G., Rosei, R., J. Chem. Phys., 2001. **115**: p. 477-481.

9. Matsumoto, T., Bennett, R.A., Stone, P., Yamada, T., Domen, K., Bowker, M., Surface Science, 2001. **471**(1-3): p. 225-245.

10. Alfe, D., de Gironcoli, S., Baroni, S., Surface Science, 1999. **437**(1-2): p. 18-28.

11. Niehus, H., Achete, C., Surface Science, 1996. **369**(1-3): p. 9-22.

12. Jensen, F., Besenbacher, F., Stensgaard, I., Surface Science, 1992. **269/270**: p. 400-404.

13. Ikemiya, N., Kubo, T., and Hara, S., Surface Science, 1995. **323**: p. 81-90.

14. Ikemiya, N., Gewirth, A.A., Journal of the American Ceramics Society, 1997. **119**: p. 9919-9920.

15. Chu, Y.S., Robinson, I.K., and Gewirth, A.A., Phys. Rev. B., 1997. **55**: p. 7945-7954.

16. Mennicke, C., Clarke, D.R., and Ruhle, M., Oxidation of Metals, 2000. **55**(5/6): p. 551-569.

17. Wagner, C., Z. Phys. Chem., 1933. **21**: p. 25-41.

18. Cabrera, N., and Mott, N.F., Rep. Prog. Phys., 1948. **12**: p. 163.

19. Mennicke, e.a., Private communication.

20. Homma, T., Khoi, N.N., Smeltzer, W.W., Embury, J.D., Oxidation of Metals, 1971. **3**: p. 463.

21. Graham, M.J., Hussey, R.J., Cohen, M., J. Electrochem. Soc., 1973. **120**: p. 1523.

22. Khoi, N.N., Smeltzer, W.W., Embury, J.D., J. Electrochem. Soc., 1975. **122**: p. 1495.

23. Ross, F.M., Tromp, R.M., and Reuter, M.C., Science, 1999. **286**: p. 1931-1934.

24. Aggarwal, S., Monga, A.P., Perusse, S.R., Ramesh, R., Ballarotto, V., Williams, E.D., Chalamala, B.R., Wei, Y., Reuss, R.H., Science, 2000. **287**: p. 2235-2237.

25. Mederros-Ribeiro, G., Bratkovski, A.M., Kamins, T.I., Ohlberg, D.A.A., Williams, R.S., Science, 1998. **279**: p. 3534-3536.

26. Mo, Y.-W., Savage, D.E., Swartzentruber, B.S., Lagally, M.G., Phys. Rev. Lett., 1990. **65**: p. 1020-1023.

27. Eaglesham, D.J., and Cerullo, M., Phys. Rev. Lett., 1990. **64**: p. 1943-1946.

28. Floro, J.A., Chason, E., Twesten, R.D., Hwang, R.Q., Freund, L.B., Phys. Rev. Lett., 1997. **79**: p. 3946-3949.

29. Leon, R., Senden, T.J., Kim, Y., Jagadish, C., Clark, A., Phys. Rev. Lett., 1999. **78**: p. 4942-4945.

30. Aggarwal, S., Ogale, S.B., Ganpule, C.S., Shinde, S.R., Novikov, V.A., Monga, A.P., Burr, M.R., Ramesh, R., Ballarotto, V., Williams, E.D., Appl. Phys. Lett., 2001. **78**: p. 1442-1444.

31. Lefakis, H., Ho, P.S., Thin Solid Films, 1991. **200**(1): p. 67.

32. Venables, J.A., Phil. Mag.,, 1973. **27**: p. 697-738.

33. Venables, J.A., Spiller, G.D. T., and Hanbuecken, M., Rep. Prog. Phys., 1984. **47**: p. 399-459.

34. Venables, J.A., Phys. Rev. B., 1987. **36**: p. 4153-4160.

35. Venables, J.A., Surface Science, 1994. **299/300**: p. 798-817.

36. Bartelt, M.C., Stoldt, C.R., Jenks, C.J., P.A. Thiel, and Evans, J.W., Phys. Rev. B., 1999. **59**: p. 3125-3134.

37. Bartelt, M.C., Stoldt, C.R., Jenks, C.J., P.A. Thiel, and Evans, J.W., Colloids and Surfaces, 2002. **165**: p. 373-403.

38. Yang, J.C., Yeadon, M., Kolasa, B., Gibson, J.M., Appl. Phys. Lett., 1997. **70**: p. 3522-3524.

39. Yang, J.C., Yeadon, M., Kolasa, B., Gibson, J.M., Scripta Materialia, 1998. **38**: p. 1237-1241.

40. Yang, J.C., Yeadon, M., Kolasa, B., Gibson, J.M., Appl. Phys. Lett., 1998. **73**: p. 2481-2483.

41. Lawless, K., and Mitchell, D., Memories Scientifiques Rev. Metallurg., 1965. **LXII**.

42. Brockway, L.O., Adler, I.M., J. Electrochem. Soc., 1972. **119**: p. 899-901.

43. Goulden, D.A., Phil. Mag., 1976. **33**: p. 393-408.

44. Milne, R.H., and Howie, A., Phil. Mag. A,, 1984. **49**: p. 665-682.

45. Keinemann, K., Rao, D.B., and Douglas, D.L., Oxidation of Metals, 1975. **9**: p. 379-400.

46. Marikar, P., Brodsky, M.B., Sowers, C.H., Zaluzec, N.J., Ultramicroscopy, 1989. **29**: p. 247-256.

47. Onay, B., Rapp, R.A., Oxidation of Metals, 1988. **29**(5/6): p. 473-486.

48. Raynaud, G.M., Clark, W.A.T, Rapp, R.A., Metallurgical Transactions A, 1984. **15A**: p. 573-586.

49. Rakowski, J.M., Meier, G.H., Pettit, F.S., Scripta Materialia, 1996. **35**(12): p. 1417-1422.

50. Li, J.S.-D., Y., and Mayer, J.W., Mater. Sci. Rep., 1992. **9**: p. 1-43.

51. Ronnquist, S., and Fisher, H., J. Inst. Met., 1960-61. **89**: p. 65-78.

52. Lawless, K.R., and Gwathmey, A.T., Acta Metall., 1956. **4**: p. 153.

53. Young, F., Cathcart, J., and Gwathmey, A., Acta Metall., 1956. **4**: p. 145.

54. Lawless, K.R., Rep. Prog. Phys., 1973. **37**: p. 231.

55. Park, J.-H., Natesan, K., Oxidation of Metals, 1993. **39**(5/6): p. 411-435.

56. Mrowee, S., Stoklosa, Oxidation of Metals, 1971. **3**(3): p. 291-311.

57. Guan, R., Hashimoto, H., Yoshida, T., Acta Cryst. B, 1984. **40**: p. 109-114.

58. Guan, R., Hashimoto, H., Kuo, K.H., Acta Cryst. B, 1984. **40**: p. 560-566.

59. Guan, R., Hashimoto, H., Kuo, K.H., Acta Cryst. B, 1985. **41**: p. 219-225.

60. Guan, R., Hashimoto, H., Kuo, K.H., Yoshida, T., Acta Cryst. B, 1987. **43**: p. 343-346.

61. Guan, R., Hashimoto, H., Kuo, K.H., Acta Cryst. B, 1990. **46**: p. 103-111.

62. Honjo, G., Soc. Of Japan Journal, 1949. **4**: p. 330.

63. McDonald, M.L., Gibson, J.M., Unterwald, F.C., Rev. Sci. Instrum., 1989. **60**: p. 700.

64. Zimmermann, C., *Ph.D. thesis*, in *Department of Physics*. 2000, University of Augsburgh, Germany.

65. Murr, L.E., and Inman, M.C., Phil. Mag., 1966: p. 135.

66. Kehoe, R.B., Phil. Mag., 1956: p. 455.

67. Safran, G., Geszti, O., and Barna, P.B, Phys. Stat. Sol. (A), 1995. **150**: p. 489.

68. Yeadon, M., et al, Mater. Res. Soc. Symp. Proc., 1997. **457**: p. 179-184.

69. Mullins, W.W., J. Appl. Phys., 1959. **30**: p. 77.

70. Mochrie, S.G., Phys. Rev. Lett., 1987. **59**: p. 304-307.

71. Francis, S.M., Leibsle, F.M., Haq, S., Xiang, N., Bowker, M., Surface Science, 1994. **315**: p. 284.

72. Instruments, D., *Scanning probe microscopy training notebook*.

73. Milne, R.H. in *EMAG, 90*. 1987. Manchester, United Kingdom.

74. Afify, H.H., Terra, F.S., Momtaz, R.S., Journal of Materials Science-Materials in Electronics, 1996. **7**(2): p. 149.

75. Tran, N.T., Keyes, M.P., Physica Status Solidi A, 1991. **126**(2): p. 143.

76. Markworth, P.R., Liu, X., Dai, J.Y., Fan, W., Marks, T.J., Chang, R.P.H., J. Mater. Res., 2001. **16**: p. 2408-2414.

77. Tersoff, J., Tromp, R.M., Phys. Rev. Lett., 1993. **70**: p. 2782-2785.

78. Hembree, G.G., Venables, J.A., Ultramicroscopy, 1992. **47**: p. 109.

79. Akiyama, M., Ueda, T., Onozawa, S., Mater. Res. Soc. Symp. Proc., 1988. **116**: p. 79.

80. Scheuch, V., Voigtlander, B., Bonzel, H.P., Surface Science, 1997. **372**: p. 71.

81. Brongersma, S.H., Castell, M.R., Perovic, D.D., Zinke-Allmang, Phys. Rev. Lett., 1998. **80**: p. 3795.

82. Mundschau, M., Bauer, E., Telieps, W., Swiech, W., Surface Science, 1989. **213**: p. 381.

83. Yang, H., Ballet, P., Salamo, G.H., J. Appl. Phys., 2001. **89**: p. 7871.

84. Meyers, M.A., Chawla, K.K, *Mechanical behavior of Materials*. 1998: Prentice Hall, INC.

85. Orr, W.H., *Ph.D thesis*. 1962, Cornell University.

86. Zhou, G.W., Yang, J.C., Phys. Rev. Lett., 2002. **89**(10): p. 106101-106104.

87. Zhou, G.W., Yang, J.C., Appl. Surf. Sci., 2003. **210**: p. 165-170.

88. Markov, I.V., *Crystal growth for beginners: fundamentals o nucleation, crystal growth, and epitaxy*. 1995, NJ: World Scientific.

89. Ohring, M., *The materials science of thin films*. 1992, NY: Academic Press.

90. Jungling, T.L., Rapp, R.A., Metallurgical Transactions A, 1984. **15**: p. 2231-2240.

91. Suzuki, T., Takeuchi, S., Yoshinaga, H., *Dislocation Dynamics and Plasticity*. 1985: Springer-Verlag.

92. Frost, H.J., Ashby, Michael F, *Deformation-Mechanism Maps*. 1982, Oxford: Pergamon.

93. Lide, D.R., *CRC Handbook of Chemistry and Physics*. 1999, Boca Raton, FL: CRC Press.

94. Doremus, R.H., *Rates of Phase Transformations*. 1985, Orlandi, FL: Academic Press. 99.

95. Howe, J.M., *Interfaces in Materials*. 1997, New Rork: Wiley Interscience. 145.

96. Gwathmey, A.T., Lawless, K.R., *The Surface Chemistry of Metals and Semiconductors*, H.C. Gatos, Editor. 1960, John Wiley and Sons, Inc.: New York. p. 483.

97. Bardolle, J., Benard, J., Rev. Met., 1952. **49**: p. 613.

98. Benard, J., Gronlund, F., Oudar, Jr., Duret, M., Z. Elektrochem. Ber. Bunsenges Physik, Chem., 1959. **63**: p. 799.

99. Holloway, P.H., Hudson, J.B., Surface Science, 1974. **43**: p. 123.

100. Foiles, S.M., Baskes, M.I., Daw, M.S., Phys. Rev. B., 1986. **33**: p. 7983.

101. Williams, D.B., Carter, C.B., *Transmission electron microscopy*. 1996, New York: Plenum. 369.

102. Zhou, G.W., Yang, J.C., Surface Science, 2003. **531**: p. 359-367.

103. Burton, W.K., Cabrera, N., Frank, F.C., Philos. Trans. R. Soc. London A, 1951. **243**: p. 299.

104. Nijs, M.D., Phys. Rev. B., 1992. **46**: p. 10386-10410.

105. Wollschager, J., Luo, E.Z., Henzler, M., Phys. Rev. B., 1991. **44**: p. 13031-13041.

106. Cao, Y., Conrad, E., Phys. Rev. B., 1990. **64**: p. 447-450.

107. Zeppendfeld, P., Kern, k., David, R., Comsa, G., Phys. Rev. Lett., 1989. **62**: p. 63-66.

108. Martin, D.S., Maunder, A., Weightman, P., Phys. Rev. B., 2001. **63**: p. 155403-155410.

109. Ocko, B.M., Mochrie, S.G.J., Phys. Rev. B., 1988. **38**: p. 7378-7384.

110. Weeks, J.D., Phys. Rev. Lett., 1983. **50**: p. 1077-1080.

111. Weeks, J.D., *Ordering in Strongly Fluctuating Condensed Matter Systems*, T. Riste, Editor. 1980, Plenum: New York. p. 293.

112. Gorse, D., Lapujoulade, J., Surface Science, 1985. **162**: p. 847.

113. Fauster, T., Schneider, R., Durr, H., Engelmann, G., Taglauer, E., Surface Science, 1987. **189/190**: p. 610.

114. Williams, R.S., Wehner, P.S., Stohr, J., Shirley, D.A., Phys. Rev. Lett., 1977. **39**: p. 302.

115. Baddorf, A.P., Plummer, E.W., Phys. Rev. Lett., 1991. **66**: p. 2770-2773.

116. Maxson, J.B., Savage, D.E., Liu, F., Tromp, R.M., Reuter, M.C., Lagally, M.G., Phys. Rev. Lett., 2000. **85**: p. 2152-2155.

117. Vlachos, D.G., Schmidt, L.D., Aris, R., Phys. Rev. B., 1993. **47**: p. 4896-4909.

118. Walko, D.A., Robinson, I.K., Phys. Rev. B., 2001. **64**: p. 45412-45423.

119. Flynn, C.P., Swiech, W., Appleton, R.S., Ondrejcek, M., Phys. Rev. B., 2000. **62**: p. 2096-2107.

120. Heffelfinger, J., Carter, C.B., Surface Science, 1997. **389**: p. 188-200.

121. Reinecke, N., Taglauer, E., Surface Science, 2000. **454-456**: p. 94-100.

122. Horn-von Hoegen, M., Meyer zu Heringdorf, F.J., Kahler, D., Schmidt, Th., Bauer, E., Thin Solid Films, 1998. **336**: p. 16-21.

123. Mullins, W.W., Phil. Mag., 1961. **6**: p. 1313.

124. Song, S., Mirang Yoon, S., Mochrie, G.J., Stephenson, G.B., Milner, T., Surface Science, 1997. **372**: p. 37.

125. Liu, F., Metiu, H., Phys. Rev. B., 1993. **48**: p. 5808.

126. Rousset, S., Repain, V., Baudot, G., Ellmer, H., et al., Mater. Sci. and Eng. B, 2002. **96**: p. 169-177.

127. Spisak, D., Hafner, J., Phys. Rev. B., 2002. **65**: p. 235405.

128. Yu, C.T., Li, D.Q., Pearson, J., Bader, S.D., Appl. Phys. Lett., 2001. **79**: p. 3848-3850.

129. Dubois, L.H., Surface Science, 1982. **119**: p. 399.

130. Niehus, H., Surface Science, 1983. **130**: p. 41.

131. Habraken, F.H.P.M., Kieffer, E.Ph., Bootsma, G.A., Surface Science, 1979. **83**: p. 45.

132. Thurgate, S.M., Jennings, P.J., Surface Science, 1983. **131**: p. 309.

133. Ho, J.H., Vook, R.W., J. Cryst. Growth, 1978. **44**: p. 561.

134. Mcdonnell, L., Woodruff, D.P., Surface Science, 1974. **46**: p. 505.

135. Ertl, G., Surface Science, 1967. **6**: p. 208.

136. Simmons, G.W., Mitchell, D.F., Lawless, K.R., Surface Science, 1967. **8**: p. 130.

137. Spitzer, A., Luth, H., Surface Science, 1982. **118**: p. 136.

138. Judd, R.W., Hollins, P., Pritchard, J., Surface Science, 1988. **171**: p. 643.

139. Haase, J., Kuhr, H.J., Surface Science, 1988. **203**: p. L695.

140. Luo, B., Urban, J., J. Phys. Condens. Matter, 1991. **3**: p. 2873.

141. Johnston, S.M., Mulligan, A., Dhanak, V., Kadodwala, M., Surface Science, 2002. **519**: p. 57-63.

142. Toomes, R.I., Woodruff, D.P., Polcik, M., Bao, S., Hofmann, Schindler, K.M., Surface Science, 2000. **443**: p. 300.

143. Matthews, J.W., IBM Researh Report, 1973. **RC 4266**.

144. Jensen, F., Besenbacher, F., Lagsgaard, E., Stensgaard, I., Surface Science, 1991. **259**: p. l781.

145. Jensen, F., Besenbacher, F., Lagsgaard, E., Stensgaard, I., Surface Science Letters, 1991. **259**: p. L774-780.

146. Ross, F.M., Tersoff, J., Tromp, R.M., Phys. Rev. Lett., 1998. **80**: p. 984.

147. Tersoff, J., LeGoues, F.K., Phys. Rev. Lett., 1994. **72**: p. 3570.

148. Hansen, M., *Constitution of Binary Alloys*. 1958, NY: McGraw-Hill.

149. Pastorek, R.L., Rapp, R.A., Trans. of The Metallurgical Society of AIME, 1969. **245**: p. 1711-1720.

150. Jeurgens, L.P.H., Sloof, W.G., Tichelaar, F.D., Mittemeijer, E.J., Phys. Rev. B., 2000. **62**: p. 4707.

151. Kubaschewski, O., Alcock, C.B., *Metallurgical Thermochemistry*. 1979, Oxford: Pergamon.

152. Hondros, E.D., McLean, M., J Mat. Sci., 1973. **8**: p. 349.

153. Fuhr, S., Shirley, S.G., *Biological application of microstructures.* Topics in current chemistry, 1998. **194**: p. 84-116.

154. Flink, S., van Veggel, F.C.J.M., Reinhoudt, D.N., Adv. Mater., 2000. **12**: p. 1315.

155. Gillmor, S.D., Thiel, A.J., Strother, T.C., Smith, L.M., Lagally, M.G., Langmuir, 2000. **16**: p. 7233.

156. Ohko, Y., Hashimoto, K., Kitamura, A., J. Phys. Chem. A, 1997. **101**: p. 8057.

157. Wang, R., Hashimoto, K., Fujishima, Chikuni, A., M., Kojima, E., Kitamura, Shimohigoshi, A. M., Watanabe, T., Nature, 1997. **388**: p. 431.

158. Wang, R., Adv. Mater., 1998. **2**: p. 135.

159. Bard, A.J., Science, 1980. **207**: p. 139.

160. Mizuno, K., F.K., Yamauchi, Y., Homma, T., Tanaka, A., Takakuwa, Y., Momose, T., J. Vac. Sci. Technol. A, 2002. **20**(5): p. 1716-1721.

161. Vaquila, I., Passeggi, M., Ferron, J., J. Phys.: Condens. Matter, 1993. **5**: p. A157-A158.

162. Vaquila, I., Passeggi Jr, M., Ferron, J., Applied Surface Science, 1996. **93**: p. 247-253.